CENTRO DE INVESTIGACIONES EN OPTICA, A.C.

"IMAGING APPROACHES FOR THE STUDY OF DEMYELINATION PROBLEMS IN H-ABC TUBULINOPATHY"

Tesis que para obtener el grado de Doctor en Ciencias (Óptica)

Presenta: *Milvia Iris Alata Tejedo*

Director de Tesis: *Dra. Valeria Piazza*

León · Guanajuato · México
Febrero de 2022

Abstract

Hypomielination with atrophy of the basal ganglia and cerebellum (H-ABC) is a central neurodegenerative disease due to mutations in the tubulin beta 4a gene. Diagnosis is made by integrating clinical data, magnetic resonance imaging of the brain and genetic analysis.

In this work we have used three different imaging approaches for the study of the central nervous system affected by H-ABC: magnetic resonance imaging (MRI), second harmonic generation (SHG) microscopy and fluorescence microscopy. Our experiments were performed in the *taiep* rat, which is the only spontaneous tubulin beta 4a mutant available for the study of this pathology.

The pathological signs presented by *taiep* rats and the morphological changes we found by our longitudinal MRI study were similar to those of patients with mutations in TUBB4A. Using the novel label free SHG microscopy, we identified microstructural differences between the central nervous system of *taiep* rats compared to control animals. We contrasted our MRI and SHG findings with images of fluorescently labeled tissue from *taiep* and control rats. The fluorescence microscopy results corroborate the hypomielination of *taiep* rats in the corpus callosum, the cerebellum and the striatum. On the other hand, the comparison of fluorescence with SHG microscopy results, indicate that microtubules from oligodendrocytes were the source of abnormal signal, which was clearly localized in white matter regions.

The importance of this work stems from the demonstration that nonlinear optics can be used not only to study and advance the understanding of the pathophysiology of tubulinopathies, but that it also has the potential to represent a new diagnostic approach to the medical problem. Demyelinating disorders are difficult to diagnose, and therefore new complementary techniques could be helpful for the description of those features of the disease that could potentially be used as clinical markers.

A diverse readership may benefit from the information detailed in this work, whether they are from scientific areas involved in the study of the cell cytoskeleton, the development of optical imaging devices or interested in the study of neurobiology and neurodevelopmental disorders.

Resumen

Hipomielinización con atrofia de los ganglios basales y el cerebelo (H-ABC) es una enfermedad neurodegenerativa central debida a mutaciones en el gen TUBB4A. El diagnóstico se realiza integrando datos clínicos, imágenes por resonancia magnética del cerebro y análisis genético.

En este trabajo hemos utilizado tres enfoques de imagenología diferentes para el estudio del sistema nervioso central afectado por H-ABC: imágenes de resonancia magnética (MRI), microscopía de generación de segundo armónico (SHG) y microscopía de fluorescencia. Nuestros experimentos se realizaron en la rata *taiep*, que es el único mutante espontáneo de tubulina beta 4a disponible para el estudio de esta patología.

Los signos patológicos presentados por las ratas *taiep* y los cambios morfológicos que encontramos en nuestro estudio de resonancia magnética longitudinal fueron similares a los de los pacientes con mutaciones en TUBB4A. Utilizando microscopía por SHG sin necesidad de marcaje, identificamos diferencias microestructurales entre el sistema nervioso central de ratas *taiep* en comparación con los animales de control. Contrastamos nuestros hallazgos de MRI y SHG con imágenes de fluorescencia de tejidos de ratas *taiep* y de control. Los resultados de la microscopía de fluorescencia corroboran la hipomielinización de ratas *taiep* en el cuerpo calloso, el cerebelo y el estriado. Por otro lado, la comparación de la fluorescencia con los resultados de la microscopía de SHG, indica que los microtúbulos de los oligodendrocitos son la fuente de señal anómala, ubicada claramente en las regiones de materia blanca.

La importancia de este trabajo surge de la demostración de que la óptica no lineal puede usarse no solo para estudiar y avanzar en la comprensión de la fisiopatología de las tubulinopatías, sino que también tiene el potencial de representar un enfoque diagnóstico nuevo del problema médico. Los trastornos desmielinizantes son difíciles de diagnosticar y, por lo tanto, nuevas técnicas complementarias podrían ser útiles para la descripción de aquellas características de la enfermedad que potencialmente podrían usarse como marcadores clínicos.

Un público diverso puede beneficiarse de la información detallada en este trabajo, ya sean de áreas científicas involucradas en el estudio del citoesqueleto celular, el desarrollo de dispositivos ópticos para la adquisición de imágenes o interesados en el estudio de la neurobiología o de los trastornos del desarrollo del sistema nervioso central.

Agradecimientos

Agradezco al Consejo Nacional de Ciencia y Tecnología y al Centro de Investigaciones en Óptica A.C. por su apoyo en el desarrollo de este proyecto.

También agradezco a la Universidad de Guanajuato, la Benemérita Universidad Autónoma de Puebla, al Centro de investigaciones en Matemáticas y al Laboratorio Nacional de Imagenología por Resonancia Magnética de la UNAM, instituciones con las que mantuvimos una colaboración científica constante.

Mi mayor reconocimiento para la Dra. Valeria Piazza quien fue mi asesora y tuvo la generosidad de compartir conmigo su conocimiento y experiencia. Gracias a sus ideas y recomendaciones pude avanzar en la obtención del grado y a la par disfrutar del proceso.

De la misma manera a los miembros de mi comité de seguimiento, los Dres. Victor Hernandez, Eden Morales y Ramón Carriles, quienes cada cuatrimestre aportaron con sus preguntas y recomendaciones al desarrollo de este proyecto y a mi evolución profesional.

Quiero reconocer también el valioso aporte de los sinodales que revisaron mi tesis y me dieron valiosas observaciones para mejorarla.

También quiero dedicar unas palabras para mis compañeros tanto a los de posgrado como a los de laboratorio, con quienes pasamos muchas horas trabajando y conversando de la vida. Definitivamente los voy a extrañar.

Quiero agradecer de manera especial a mi hija y mi esposo quienes han vivido esta etapa conmigo, quiero decirles que han hecho de este proceso aún más gratificante y han sido mi mayor soporte emocional. Los amo muchísimo.

Index

Introduction

The efficient transmission of electric impulses trough axons require an electric insulator, this insulator is the myelin sheath[1]. The myelinating cells of the central nervous system are the oligodendrocytes, which extend many processes that concentrically wrap around the nerve axon[2]. Oligodendrocytes undergo a complex and precisely timed program of proliferation, migration, differentiation, maturation, and myelination to finally produce the insulating sheath of axons[3]. Myelin is necessary for the formation, health and function of the central nervous system (CNS)[4].

There was a time when disorders that primarily affect myelin where mostly undefined and the few that were known had to be diagnosed via metabolic investigations. The introduction of magnetic resonance imaging, in the late eighties, completely changed the diagnosis approach and opened new possibilities in the white matter field study. The high sensitivity of MRI to white matter abnormalities made possible the recognition of patterns in patients that shared the same diagnosis, and to also recognize that the patterns were different from patients with other diagnosis[5,6]. Even though, in many cases it was not possible to establish a specific diagnose. Later in 2001, the idea of defining new white matter disorders by their MRI pattern was finally validated when the first mutated genes were identified in withe matter disorders defined by MRI (EIF2B1-5 for vanishing white matter and MLC1 for megalencephalic leukoencephalopathy with subcortical cysts)[7,8]. The development of next-generation sequencing in 2005 allowed the rapid sequencing of large amounts of DNA[9]. Whole exome sequencing provides a definitive diagnosis in 80–90% of patients[10]. The technological advances, MRI and next generation sequencing provided new information that changed a concept that was ideated in the 1930s, leukodistrophy, which at that time was used to describe disorders primarily affecting myelin, either directly or through involvement of oligodendrocytes, caused by a genetic defect and clinically progressive sign and symphtoms. Nowadays, we know that some leukodistrophies are caused by mutations that affect proteins that are specifically expressed in cell types other than oligodendrocytes, like CSF1R gene which is expressed in microglia, macrophages and monocytes[11]; and there are leukodistrophies that are not necessarily progressive like megalencephalic leukoencephalopathy with subcortical cysts that was found to have an improving variant along with only transient abnormalities on MRI[12]. Another important

discovery is that a high percentage of genetic defects found in leukodistrophies affect the highly complex process of mRNA translation[13]. The discoveries behind the reconceptualization of leukodistrophies tell us how the availability of different techniques offered new perspectives to understand these diseases.

Hypomielination with Atrophy of the Basal Ganglia and the Cerebellum

One of the diseases that was defined thanks to MRI patterning and next-generation sequencing is hypomyelination with atrophy of the basal ganglia and the cerebellum (H-ABC). It was described for the first time in 2002 by Van der knaap et al.; when they were studying a group of 102 patients with unclassified leukoencephalopathies that had hypomyelinating disorders, they identified seven patients whose putamen was absent without evidence of a lesion in the region. These individuals had a distinct MRI pattern consisting of a triad of radiological signs: hypomyelination, atrophy of the caudate, putamen and the cerebellum (Fig. 1.1). Although the severity of the clinical picture varied among the patients, the overall pattern was very similar. The onset of H-ABC was variable, ranging from infancy to childhood. And the clinical profile included developmental delay, dystonia, choreoathetosis, rigidity, opisthotonus, and oculogyric crises, progressive spastic tetraplegia, ataxia and more rarely, seizures[7].
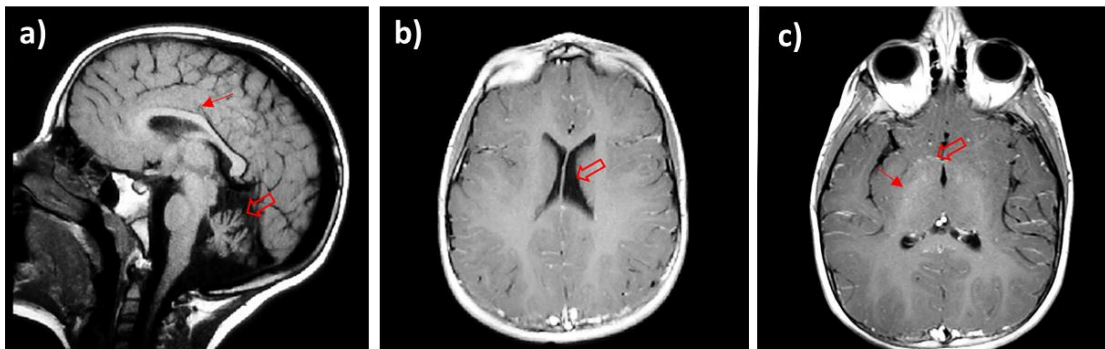

Figure 1.1 *Brain structures in a patient suffering from H-ABC. (a) Sagittal T1-weighted magnetic resonance images obtained at 5 years show atrophy of cerebellum (open arrow), corpus callosum (arrow). (b) Axial T2-FLAIR weighted magnetic resonance images obtained at 5 years old show atrophy of the brain cortex and ventriculomegaly (open arrow). (c) Atrophy of caudate (open arrow) and putamen (arrow) are also observed*[14].

By 2013 only 22 cases of H-ABC had been reported in the literature, from all of those none were from siblings, which hindered the identification of causative mutation. Using exome

sequencing Simons et al. studied eleven H-ABC patients and some of their relatives with the intention of establishing if H-ABC was the effect of a single monogenic entity or a group of heterogeneous leukoencephalopathies. They identified the TUBB4A c.745G>A mutation, which causes a nonsynonymous change from an aspartic acid to asparagine at the residue n. 249 of the TUBB4A protein (p.Asp249Asn)[15]. After modeling TUBB4A they could generate a hypothesis about the effects of the mutations according to its localization. The mutation´s position might affect the dimerization of tubulin, the polymerization or the stability of microtubules. They also hypothesized that the TUBB4A mutation results in primary disturbance of neurons and the secondary involvement of glial cells. Finally, they concluded that a single *de novo* mutation in TUBB4A resulted in H-ABC.

To date, more than 40 mutations of TUBB4a have been found in H-ABC patients[16–21]. The p.Asp249Asn is the most common mutation among all of them: it is also the mutation that our group identified in the first Mexican patient diagnosed with H-ABC (Fig. 1)[14,22]. Leukodistrophies are still difficult to diagnose and even more for sporadic diseases like H-ABC that are still not very familiar to clinicians. The features of H-ABC found in magnetic resonance images (MRI) together with the clinical signs give a strong indication of the disease, but definitive identification can only be provided by genetic analysis. The necessity of the genetic study for confirmation is an obstacle in low income countries and therefore the real population of patients affected by H-ABC may be higher. Approximately 200 children have been diagnosed with this rare disease, so far[23].

Tubulinopathies

H-ABC is also part of a family of diseases called tubulinopathies, which comprises a wide, overlapping range of brain malformations caused by mutations in genes that codify for tubulins and for microtubule associated proteins[24]. The main clinical symptoms of tubulinopathies are motor impairment, intellectual disability and epilepsy[25]. Patients who suffer from tubulinopathies may present many different complex brain malformations. One of the most common morphological imaging patterns in patients of tubulinopathies are the dysmorphic basal ganglia which are seen in about 75% of cases. Other abnormalities include hypoplasia or agenesis of the corpus callosum, brainstem, cerebellar hypoplasia and dysplasia, and cortical

malformations like lissencephaly and polymicrogyria[26]. Tubulin mutations can cause neurodevelopmental diseases and neurodegeneration. It is not clear how tubulinopthies impair tubulin functions and neuron activities, causing neurodegeneration or neurodevelopmental defects[27].

Tubulins are the building blocks of microtubules (MTs) which have an important role in brain development: to better understand tubulinopathies it is necessary to know about the composition and function of microtubules.

The Microtubules

The cell's cytoskeleton performs a variety of tasks among them controlling cell shape, cell movement, cell division, organization of cell components and the transport of proteins. The cytoskeleton is formed by a network of protein filaments: microfilaments, intermediate filaments and microtubules (MTs). Those filaments are not rigid, instead they are dynamic structures in constant modification[28].

The ability of MTs to rapidly assembly and disassembly is essential for basic cellular processes such as cell division (mitotic spindle), motility and differentiation[29]. In animal cells, long MTs grow out from centrosomes providing the tracks for intracellular transport. MTs also form the core of eukaryotic cilia and flagella, arranging in very organized and stable bundles[30]. During nervous system development, cellular events such as mitotic division, relocation of migrating neurons and the extension of dendritic and axonal processes highly depend on microtubules[31]. And in cells with particularly long ramifications like oligodendrocytes, the myelinating cells of the central nervous system, the MTs cytoskeleton is especially important for long distance transport[32].

Microtubules are hollow cylinders formed by alpha/beta tubulins assembled in a head to tail heterodimer. The human genome has nine genes for each α- and β-tubulin, called isotypes[33]. The isotypes differ in their amino acid sequence encoded by different genes. Some of those isotypes are ubiquitously expressed and others are found in some specialized cells, like TUBB3A in sperm[34], TUBB3 in neurons[35] and TUBB1 in platelets[36]. The evidence suggest that the isoforms of tubulins tune the functional properties of MTs depending on the cell type, developmental profile and subcellular localization[31]. During brain development, tubulin

isotypes are differentially expressed, for example Tubb3 isotype is mainly expressed during the early stages of neurite outgrowth and drops at lower levels at mature stages[37].

The polar heterodimers of tubulin form protofilaments which stack together to build the wall of the tube. The microtubule is made of 13 protofilaments arranged parallel to each other. Alpha and beta tubulins alternate along their length, forming a polarized microtubule, with α-tubulin exposed to one side and β-tubulin exposed to the opposite side. The β-tubulin side is called the plus end, because tubulin dimers attach to this end faster than they do to the α-tubulin exposed end. The MT polarity guide intracellular transport [30].

Microtubules and the nervous system

The vertebrate brain development relies on three cellular processes which are highly dependent on the cell cytoskeleton: neurogenesis, neuronal migration and neuronal differentiation[31]. Meaning that mutations that affect tubulins usually relate to brain malformations[24]. Even more, it has been suggested that patients with a reduced myelin volume should be analyzed for tubulin mutations[38]. As it was mentioned before, not all alpha- and beta-tubulin isotypes are expressed in all cell types; for example, TUBB3 is only expressed in neurons, TUBB4a, TUBB2b and TUBB2a are expressed in brain tissue; while others are ubiquitously expressed like TUBB, TUBB4b, TUBB6 and TUBB8. This work focuses on the TUBB4a isotype, which has its highest expression in the cerebellum, putamen and white matter[39]. So far, variants in seven tubulin genes have been associated with an overlapping range of malformations of cortical development (MCD), regarding TUBA1A, TUBB2B, TUBB2A, TUBB3, TUBB4A, TUBB (TUBB5), and TUBG1[26,40]. To date, four tubulin isotypes (TUBB3, TUBB2A, TUBA4A, and TUBB4A) have been associated with neurodegenerative phenotypes[27].

Mutations in TUBB4a

TUBB4A is expressed in the CNS, particularly in the cerebellum and white matter of the brain and also in the striatum[39]. The cells where TUBB4A is primarily localized are neurons and oligodendrocytes, with the highest expression in mature myelinating oligodendrocytes[41].

To predict the possible effects of the amino acid changes caused by missense point mutations it is very important to consider the identity of the new residue, the localization of the amino acid change and its interactions with surrounding aminoacids.

The tubulin monomers are described by three domains that serve different functions: the N-terminal (nucleotide binding domain), the second domain and the C-terminal (outer surface domain)[42]. Mutations in TUBB4a have been found in all three tubulin b-4A monomer domains, even though most of them were found at the intra-dimer interface[16]. Lately, mutations have been classified according to their positions: Inter-dimer interface, kinesin-binding site and intra-dimer interface, looking for possible relations between the mutation position and the patient phenotypes. The canonical p.Asp249Asn mutation is located in the intra-dimer interface, in the second domain T7 loop, a region that interacts with the GTP nucleotide at N-terminal side of the α-tubulin, which is thought to be important for longitudinal interactions between tubulins[15,16].

The *taiep* rat

The study of animal models of diseases has provided medical knowledge necessary for the alleviation of human suffering[43]. Moreover, for a disease without a clear pathophysiology they are essential tools for the validation of hypothesis.

In general, laboratory rats are the prominent model for the study of complex diseases and pharmacology because of their anatomical, physiological and genetic similarity to humans[44].

In 1989 Holmgren et al. described a spontaneous neurological mutant rat, detected in a colony of Sprague Dawley rats, which they named *taiep*[45]. *Taiep* is an acronym formed by the names of the symptoms suffered by the rat: tremor, ataxia, immobility, epilepsy and paralysis. The *taiep* rat suffers from hypomielination at birth and progressive demyelination of the central nervous system in adulthood. Among the regions affected by demyelination there are the optic nerve, the fasciculus gracilis, the corticospinal tract, the corpus callosum and the cerebellum[14,46–48].

Since the discovery of this mutant, different studies have described the abnormalities found in the rat nervous system, including a very particular one: the accumulation of microtubules within its oligodendrocytes[46,47,49].
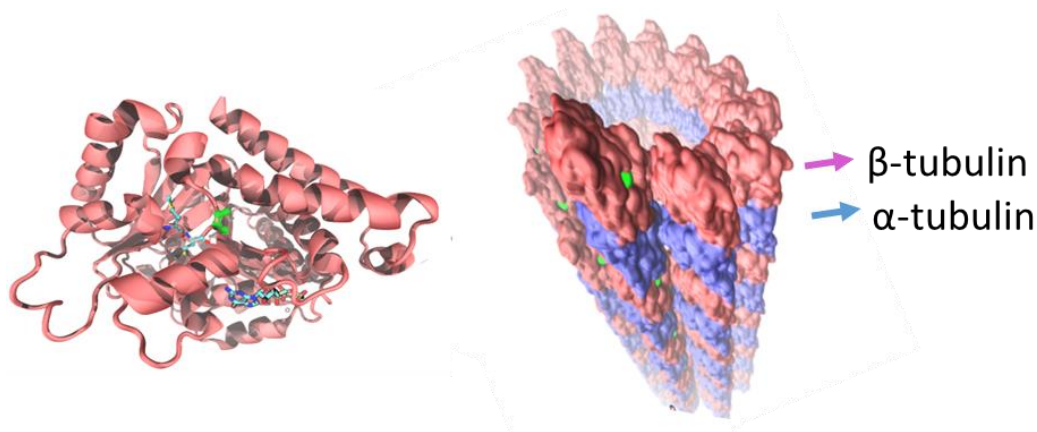
Figure 1.2. *Structural context of Ala302 in the TUBB4A protein. In the quaternary context, Ala302 (green) lies in a cleft along the microtubule separated more than a nanometer from any neighboring protein (Garduno 2020).*

The mutation responsible for the myelin alteration in *taiep* rats, is a single missense mutation that converted Ala302 to Thr (GCG to ACG) (Fig. 1.2), the mutation was found in *taiep* rats from both the University of Wisconsin[50] and the Benemérita Universidad Autónoma de Puebla[48]. Duncan et al. proposed that the mutation was localized in a domain that mediates lateral interactions between dimers. Even though, our rendering of the mutated protein in a 3D model of a microtubule for the position of the amino acidic change suggests it might not be involved in lateral interactions because it is located in a cleft and not in the surface that is in contact with neighboring dimers[48].

Our approach

The aim of this work was to explore new possibilities for the characterization and the diagnosis of neurodegenerative diseases in which hypo or de-myelination is caused by tubulin anomalies.

Magnetic resonance imaging (MRI) was used to first understand the pathological course of the disease in the animal model, the *taiep* rat. The MRI features of the tubulinopathy were described and compared to the human radiological observations, resulting in the presentation of this rat as the first spontaneous mutant that could serve as an animal model for the human disease[48]. Later, the MRI information obtained was also used to analyze auditory consequences related to the tubulinopathy[22] and to make a longitudinal volumetric comparative analysis between brain structures of a Mexican diagnosed H-ABC patient and the animal model[14].

On the other hand, the use of second harmonic generation (SHG) microscopy, in a commercial nonlinear microscope for the assessment of central nervous system tissue sections was proposed and tested. Most of the research of SHG from microtubules is performed in custom made optical systems[51–53]. These systems are optimized in many aspects, like the control of polarization of excitation beam, the use of high numerical aperture objectives for excitation and similar objectives or with a higher numerical aperture (NA) for collection of SHG light, and finally they also include photon counting detection. Even though, the characterization of commercially available nonlinear microscopes for imaging microtubules could popularize the use of this application. Commercial microscopes are precisely designed and provide specialized software for imaging, but this high functionality also imposes some restrictions for alternative use of light sources, variety of condensers and detection systems. The restrictions could be related to availability of compatible options and also to monetary limitations.

Our nonlinear microscope has an infra-red (IR) tunable pulsed laser for excitation, objectives with NA from 0.25 to 1.46, a condenser with NA of 0.55, three options for detection path (one in forward and two in backward direction), two sets of filter cubes, one for the detection of wavelengths below 485 nm and the other for the detection of wavelengths between 500- 550 nm and photomultipliers for signal detection.

We had to establish a protocol for living cells imaging and also for acute tissue sections from CNS imaging. We aimed to obtain SHG signal from microtubules *in vivo* and to achieve that goal we had to first test laser power, with different objective combinations to understand the range of powers to be used without sample damage. Other parameters of image acquisition like imaging speed and averaging had to be tested in parallel to avoid photodamage. The conditions for sample preparation and preservation were also optimized for SHG imaging. We selected the forward nondescanned detection path because we determined that it was the best for microtubules imaging, as it reduced the detection of contributions from other endogenous signals. In images obtained in backward detection path we observed that the intensity of SHG signal was very low compared to the fluorescence arising from two photon excitation.

Although imaging microtubules by SHG is challenging we were able to apply our protocol for label free imaging microtubules in acute tissue sections of the brain and cerebellum of mice and rats. Our path in the implementation of SHG imaging of tissular microtubules involved previous

14

steps and a variety of samples that were suitable for label free SHG imaging. We used a strong and stable SH generating molecule to establish the basic imaging conditions, this sample helped us understanding the limitations and benefits of our system. To determine the ideal structure to image we started imaging a nonlinear crystal BBO (Beta Barium Borate crystal) and corn starch, we chose the latter as the testing sample because its imaging is straightforward, it has strong signal, it does not deteriorate and is inexpensive compared to the nonlinear crystal. With the knowledge obtained we moved to the imaging of more complex samples like collagen from fixed tissue sections, then to collagen and myosin from acute dissected muscle and finally imaging microtubules from living cell cultures in structures like mitotic spindles and axons.

Consistent differences between pathological and control tissue were found in the central white matter. The proposed SHG imaging technique is able to distinguish between tubulin loaded tissue, due to tubulin mutation, and normal tissue. The analysis of the images including SHG, fluorescence microscopy and MRI, strongly suggest that the source of the difference in signal seen in SHG images are the oligodendrocytes rich in tubulin that characterize the tubulinopathy in the CNS of *taiep* rat.

It was concluded that the nonlinear approach of SHG microscopy has comparative advantages to other microscopy techniques previously used to assess the myelin defect in *taiep* rats. SHG is able to obtain signal from live microtubules without the use of any exogenous marker: is label free. Tissue preparation is relatively simple and common solutions used in cell culture and tissue preservation are used. In the case of *taiep* rats, microtubules from oligodendrocytes were the source of abnormal signal, which was clearly localized in white matter regions. Our findings open the door to the possibility of diagnostic approaches that rely on the imaging of bundles of (living) microtubules in their physiological condition.

Ethics Statement

All animals were provided by the animal facility of the Benemérita Universidad Autónoma de Puebla where *taiep* rats were originally described and raised.

All experimental procedures were carried out following the rules of the Declaration of Helsinki of 1975 revised in 2013 and in compliance with the laws and codes approved in the seventh title of the regulations of the general law of health, regarding health research, of the Mexican government (NOM-033-Z00-1995 and NOM-062-ZOO-199) and in accordance with the

recommendations of the National Institutes of Health Guide for the Care and Use of Experimental Animals (eighth edition, 2011). All the procedures for animals and patients were approved by the institutional committee of bioethics in research of the University of Guanajuato and the Benemérita Universidad Autónoma de Puebla.

Justification of the work

This work is justified from two perspectives: On one hand the need of an animal model to study a recently described disease and for which very little is known about the neuropathological changes in the white matter of patients suffering from it, mainly due to the lack of pathologic samples. And on the other hand the need of noninvasive imaging techniques with microscopic resolution to analyze CNS pathological tissue.

General objective

Explore new possibilities for the characterization and the diagnosis of neurodegenerative diseases in which hypo or demyelination is caused by tubulin anomalies

Specific objectives

Detect differences between the cytoskeleton of oligodendrocytes of control versus taiep rats using optic imaging techniques like SHG and fluorescence.

Implement a protocol for the SHG imaging of tubulin in biological systems, using the commercial NLO LSM 710 ZEISS microscope (Germany). In parallel, define the possibilities and the limitations of the imaging system.

Describe the radiological features of *taiep* rat's brain and discover if they are comparable to those seen in H-ABC patients, to determine if this rat is a adequate animal model for tubulinopathies.

Magnetic Resonance imaging and tubulinopathies

A very well established and noninvasive technique used in the diagnosis of neurodegenerative diseases is MRI, which consist in the application of magnetic fields that interact with hydrogen protons found in tissues. The magnetic resonator is able to excite and then detect the change in the trajectory of relaxing protons[54].

The scanner uses pulse sequences, consisting of radiofrequency and gradient pulses, to produce MR images. The duration and the timing of the pulses are precisely determined to enhance the relaxation time of protons: spin-lattice relaxation time and spin-spin relaxation time, denoted T1 and T2, respectively. Both relaxations happen simultaneously but pulse sequences used to better measure T1 are different from the sequences used to measure T2. Contrast in brain is obtained from the difference in relaxation times between tissues and cerebrospinal fluid; tissue types are usually classified as fat based and water based. Regions rich in lipids such as myelin have short T1 (e.g. 100-150 ms) and T2 (10-100 ms), water based tissues have midrange T1 (e.g. 400-120 ms) and also T2 (40-200 ms) and fluids have the longest T1 (e.g. 1500-2000) and T2 (700-1200 ms). In T1 weighted images fluids are very dark (unless flowing), tissues that are water based are mid grey and fat based tissues have the highest intensity[54]. In T2 weighted images fluids are very bright, and water and fat based tissues are gray, being the fat based tissues usually darker.

MR imaging features of H-ABC became clear in a study seeking to define new disease entities among leukoencephalopathies of unknown origin[7]. Using T1 and T2 weighted images, they defined an imaging pattern that differed from others, and consisted of a combination of hypomyelination and atrophy of the basal ganglia and cerebellum (H-ABC). In the 2002 analysis they argued that abnormal white matter containing little myelin has long T1 and T2, which results in low signal on T1 weighted images (hypointensities) and high signal on T2 weighted images (hyperintensities), but when there is diffuse deposition of a small amount of myelin, the effect in T1 shortening is more pronounced than in T2 shortening. Resulting in T2 weighted images with high intensity and T1 intermediate or high signal intensity.

Since its characterization, many studies have confirmed the triad of radiological features in H-ABC patients carrying mutations in TUBB4A[17,20]. Efforts are being made to correlate phenotypic severities with TUBB4A genotype[21].

Longitudinal study of *taiep* rats central nervous system

MRI studies are relatively innocuous compared to other imaging techniques such as X-Ray, making this imaging technique ideal for repeated studies in the same subject over a time course. In the case of recently described diseases, like tubulinopathies, there is not so much information available. Clinical studies reported MRI evidence in the variability of CNS abnormalities expected in patients with mutations in TUBB4A and a few of them analyze MRIs from patients at two different ages. Longitudinal studies allow the extraction of information about disease evolution, which is necessary to fully understand the effects of a mutation.

In this work the progression of the disease in living *taiep* rats was documented by MRI. *Taiep* rat brains were imaged since they were 1 month old and until they were 8 months old. It was planned that rats should be imaged once every month, but problems with the MRI antenna after the third month changed the time plan of the study. After all a full set of data for the 10 rats included in the study for the 1st, 2nd, and 8th months was obtained.

Longitudinal analysis in animals that suffer a disease is not always possible, since many of them might die early or at different, unpredictable time points. In our case, the longitudinal study was possible because, even if *taiep* rats suffer from neurodegeneration they have a long lifespan reaching 18 to 24 months of age[55]. The study of MRI applied to rodent´s brain requires resonators with high magnetic fields to obtain the necessary high resolutions to image small structures. Typical magnetic fields used are 4.7, 7, 9.4, 11.7 T[56] compared to clinical scanners at 1.5 or 3 T. An Helium-cooled 7.0 T scanner (BRUKER PHARMASCAN 70/16 Billerica, MA, USA) (Fig. 2.1 a, b) equipped with a gradient set with Gmax = 760 mT/m BRUKER, from *El laboratorio nacional de imagenología por resonancia magnética (LANIREM)* at *Instituto de Neurobiología UNAM, Juriquilla, Campus Queretaro* was used in this work.
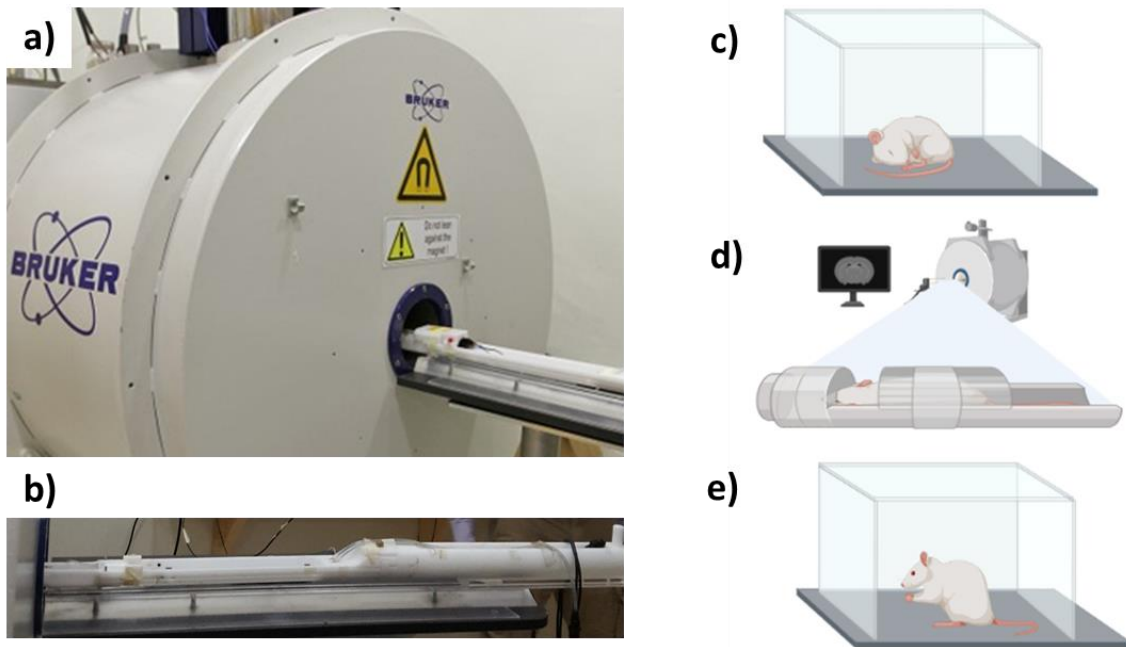
Figure 2.1 *Equipment used for the MRI study and rat anesthesia. a) 7 Tesla magnetic resonance imaging machine. b) Small animals coil. c) The rat receives isoflurane induction anesthetic dose in an induction chamber. d) The rodent remains anesthetized with a maintenance dose during all the procedure. e) The animal recovers from anesthesia in its laboratory rat cage.*

In order to make the most of the study four different sequences of magnetic pulses were included. They were applied in order to obtain anatomical information, diffusion data for white matter analysis and relaxometry data for water content analysis. In this work the T2 weighted images (WI) were used for anatomical and volumetric studies. The other data, related to diffusion and relaxometry analysis are not part of this thesis work and will not be discussed further.

To determine the characteristics of the MRI sequences, it was essential to minimize the time rats spend anesthetized (max of 1 hour) and it should also be sufficient to obtain, first, the anatomical information in T1 and T2 WI (as it is usually obtained for patients) and data for the analysis of myelin content such as diffusion and relaxometry studies. Time was distributed as indicated in Table 1.

Table 2.1 Magnetic resonance imaging sequences

Sequence	Duration	Data type
DTI EPI 60dir	~30 min	Diffusion
T1 FLASH	~4 min	Longitudinal magnetization, anatomical.
T2 Turbo RARE	~5 min	Transversal magnetization, anatomical.
T1 T2 map RARE	~20 min	Relaxometry

DTI: diffusion tensor imaging, FLASH: Fast low angle shot, RARE: Rapid Imaging with Refocused Echoes.

Materials and methods

The MRI study included six *taiep* and four Sprague Dawley wild-type (WT) rats as controls at 1, 2, and 8 months. During the *in vivo* MRI recording, the animals were anesthetized with isoflurane (Sofloran, PiSA Mexico), 5% concentration dose for induction, and 1-2% to maintain an adequate anesthesia level (Fig. 2.1 c-e). A pulse oximeter monitored the rats' oxygenation level, and the body temperature was kept constant throughout the experiment using a thermo-regulated water circulation system.

T2-weighted images

Coronal images were acquired from contiguous 0.8 mm sections in the coronal plane using a Rapid Acquisition with Refocused Echoes (RARE) sequence with the following parameters: repetition time (TR) of 2,673.5 ms; echo time (TE) of 33 ms, field of view (FOV) 20×18 mm^2, matrix size 200×180 corresponding to an in-plane resolution of 0.1×0.1 mm^2.

Sagittal and axial sections were acquired using a sequence with a TR of 15 ms, TE 3 ms, FOV 100 mm^2, and an in-plane resolution of 0.208×0.208 mm^2.

Volume analysis

Volume analysis of the whole encephalon, the corpus callosum (CC), the cerebellum (Cb), the lateral ventricle (LV), 3rd (3V), and 4th ventricles (4V) was carried out using ITK-SNAP (V 3.6.0) software[57]. The areas used to calculate volumes were obtained for each slice by manually tracing the anatomical structure's contour.

Statistical analysis

Statistical analyses were carried out with GraphPad (version 9.1.0 GraphPad Software Inc., La Jolla, CA, USA). Data are plotted as mean ± SEM. Points represent individual measurements in at least n = 3 per group. Statistical differences were analyzed with appropriate tests, indicated in figure legends, comparing the WT and *taiep* groups. For all experiments, $p < 0.05$ was considered significant.

Results

Anatomical features of taiep rats analyzed by MRI
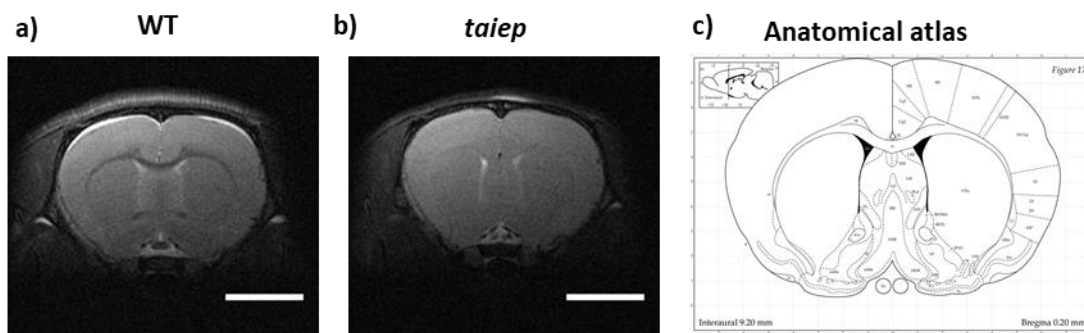

Figure 2.2 *T2 weighted images allow the anatomical analysis of brain and cerebellum. a) Wild Type (WT) brain coronal section of one month old rat brain. b) taiep coronal section at the same plane as in (a). Scale bar 5 mm. c) Paxinos[58] rat brain atlas in the same plane seen in (a) and (b).*

The goal of this first anatomical analysis was to make a qualitative comparison between WT and *taiep* rats brain structures using T2-WI.The Paxinos Rat Brain atlas (2006) was used as an anatomic guide (Fig. 2 c). The images analyzed correspond to 24 planes along the axis of the rat's head, each plane had a thickness of 1.05 mm and the in plane resolution was 10 pixels per millimeter. After a scrutiny of all volume imaged, we identified three planes where differences in recognizable anatomical structures were more pronounced (Fig. 2.3 and Table 2.2).

In the most rostral plane, the corpus callosum (CC) of *taiep* rats appears thinner than in WT rats at 1 month; thinning becomes more pronounced at 2 months, and at 8 months of age CC is no longer visible, while in WT rats it seems to thicken over time as expected (Fig. 2.3 a).

In the second plane, WT rat brains display distinctive white matter features at all ages. In this coronal section, the CC is well-defined and its low signal separates the neocortex (above) from the striatum (below) (Figure 3.2 b). Caudate-putamen, globus pallidus (basal ganglia) and

internal capsule are clearly delineated in healthy rats at all considered ages (Figures 2.3 b). When analyzing equivalent coronal sections of the *taiep* rats, it was found that the CC gets thinner, the internal capsule is not visible and basal ganglia are poorly defined at any age (Fig. 2.3 b).
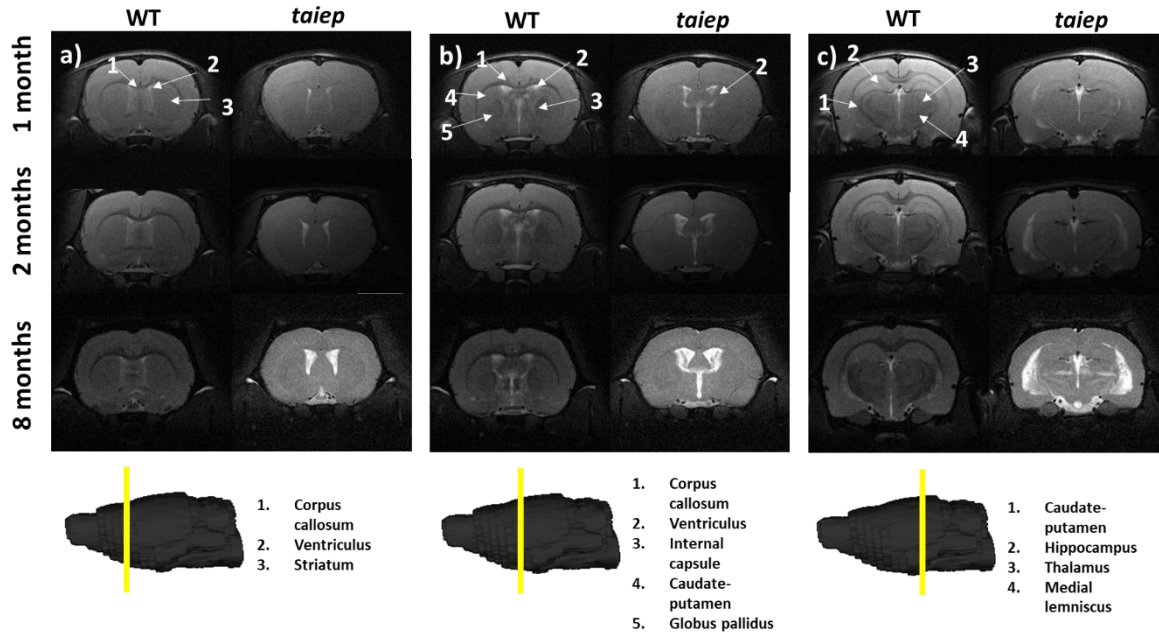

Figure 2.3 *T2 WI from one WT and one taiep rat brain. Coronal sections were taken at three different planes and time-points. a) Corpus callosum, striatum, and lateral ventricles of WT and taiep are visible in the first plane. b) In the second plane is possible to discriminate the caudate-putamen from the globus pallidus and the internal capsule in control rats, while in taiep those structures are indistinguishable. c) In the third plane the thalamus and the hippocampus are visible in the healthy rat, as well as a myelinated, hypointense hippocampal layer. In the three planes the CC is thin or not visible, the ventricles of taiep rats are enlarged and hyperintense signal is obtained from their surrounding areas. Six taiep and four WT rats were analyzed in parallel with equivalent results.*

The most caudal plane offers a thorough view of the CC, the hippocampus, the thalamus, the medial lemniscus (ML), the internal capsule, and the ventricles of the WT rat. In the case of *taiep* rats the white matter is indistinguishable from the neighboring structures and, particularly in this plane, the CC is undetectable already since the first month of age. While in the control animals the hippocampus is always well delineated, its anatomical profile in the *taiep* rats is poorly identifiable. In *taiep* rats the fimbria is not visible and, at 2 months, two out of six rats already presented hyperintensities where this structure should be located. There is also atrophy of the basal ganglia, with poor definition of the areas otherwise occupied by the striatum as well as hyperintensity of the ventricular system, which aggravates with the age of the subjects. The

signal from the ML of *taiep* rats is undetectable at 1 and 2 months but at 8 months the region of the ML gives hyperintense signal opposite to the low signal of ML in WT rats of any age.
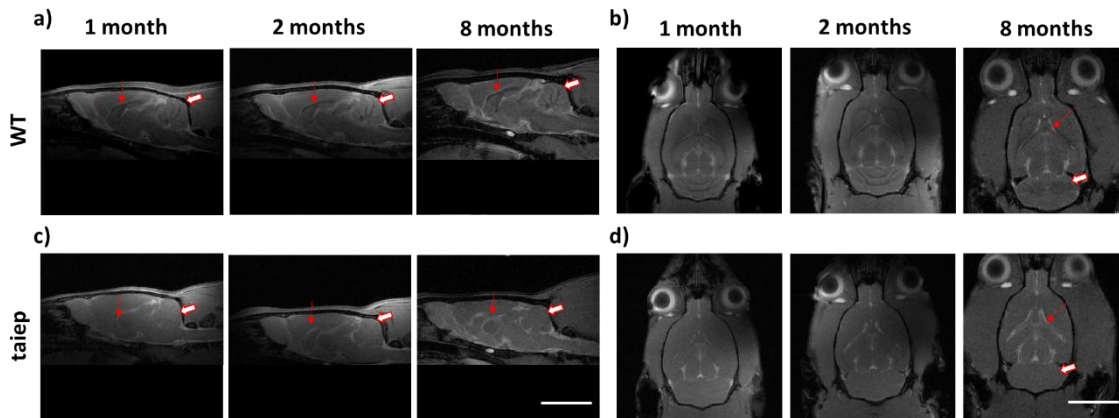

Figure 2.4 *Comparative analysis of the development of brain structures in the taiep rat. a,c) Sagittal T2-weighted MRIs obtained at 1, 2, and 8 months for the wild-type and taiep rat. Signals of the white matter of cerebellum (open arrows) and corpus callosum (arrows) are less visible in taiep rats compared to WT. b, d) Axial T2-weighted MRIs obtained at 1, 2, and 8 months. Progressive enlargement of lateral ventricles (arrows) and cerebellar demyelination (open arrow) is observed in taiep rat at 8 months. Six taiep and four WT rats were analyzed in parallel with equivalent results.*

The sagittal images include the whole brain where the CC and the ventricular system are clearly visible, corroborating from another projection plane the high signal from the CC and the enlargement of the ventricles (Fig. 2.4 a, c). At 2 months, an area of hyperintensity around the ventricles is also evident in two out of six mutant rats; at 4 months it can be detected in four rats and at 8 months all the animals presented this periventricular hyperintensity, whereas in WT rats this signal does not appear (Fig. 2.3 a, b, c). The axial images allow the visualization of the ventricular system, the corpus callosum and the cerebellum. In the *taiep* rat, the cerebellar and callosal white matter generate hyperintensities, consistent with the loss of lipid content (Fig. 2.4 b, d). In both planes the difference between healthy and mutant rats is evident even from the first month, suggesting that the cerebellum is especially affected by demyelination.

Table 2.2 MRI features per subject.

Rat/feature	mo	taiep 1	taiep 2	taiep 3	taiep 4	taiep 5	taiep 6	SD 1	SD2	SD3	SD4
Thinner corpus callosum	1 mo	Very thin	Not visible	Very thin	Very thin	Not visible	Very thin	thick	thick	thick	thick
	2 mo	Thin	Very thin	Not visible	Very thin	Very thin	Very thin	thicker	thicker	thicker	thicker
	8 mo	Very thin	Not visible	Not visible	Not visible	Not visible	Very thin	NA	NA	NA	thicker
Well delimited basal ganglia	1 mo	no	no	no	no	no	no	yes	yes	yes	yes
	2 mo	no	no	no	no	no	no	yes	yes	yes	yes
	8 mo	no	no	no	no	no	no	NA	NA	yes	yes
Internal capsule is visible	1 mo	no	no	no	no	no	no	yes	yes	yes	yes
	2 mo	no	no	no	no	no	no	yes	yes	yes	yes
	8 mo	no	no	no	no	no	no	NA	NA	yes	yes
Medial lemniscus typical low signal	1 mo	Very diffuse	diffuse	diffuse	diffuse	Very diffuse	diffuse	yes	yes	yes	yes
	2 mo	Very diffuse	diffuse	diffuse	diffuse	diffuse	Very diffuse	yes	yes	yes	yes
	8 mo	artifact	artifact	high signal	artifact	high signal	high signal	NA	NA	yes	yes
Hippocampus anatomical profile	1 mo	low	low	Very low	Very low	low	low	yes	yes	yes	yes
	2 mo	low	low	Very low	low	low	low	yes	yes	yes	yes
	8 mo	none	none	none	none	none	none	NA	NA	poco	yes
Hyperintensity around hippocampus	1 mo	low	no	no	no	no	no	no	no	no	no
	2 mo	mild	mild	low	low	no	no	no	yes	no	no
	8 mo	pronounced	pronounced	pronounced	pronounced	pronounced	pronounced	NA	NA	no	no
Hyperintensity of the ventricular system	1 mo	low	no	no	no	no	no	no	no	no	no
	2 mo	low	low	low	low	no	no	no	yes	no	no
	8 mo	pronounced	pronounced	pronounced	pronounced	pronounced	pronounced	NA	NA	no	no
Atrophy of cerebellum	1 mo	mild	mild	mild	mild	pronounced	pronounced	no	no	no	no
	2 mo	pronounced	pronounced	pronounced	pronounced	pronounced	pronounced	no	no	no	no
	8 mo	pronounced	pronounced	pronounced	pronounced	pronounced	pronounced	NA	NA	no	no
hyperintensity around the ventricles	1 mo	low	low	no	no	no	no	no	no	no	no
	2 mo	low	low	no	no	no	no	no	yes	no	no
	8 mo	yes	yes	yes	yes	yes	yes	NA	NA	no	no

NA: not available

Longitudinal Quantitative Analysis of Magnetic Resonance Images of the taiep Rat

T2 weighted images were used for manual segmentation of whole encephalon, corpus callosum, cerebellum, lateral ventricles, third and fourth ventricles in *taiep* and control rats of 1, 2 and 8 months. The free software ITK Snap was selected to perform the segmentation and volume analysis.

Encephalon

The encephalon of control rats grow while the *taiep* rat's encephalon maintain the same volume. In WT rats, the encephalic volume increased significantly (p= 0.0283) from 1 month (1900.2 ± 40.4 mm^3) to 2 months (2168.1 ± 22.3 mm^3) and then remain unchanged (p= 0.933) until 8 months (2253.3 ± 8.5 mm^3). Instead, in the *taiep* rat, the encephalic mass did not show the same growth pattern, i.e., no significant (p=0.348) increase of volume was observed at any analyzed age (to 1 month: 1757.5 ± 38.6 mm^3; to 2 months:1898.1 ± 22.7 mm^3; and to 8 months:1949.8 ± 89.8 mm^3). Comparing WT and *taiep* rats, the encephalic volume did not show significant differences at 1 month of age (p=0.383). However, a delay in the growth rate in *taiep* rats is statistically significant at 2 and 8 months compared to WT volumes (p= 0.0197 and 0.0159, respectively) (Fig. 2.5 d).

Cerebellum

Cerebellar volume remain unchanged in WT and *taiep* rats. WT and *taiep* rat's cerebellar volumes were calculated in the same animals where the encephalic volumes were previously measured. Cerebellar volumes were 233.5 ± 11.5 mm^3 vs. 212.48 ± 14.5 mm^3 at 1 month; 253.4 ± 16.7 mm^3 vs. 248.25 ± 11 mm^3 vs. at 2 months, and 275.4 ± 30.1 mm^3 vs. 258.6 ± 14.3 mm^3 at 8 months, for WT and *taiep*, respectively (Fig.2.5 e). Considering the delay in encephalic growth in *taiep* rats, we calculated the ratio between the cerebellar and encephalic volumes. We did not find significant differences (p >0.05) at the three ages between those ratios, either for control or *taiep* rats (Fig. 2.6 a).
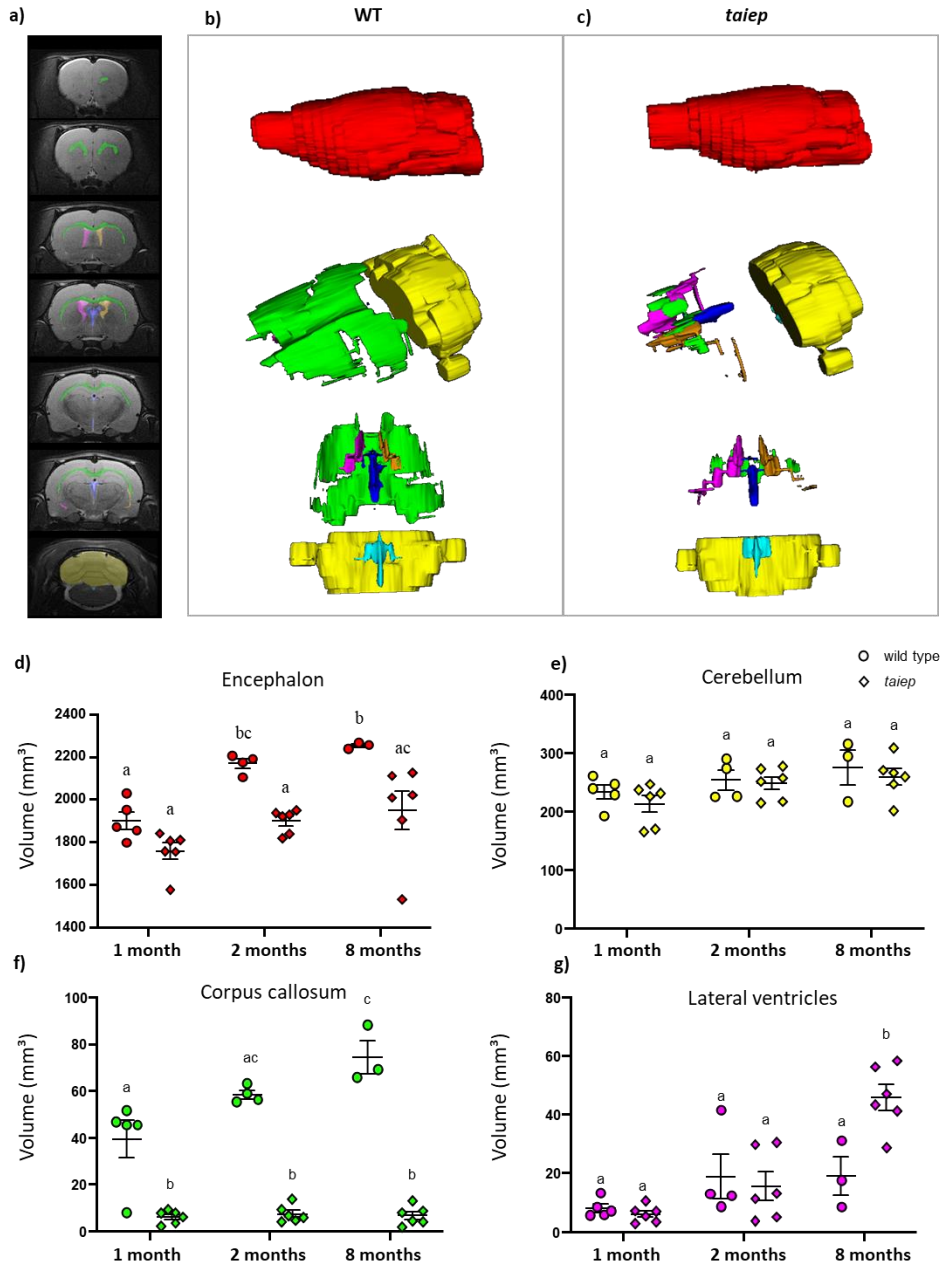
Figure 2.5 *Segmentation and volumetric analysis. a) Excerpts from the 24 coronal planes used, including the segmentation in colors. The whole encephalon in red, the corpus callosum in green, right lateral ventricle in magenta, left lateral ventricle in orange, third ventricle in blue, fourth ventricle in cyan and cerebellum in yellow. b) WT volume reconstruction of segmented structures. Lateral view of the whole encephalon, lateral view from above and view from below. c) taiep volume reconstruction of segmented structures. d-g) Scatter plots of the values of encephalic volume of cerebellum, corpus callosum and lateral ventricles. d) Encephalon volume of WT rats increased and no significant difference in volume was found in taiep rats encephalon. e) Non-significant differences were obtained for the cerebellum volume of WT and taiep rats along the analyzed periods. f) CC volume of taiep rats remains smaller than cc WT CC volume at all analyzed ages. g) Lateral ventricle volume increases significantly compared to WT lateral ventricle volume at 8 months. The data obtained for each rat are represented by one point in the plot (at least n=3 for group). Two-way ANOVA followed by Tukey's multiple comparison test was performed. Different letters indicate significant differences between groups (d-g).*

26

Corpus callosum

The corpus callosum of WT rats was easily recognizable in the brain's MRIs (Fig 2.3), while in the *taiep* rat, the corpus callosum appeared very thin in some slices or even indistinguishable in others (Fig 2.3). Corpus callosum volumes were measured in the regions where it was visible in the T2-weighted images. In WT rats, the corpus callosum volume increased significantly from 1 to 2 months (39.4 ± 7.95 mm^3 and 58.4 ± 1.8 mm^3 respectively; p=0.03) and from 1 to 8 months (74.3 ± 7 mm^3 p= 0.0001). However, no significant differences (p >0.05) were found when comparing corpus callosum volume from 2 months to 8 months of WT rats. There were no significant differences in *taiep* rats when the volume of the corpus callosum was compared at different ages (at 1 month: 6.06 ± 1.1 mm^3; at 2 months: 7.3 ± 1.5 mm^3 and at 8 months: 6.6 ± 1.7 mm^3) (Fig. 2.5 f).

Considering the differences in the encephalic volume between WT and *taiep* rats, the corpus callosum volume related to the encephalic volume was calculated. Data obtained showed that the corpus callosum volume of WT rats increased proportionally to the encephalic volume. Significant differences between 1 and 8 months (p=0.010), but not between 1 and 2 months or 2 and 8 months were measured, suggesting that the corpus callosum grows slowly during wild-type rat development. Instead, in the *taiep* rat, the volume of the corpus callosum related to the encephalic volume did not show significant differences (p>0.05) at any of the analyzed ages, indicating that the corpus callosum is atrophic and it does not grow during development (Fig. 2.6 b). It is important to note that the corpus callosum volume related to the encephalic volume in *taiep* rats is significantly smaller (p <0.0001 when compared at the same age between both group of rats) than that observed in WT rats at all the analyzed ages.

Ventricles

The volume of lateral ventricles did not show significant differences (p> 0.05) at the analyzed ages (8 ± 1.4 mm^3 and 18.7 ± 7.6 mm^3) in WT rats. Instead, in the *taiep* rat, even though there were no significant changes in the volumes of the lateral ventricles (6 ± 1.2 mm^3 and 15.5 ± 4.8 mm^3) between the first and second month (p=0.801), a dramatic increase in their volume appeared at eight months (45.7 ± 4.4 mm^3); (p<0.0001 comparing 1 vs. 8 months and p<0.0002 comparing 2 vs. 8 months) (Fig. 2.5 g). Related to the encephalic volume,

ventriculomegaly was significant in the *taiep* rat (p<0.0001 comparing 1 vs. 8 months; p=0.0007 comparing 2 vs. 8 months) at 8 months (Fig. 2.6 c).
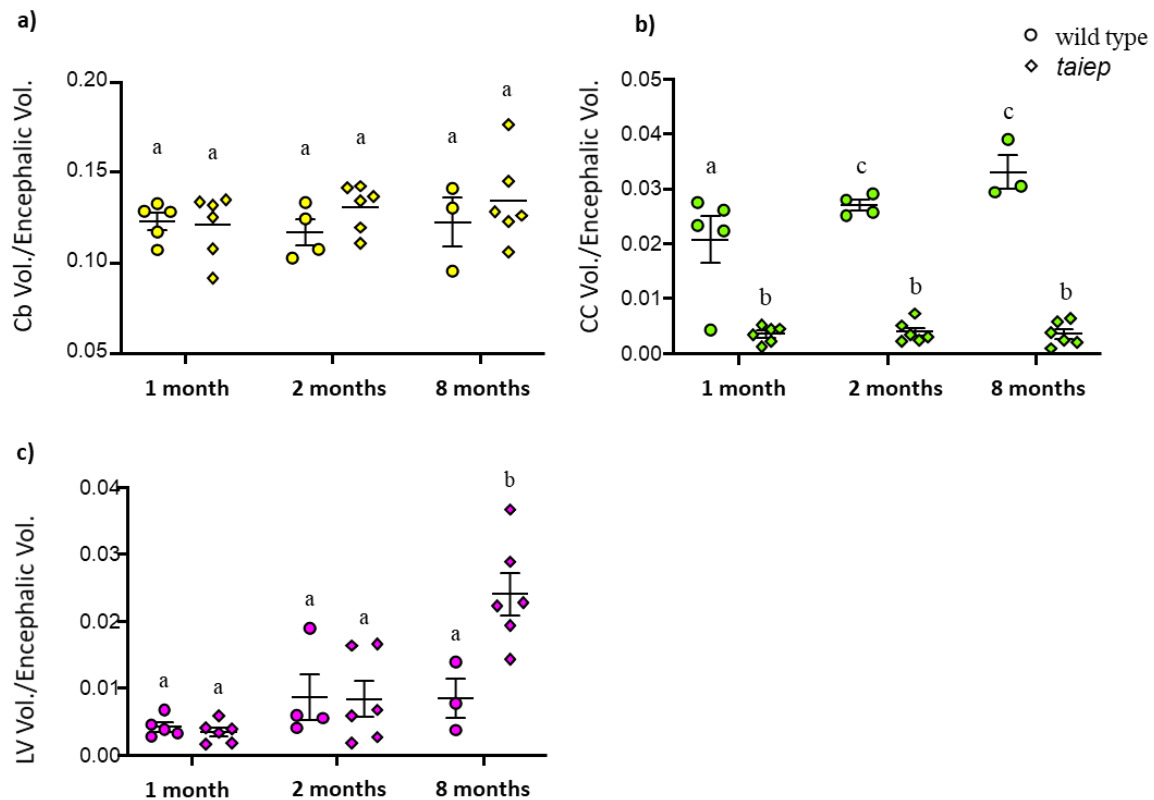

Figure 2.6. Scatter plot of the values of encephalic volume. WT encephalon volume was significantly bigger than that of taiep rats at 2 and 8 months (b). Non-significant differences were obtained for cerebellum/encephalon volume ratio of WT and taiep rats along the analyzed ages (c). The data obtained for each rat are represented by one point in the plot (at least n=3 for group). Two-way ANOVA followed by Tukey's multiple comparison test was performed. Different letters indicate significant differences between groups (b-c).

Discussion

In this study we aimed to discover if radiological features of *taiep* rat's brain were comparable to those seen in H-ABC patients, to determine if this rat was a possible animal model for tubulinopathies. The diagnosis of diseases like H-ABC is a difficult task, in part due to the similitudes with other neurodegenerative diseases and also because, as it was recently described there are few data available to further characterize its pathophysiology. Having an animal model for tubulinopathies will speed up the study of the disease mechanisms and will also represent an opportunity for monitoring the evolution of the disease once pharmacological or genetic therapies are designed. When we put together the motor

problems of *taiep* rats, with the evidence of hypomyelination and demyelination related to a tubulin defect, we see that *taiep* is an adequate animal model for tubulinopathies.

For imaging we used a helium cooled high magnetic induction scanner (7 T), which permitted us to obtain higher quality images than common clinical scanners which usually work at 3 T or less.

The general characteristic of T2 WI in *taiep* rat's brain was a homogeneous high signal across white and gray matter. In healthy individuals myelinated fibers produce low signal in T2 WI. However, in *taiep* rat brains the white matter tracts are almost indistinguishable from their surrounding structures due to their high signal. High intensity in the T2 WI MRI signal is interpreted as a sign of demyelination because as the myelin sheets degenerate, the space once occupied by myelin phospho- and glycolipids is now filled with cerebrospinal fluid and the signal generated from the atrophied fibers becomes more intense as the degeneration progresses.

The identified structures with abnormal MR signal in the CNS of *taiep* rats were: the fibers that cross the caudate putamen, the globus pallidus, the medial lemniscus, the dentate gyrus in the hippocampus the internal capsule, the corpus callosum, the ventricular walls and the cerebellar WM.

The caudate-putamen and the globus pallidus of *taiep* rats are indistinguishable at 1, 2 and 8 months, while images of the control rats of the same age allow the differentiation of those areas. Atrophy of these striatal structures in *taiep* rats has not been previously reported, but is one of the main characteristics observed in H-ABC patients[7] and is important because damage in the nervous network that involves the basal ganglia are related to motor problems like dystonia[59].

Another white matter structure that shows demyelination in MRI of *taiep* rats is the medial lemniscus (ML) which displays high T2 WI signal during the first 2 months and is hyperintense at 8 months. In control rats the ML signal is low because this is a white matter pathway formed by the myelinated axons of second order neurons located in the nuclei gracilis or cuneatus. In *taiep* rats the high signal indicates hypomyelination, which agrees with previous description of the corticospinal tract and fasciculus gracilis of the mutant rats[46].

Partial myelination of the fasciculus gracilis and corticospinal tracts was seen in 2 months mutant rats but no myelin was present by 12 months. The MRI indicates that the demyelination observed in the spinal cord[46,49,60] is maintained along the corresponding pathways, such as the cortico-spinal tract or gracilis tract.

In our MRIs the dentate gyrus is seen as a distinct thin, dark line at all ages in the hippocampus of healthy rats, however, in *taiep* rats it was recognizable only at one month (Figure 3 c). This particular difference could indicate degradation of neurons near this area. Other studies confirm the presence of morphological[61] and physiological[62] changes in the *taiep* hippocampus.

The cerebellum of *taiep* rats has lost all the characteristic patterns of white matter at all analyzed ages. In coronal and sagittal sections, the signal from cerebellar white matter is also homogeneous with respect to the surrounding cerebellar gray matter. Our results showed that cerebellar volume of WT and *taiep* rats remains unchanged during development. Even though, the first anatomical descriptions of the *taiep* rat showed that the cerebellum seems to be atrophic as its weight is 16% lower than in the WT rat [45]. Hyperintense signal from cerebellar WM could be related to cerebellar atrophy that possibly develops during the intrauterine life due to still unknown mechanisms, but it does not advance after birth.

The corpus callosum and the internal capsule in the tubulin mutants display high signal. In healthy animals those structures are formed by highly myelinated fibers and therefore are expected to generate dark areas in T2 WI, as is the case for control rats. The results of volumetric analysis where we report no increment in CC size of *taiep* rats in contrast to the growth experienced by WT rat's brain between their first and second month of life are also coherent with the low contrast obtained in the corpus callosum of *taiep* rats.

Another important finding is related to lateral ventriculi: in *taiep* rats, they showed hyper intensities around them accompanied with an increase in venticulari volume. Encephalic volume loss produces a compensatory enlargement of the cerebrospinal fluid spaces and that is the case with some H-ABC patients[14]. The hyperintensity around ventricles recalls periventricular leukomalacia (PVL). PVL is associated to failure of pre-OL differentiation and as a result hypomyelination[63] and even though it is not possible to identify cystic lesions at any age, there is indeed ventriculomegaly, loss of periventricular white matter and thinning

of the CC, typical signs of PVL, which can also be found in some H-ABC patients. It is possible that both diseases share a common phase during in utero development, when pre-oligodendrocytes suffer hypoxia in PVL and tubulin malfunction manifests itself as deficient myelination around the ventricles and further demyelination[64] during the early life of the patients in H-ABC and also in maturing *taiep* rats.

Anatomical data obtained from the MRI study allowed us to detect and follow in time the macrostructural changes associated to H-ABC. The qualitative and quantitative analysis performed in major structures of the CNS of *taiep* rats produced valuable information for a publication where the *taiep* rat is presented as the first available animal model for tubulinopathies[48]. After that, the volumetric information was compared to new clinical data of a Mexican patient of H-ABC, which was published in a special issue about cerebellar ataxia[14]. After analyzing the progression of the disease using MRI T2 WI from the *taiep* rat with success, we also believe that new information may be obtained from many more MRI applications, including some to deepen the anatomical knowledge of the affected CNS, like MRI diffusion tensor imaging[65] or techniques that could quantitatively estimate the change in myelination levels[66].

Second harmonic generation microscopy

The nonlinear phenomenon of SHG applied to imaging has unique features that make it very promising for medical applications. SHG produces intrinsic contrast from structural protein arrays that are highly ordered and non centrosymmetric, so it is label free[67]. It also has inherent optical sectioning, providing the possibility of three dimensional imaging of native tissue[68,69]. And as infrared light is used for excitation it can produce images deep in optically thick preparations[70]. All those features are necessary for imaging in physiological conditions and are crucial for intravital tissue microscopy[71].

Collagen, muscular myosin, and tubulin are the three non-centrosymmetric biological materials known so far, that form highly ordered arrays which emit SH signals[51]. When tubulin interacts with an intense short laser pulse, it scatters frequency-doubled photons, which can be exploited for label free imaging. The only SHG emitters in the central nervous system are collagen and microtubules[72]. Collagen is abundant in the meninges[73], vessel walls and the choroid plexus[74]; while microtubules, despite being ubiquitous, are highly organized and locally concentrated just in the axons[75]. The SH signal from microtubules depends on their direction (parallel or antiparallel), organization and abundance[52,76]. As SHG is a coherent process, the signals from parallel MTs sum up, while signals from antiparallel MTs interfere destructively. It is estimated that a detectable SH signal arises from bundles of about 50, predominantly parallel microtubules[52].

Applying the SHG technique for the analysis of the CNS could provide a new alternative for the selective imaging of parallel microtubules arrays like those found in axons[77]. In the specific case of the TUBB4A mutant rats there is another structure, besides axons, that is presumably composed of such organized microtubules, the oligodendrocytes. Our animal model for tubulinopathies has an accumulation of microtubules within oligodendrocytes bodies and processes[46,78], which could cause the progressive loss of myelin in the central nervous system. Thus, we expect to obtain different SH signals from mutant and control rats. Recent investigations support that MT bundles that are nucleated in oligodendrocytes processes are highly polarized[79]. However, SHG microscopy has not yet been applied for the imaging of cultured oligodendrocytes and as the amount of parallel microtubules in

oligodendrocytes processes is not reported we could not predict if those bundles of MTs generate detectable SH signal. So far, the groups that have performed SHG in the CNS have not reported oligodendrocytes processes as a source of SHG. The intrinsic polarization of MT bundles in OLGs and the increased number in OLGs of *taiep* rats lead us to hypothesize that detectable SH signal should arise from the defective, mutant cells in *taiep* rats. Therefore, SHG microscopy could be a powerful tool for the examination and analysis of the demyelination process in the CNS.
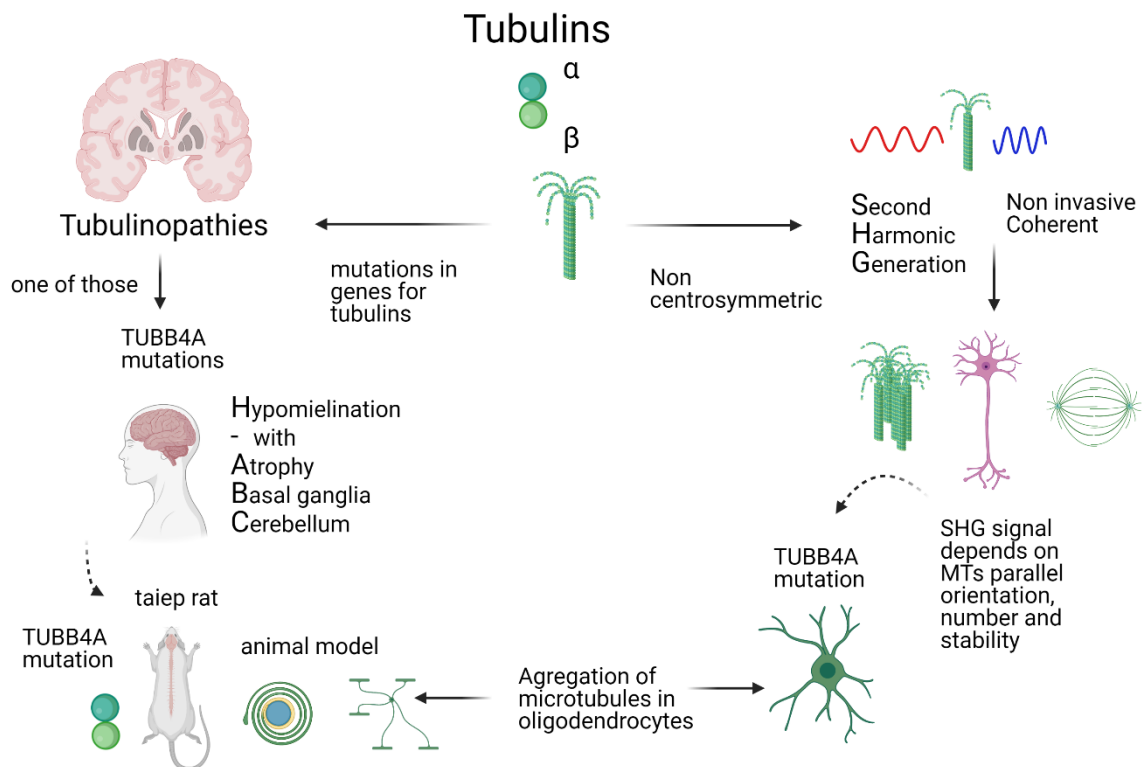

Figure 3.1 *Our hypothesis is that SHG imaging technique could be useful for the study of tubulinopathies in which bundles of parallel microtubules accumulate. Microtubules are the element that connects the technique with the disease, as it is suitable for the selective imaging of microtubules whit the spatial organization that is found in the oligodendrocytes of taiep rats.*

Brief historical background

SHG was demonstrated in 1961 by Franken et al. using a quartz sample as nonlinear medium and by that time the recently invented ruby laser, which provided coherent light at high powers[80]. The laser emitted light of 694.3 nm and after focusing the beam inside a quartz the

emerging light was analyzed by a quartz prism spectrometer observing second harmonic at 347.2 nm.

In 1968 Bloembergen et al. discovered SHG from interfaces[81] and after that it has been widely used for characterizing surfaces and probing physical and chemical dynamics at interfaces[82]. The use of SHG for imaging was first performed by Hellwart and Christensen in 1974, when they observed the crystal structure of polycrystalline ZnSe[83]. In 1986 Freund et al. published the first biological SHG microscopy experiments, obtaining low resolution (~50 μm) images from collagen in rat tail tendon[84]. By 1993 the use of SHG microscopy for the sensing of membrane potential was suggested[85] in an analogous method to surface SHG. Later, the commercial availability of mode locked lasers made possible to implement high resolution SHG scanning microscopes[67]. There are two distinct areas of SHG microscopy development, exogenous staining with fluorescent dyes for imaging cell membranes and endogenous imaging of tissues. Label free imaging has proven to be of high medical interest and the landscape of imageable harmonophores include collagen fibers, actomyosin and microtubules[68].

In the field of medical diagnosis, SHG has aided in the study of pathologies related to collagen disorders in skin like keloids, keratoconus in cornea and liver fibrosis[86–88] and to distinguish between normal and malignant tissues, including colon cancer[89], ovarian cancer[90], breast cancer[91], prostate cancer[92], and malignant thyroid nodules[93]. Imaging of muscle myosin has also contributed to the study of muscular dystrophy and Pompe disease[94,95]. And the SHG imaging of axonal microtubules in an animal model for glaucoma revealed that cytoskeletal deficits predispose axons of the retinal ganglion to atrophy[77].

In addition to these works, other developments are also focused on improving instrumentation technology for practical cinical use, including image processing for the interpretation of nonlinear signals[96,97]. The use of multiple nonlinear phenomena, like two photon, SHG, third harmonic generation (THG) and coherent anti Stokes Ramman scattering (CARS) in a single microscope is also being explored, as such equipment could provide information of multiple structures in samples at the molecular level and in a label free manner[98].

Theory background

A function that is used to describe the response of material to an applied electric field is the polarization P, which is given by[99]

$$P = \chi^{(1)}\, \vec{E} + \chi^{(2)}\, \vec{E}\vec{E} + \chi^{(3)}\, \vec{E}\vec{E}\vec{E} + \cdots \tag{1}$$

The linear susceptibility tensor, $\chi^{(1)}$, describes linear absorption and the refractive index, while higher order susceptibilities are related to nonlinear processes. SHG is a coherent, nonlinear optical phenomena that occurs in materials with a non-zero susceptibility of second order $\chi^{(2)}$. $\chi^{(2)}$ describes the macroscopic response of SHG, sum frequency generation, difference frequency generation and optical rectification, and is non zero only for ordered non centrosymmetric structures. $\chi^{(3)}$ is related to two-photon absorption, third-harmonic generation, and stimulated Raman processes.

Second harmonic generation results from the annihilation of two input photons at optical frequency ω to form one output photon via a virtual energy level.

In general, $\chi^{(2)}$ is a third rank tensor that contains 27 elements, but in the case of SHG, as the two input photons are of the same frequency ω, the susceptibility tensor has the following symmetry.[100]

$$\chi^{(2)}_{iik}(\omega,\omega) = \chi^{(2)}_{iki}(\omega,\omega) \tag{2}$$

which reduces the independent elements of the tensor to 18.

At a molecular level, the light-matter interaction is determined by its dipole moment $\vec{\mu}$:

$$\vec{\mu} = \vec{\mu}_0 + \alpha\vec{E} + \frac{1}{2}\beta\vec{E}\vec{E} + \cdots \tag{3}$$

$\vec{\mu}_0$ is the permanent molecular dipole, α is the molecular polarizability and β is a tensor that describes the first hyperpolarizability responsible for hyper-Rayleigh scattering (HRS). SHG is a coherent addition of the HRS emission from the local molecular ensemble. Then $\chi^{(2)}$ and β are related by:

$$\chi^{(2)} = N_s\langle\beta\rangle \tag{4}$$

Where N_s is the number of molecules involved and $\langle\beta\rangle$ is the orientational average of β.

When dealing with fibrillary structures like microtubules we can assume a single axis of hyperpolarizability for HRS emitters and that this axis coincides with the y' axis of the molecular system of coordinates. Therefore, the only non-zero component of β is $\beta_{y'y'y'}$. With the laboratory system of coordinates (x,y,z) and its y-axis along the axis of cylindrical symmetry and considering that the emitters are oriented at a fixed polar angle ϑ respect to the symmetry axis, only 5 elements of the second order susceptibility tensor are nonzero[100].

$$\chi^{(2)}_{yyy} = N\beta \cos^3 \vartheta \tag{5}$$

and

$$\chi^{(2)}_{yxx} = \chi^{(2)}_{xxy} = \chi^{(2)}_{yzz} = \chi^{(2)}_{zyy} = \frac{N}{2}\beta \cos\vartheta \sin^2\vartheta \tag{6}$$

For an excitation source like a linearly polarized laser beam at an angle ψ with respect to the y-axis (axis of cylindrical symmetry of the microtubule) and that propagates along the z-axis

$$\vec{E} = E \sin\psi\, \hat{e}_x + E \cos\psi\, \hat{e}_y \tag{7}$$

Thus, the polarization can be written as

$$\vec{P}^{(2)} = 2E^2 \sin\psi \cos\psi\, \chi^{(2)}_{yxx}\hat{e}_x + (E^2 \sin^2\psi\, \chi^{(2)}_{yxx} + E^2 \cos^2\psi\, \chi^{(2)}_{yyy})\hat{e}_y \tag{8}$$

And the SHG intensity proportional to the square of the second order polarization

$$I_{SHG} \propto \left(\vec{P}^{(2)}\right)^2 = E^4\left(\chi^{(2)}_{yxx}\right)^2 \left[\sin^2 2\psi + (\sin^2\psi + \frac{\chi^{(2)}_{yyy}}{\chi^{(2)}_{yxx}}\cos^2\psi)^2\right] \tag{9}$$

This equation allows to assess the structural distribution of emitters in a sample. When the SHG intensity is measured as a function of the laser polarization angle ψ, the resulting data can be fitted with

$$I_{SHG} \propto \sin^2 2\psi + (\sin^2\psi + \gamma\cos^2\psi)^2 \tag{10}$$

with

$$\gamma = \frac{\chi^{(2)}_{yyy}}{\chi^{(2)}_{yxx}} = \frac{2}{\tan^2\vartheta} \tag{11}$$

Some values for the angle ϑ in the tubulin dimer have been calculated: Odin et al. obtained an angle of $35 \pm 2°$ for microtubules in axonemes[101] and Psilodimitrakopoulos et al. calculated an angle of 33.96° with a width of 12.85° for microtubules in culture cortical neurons[102]. In other work involving ischemic cultured neurons, Psilodimitrakopoulos et al., calculated a change in the angle from 44.3° to 47.1° after 120 minutes of oxygen and glucose deprivation[103]. Kaneshiro et al. (2019) analyzed purified microtubules in solution, estimating a mean angle of 38.5° and a mean value of 39.7° in taxol stabilized microtubules; they also observed a difference in conformation for microtubules decorated with binding proteins (38.7°) and also microtubules decorated with the binding proteins and in the presence of taxol 39.3° [104].

Technical requirements for SHG microscopy

Laser Source

Nonlinear transitions probabilities are low compared to optical linear phenomena, and therefore to achieve excitation that produces enough signal to be detected, a high spatial and temporal density of photons is necessary[105]. Femtosecond pulsed lasers can assure a high amount of photons concentrated in a short time and when focused with a high numerical aperture objective, the small volume where light is concentrated completes the demands for the SH phenomenon to occur. Typically, the excitation wavelength is chosen in the near infrared to exploit the inherent reduced light scattering and absorption and allow for deep tissue penetration (> 500 µm).

Objective lens

The excitation objective lens will determine the spatial resolution of the imaging system. In a nonlinear scanning microscope, the spatial resolution is given by the excitation volume, which is smaller than the diffraction limit because of the nonlinear optical properties of the excitation process. Even though, an approximation for spatial radial and axial resolution is given by[70].

$$\omega_{xy} = \begin{cases} \frac{0.320\lambda}{\sqrt{2}NA} & NA \leq 0.7 \\ \frac{0.325\lambda}{\sqrt{2}NA^{0.91}} & NA > 0.7 \end{cases} \qquad (12)$$

$$\omega_z = \frac{0.532\lambda}{\sqrt{2}} \left[\frac{1}{n - \sqrt{n^2 - NA^2}} \right] \qquad (13)$$

Where λ is the excitation wavelength used, n is the refractive index of the immersion medium, and NA is the objective numerical aperture.

Other important characteristics to be considered about the objective lens are its transmittance for the excitation wavelength used, its numerical aperture, and the working distance. Choosing an objective with NA higher than 0.5 is recommended to provide enough density of photons in the focus for the nonlinear process to occur[100] and the working distance should be elected according to the thickness and morphology of the sample to be imaged.

Forward and backward detection

SHG is a coherent process, therefore most of the generated signal should have the same direction as the exciting wave vector. The phase of the SH light is related to the phase of the driving fundamental light[106]. The total radiated harmonic power depends on both the spatial distribution of the molecules and of the driving field. The molecules that contribute to SHG should not be considered as independent sources because the signal of all the emitting molecules may interfere, and according to their distribution the signal may add up or may be destroyed.

Some uniaxial birefringent crystals like potassium dihydrogen phosphate (KDP) or beta barium borate (BBO), illuminated with an appropriate angle of incidence and the right polarization can meet ideal phase matching for SHG, which is $\Delta k = k_{2\omega} - 2k_\omega = 0$, where $k_{2\omega}$ is the wave vector for SHG photon and k_ω is the wave vector for the incident photon. When this condition is fulfilled, the radiation emitted is 100% forward propagating[100]. In general, this condition is not fulfilled for tissues but it has been observed that in tissues there is backward emitted SHG, which requires strong axial momentum contributions. A relaxed phase-matching condition has been developed by LaComb et al. for collagen in tissue. Their model includes contributions from quasi phase matching and additional phase mismatch due to dispersion and randomness[107].

The ratio between forward and backward emitted SHG signal ranges from 1 to 10^{12}, depending on the distribution and directionality of the induced dipoles within the focal volume[70].The pattern of the forward emitted light displays two lobes that form an angle with respect to the optical axis[106]. Ideally, the objective lens used for detection should have a higher NA than the excitation objective so that all emitted SH signal is collected.

In general, the amount of SHG backward emitted signal is much lower than the forward emitted signal. But, when imaging biological tissue, the multiple backscattering events that occur in such scattering media generate backward signal that ranges from 5% to 20% of the forward emitted signal[100].

For backward detection, the transmittance of the objective should be optimal for IR and SH generated light.

Filters

The use of three elements: a short pass filter, a narrow band pass filter and also a dichroic mirror is advised. Short pass filters block spurious contamination of the excitation light in the detection path. Filters that block IR excitation light usually have a cutoff wavelength between 650-700 nm; these kind of filters allow fluorescence and SHG signal to pass, which could be desired as two photon fluorescence signal may also be detected.
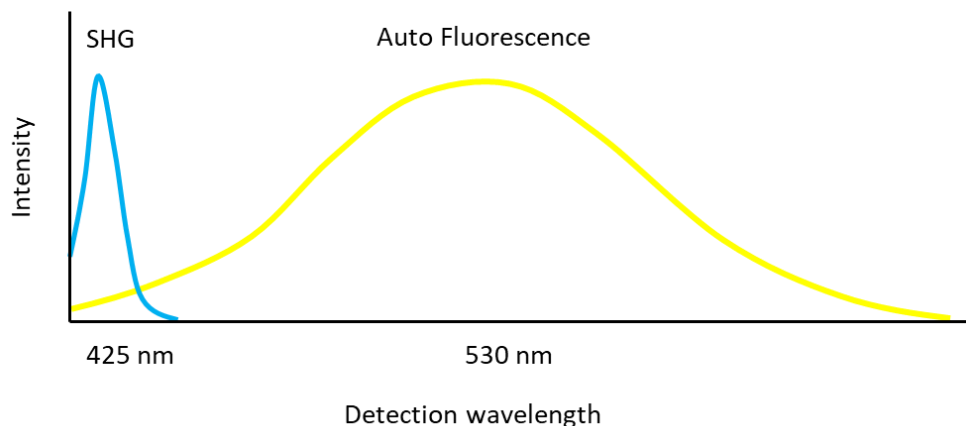

Figure 3.2 Typical emission spectra of a primary hippocampal cell culture obtained with an excitation wavelength of 850 nm. The SHG spectra is centered at half the excitation wavelength. The autofluorescence spectra is a broadband centered around 530 nm[76].

Two photon excitation (TPE) is also a nonlinear process, but this is different from SHG as in TPE two photons are absorbed in order to take the molecule to an excited state, instead than a virtual state as in SHG; as a consequence of absorption the emitted photon has lower energy than the sum of the two photons used for excitation. TPE is a third order nonlinear process that depends on the third order nonlinear susceptibility (χ^3).

A band pass filter centered at half the wavelength of the excitation wavelength and with a width of about 20 nm is convenient to selectively detect SHG (Fig. 3.2)[100]. The dichroic mirror diverts the SHG light to be detected and may be needed depending on the imaging setup.

Detector

The most common type of detector used for SHG microscopy is the photomultiplier tube (PMT). A PMT is a vacuum tube, usually made of glass that converts very small light signals into a measurable electric current. It consists of a photocathode, a number of dynodes and an anode. A photon ejects an electron from the photocathode. An electrical field in the PMT accelerates the electron into another surface called a dynode. The collision of the electron with the dynode releases several new electrons, which are accelerated into another dynode. This process is repeated several times producing a typical electron gain of $\sim 10^6$ [108].

Other types of detectors are avalanche photodiodes, microchannel plates, charge coupling devices arrays and PMT arrays.

Materials and methods

Optical system

A LSM-710-NLO AxioObserver Z1 confocal microscope (Zeiss, Germany), and a Chameleon Vision II titanium sapphire tunable laser (680-1080 nm, 140 fs, Coherent) were used for imaging. Light was focused with a plan-neofluar 25X/0.8 Imm Korr DIC M27, a plan-apochromat 63X/1.46 Oil Korr immersion objectives and an epiplan neofluar 50X/0.55 dry objective (Zeiss, Germany). The SHG was collected in the transmission direction (forward path) with a 0.5 N.A. condenser (Zeiss, Item no.: 424242-0000-000) or in reflection mode with the same objective used for excitation. The wavelength used for excitation of the samples was 810 nm and detection was performed after a short pass filter (SP 485) with

photomultiplier tubes (Hamamatsu, Japan) in the non descanned (ND) detection, either in transmission or reflection mode. A single band –pass filter centered at 405 nm and a width of 20 nm (Semrock, FF01-405/10-25) was used to selectively detect only photons involved in SHG in the forward direction. The descanned detection reflection pathway was also used for selected imaging experiments, in that case the detector was the Zeiss LSM meta. In some experiments a half wave plate was inserted before the objective to rotate the polarization of the excitation laser beam. Imaging power was measured with a power meter (PMD100D, Thorlabs, USA).

Pseudo-bright field images were generated with residual 405 nm laser light captured in transmission by an external non descanned detector (NDD) of the LSM 710 Zeiss confocal microscope.

Nonlinear crystal and glass

A Beta barium borate (BBO) was imaged with the 50X objective in the ND transmission path with a laser power of 1.3 mW, and in the descanned reflection mode with a power of 14 mW.

Starch

Corn starch was imaged with 25X, 50X and 63X using the three different detection paths. Also, the sample was mounted in three different manners: 1) placed between a glass slide (~ 1 mm thick) and a coverslip (~0.17 mm thick), 2) placed between two coverslips and 3) placed over a coverslip and not covered. Laser powers between 2.5 and 30 mW were used for imaging.

The high SH intensity generated by starch together with the simple mounting and handling of the sample allowed us to use it for some experiments using the half wave plate to rotate the linear polarization and verify the effect of excitation polarization.

Cells

Living HeLa cells (CCL-2, ATCC) and Immortalized Multipotent Otic Progenitor (iMOP) cells were imaged (donated by Dr. Kelvin Kwan). Cells were cultured in glass bottom dishes, the media used for culture was removed and replaced with phosphate buffered saline (PBS) to avoid noise from autofluorescence of colored media. The PBS volume used for imaging

was enough to keep cells hydrated during imaging but low enough to form a thin layer of PBS. The PBS film used was equivalent to ~40 uL for a 0.78 cm^2 surface well.

Collagen and myosin

Acute tissue sections of gastrocnemius and biceps muscles of mice and rats were isolated and then sliced in a vibratome (Leica VT1200, USA), obtaining 200 and 400 um-thick sections. The sections where placed between two coverslips for imaging. The tissue was imaged using the three detection paths and 25X, 50X and 63X objectives. Laser powers used for imaging ranged from 19 to 34 mW.

Central nervous system tissue

Brain, cerebellum and spinal cord of adult mice and rats were imaged. To obtain the acute sections, rodents were anesthetized with a mixture of ketamine–xylazine (0.125 mg/Kg and 5 mg/Kg, IP), and then sacrificed by decapitation. The brain and cerebellum were removed and separated into two halves. One half was immediately immersed in 4% formaldehyde in PBS for immunohistochemical processing. The second half was used for SHG imaging, obtaining acute coronal brain slices of 160 μm. The unfixed tissues were immersed in HBSS at 37°C to prevent microtubules depolymerization during the time between sectioning and imaging.

Image Processing

The open source FIJI software[109] was used to convert and reconstruct the images as well as to perform the intensity analysis.

Results

Characterization of the optical system

The goal of the first part of this study was to understand the capabilities and limitations of our imaging system with respect to SHG microscopy.

The Zeiss LSM NLO 710 nonlinear laser scanning microscope was used for imaging. One positive aspect about using a commercial system is that the protocols and findings described here may be replicated by any institution that has the same system, or another commercial set-up with similar characteristics, which is very likely the case for many biomedical laboratories around the world.

Table 3.1 Characteristics of the pulsed laser[110]

Chameleon Vision II	
Tuning range	680 to 1080 nm
Average power at peak	3.0 W
Pulse width	140 fs
Polarization	Horizontal >500:1

The system has three available detection paths as is depicted in figure 3.3, which gave us alternatives for signal detection. The set up itself is an inverted microscope and therefore, the objectives are placed under the samples and illuminate it from below. In this configuration the transmitted light is detected in the upper photomultiplier NDD T (Fig 3.3 a). For backscattered detection we had two options: to use the shortest path which corresponds to NDD R or to use the internal detectors that are located after a longer light path with more optical components (LSM) (Fig. 3.3 b). The laser used for imaging was a Chameleon Vision II, which is a tunable titanium sapphire pulsed laser of 3W of power at 810 nm (Table 3.1). The laser is diffracted by an acousto-optic modulator (Fig 3.3 a, red arrow) and the first order is coupled into the microscopy system for excitation.
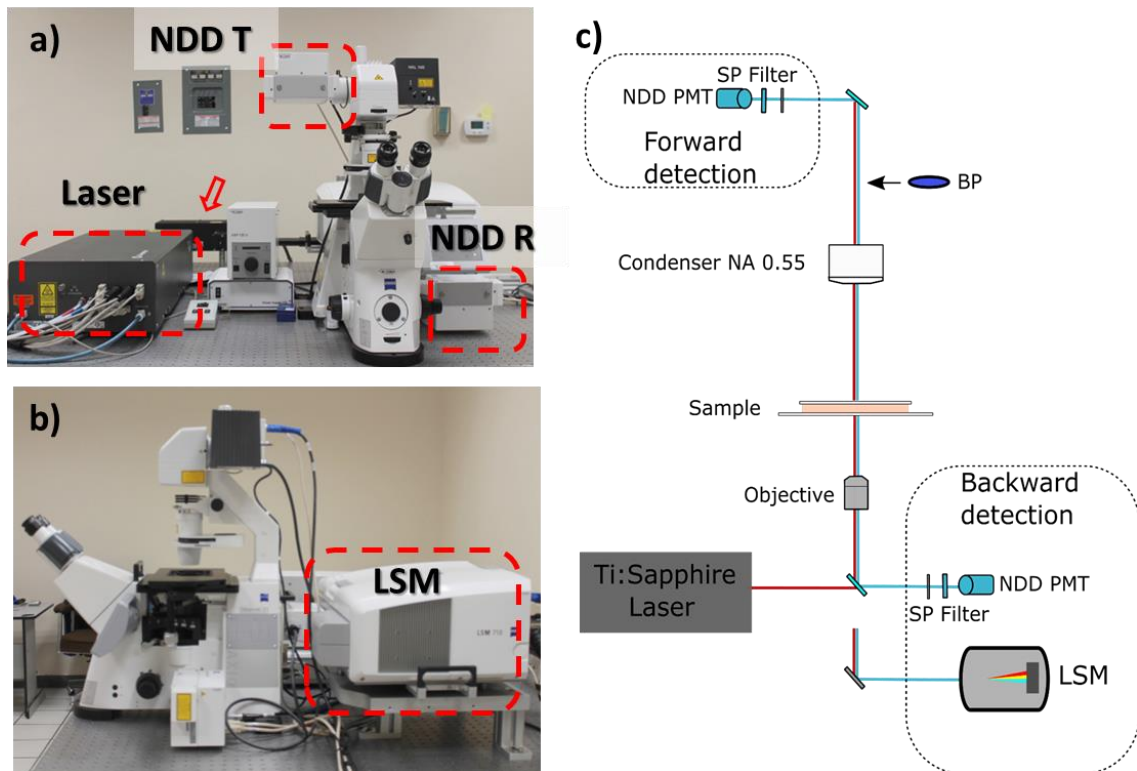
Figure 3.3 *Imaging system used for SHG microscopy. a) Frontal view of the microscope. The laser, the acousto-optic modulator (red arrow) and the photomultiplier detectors of the nondescanned (NDD) paths in transmission (T) and reflection (R) positions are marked. b) Lateral view of the microscope where the position of the detector in the descanned path is visible (LSM). c) Schematic representation of the optical system. The red lines represent the excitation light and the blue lines the SHG light. NA = numerical aperture, BP= band pass and SP=short pass. A narrow band pass filter was positioned between the condenser and SP filters (arrow) to eliminate autofluorescence.*

Most commercial microscopes are closed systems, with access ports to very few portions of the optical path. In our case, measuring the power of the laser is possible only at the back focal plane of the objective. Knowing the power of the laser beam at the back focal plane of the objective would be important because this value is necessary for the estimation of intensity at the sample. We measured this power using the excitation laser but removing the objective which allows the access to the beam that reaches the back aperture of the objective (Table 3.3). The laser power used for imaging is controlled by the software, the user simply selects the percentage to use. As the laser is tunable, its power curve describes the highest possible power for each wavelength. From the beginning of our study we used 810 nm for excitation, because at that wavelength the laser has its highest power values and also because, as it is a common value used for biological SHG imaging[76,102,104], our results could be more

comparable to the results of other groups. For that reason, we periodically measured the laser power at 810 nm for different percentages selected in the software and including the maximum power for imaging. During the first years of the investigation the maximum available power for imaging at 810 nm was 130 mW but in the last year a reduction was detected (Table 3.2). The reduction was associated to temperature fluctuations and increased humidity in the laboratory.

Table 3.2 Average laser power of Chameleon laser at 810 nm

Software: Laser power %	Measured Power (mW) 2018-2019	Measured Power (mW) 2021
5	7.5	6.4
10	12.6	10.2
20	24.5	18.6
50	60	42.9
100	130	95.5

The original, maximum laser power was 130 mW, but a drop in the maximum usable laser power was detected at the beginning of 2021. To compensate for the drop in power we selected higher percentages of the available laser power. The laser beam is horizontally polarized and therefore the images reflect the effect of using linearly polarized light in the horizontal direction (Fig 3.5 c-f).

Knowing the laser power allowed us to calculate the intensity at the sample. The intensity $\langle I \rangle = \frac{\langle P \rangle}{S}$ was calculated considering $\omega_{xy} = \frac{0.325\lambda}{\sqrt{2}NA^{0.91}}$ for NA above 0.7 and $\omega_{xy} = \frac{0.320\lambda}{\sqrt{2}NA}$ for NA below 0.7.

Table 3.3 Intensity at the sample for an average power of 10 mW

Objective	NA	Intensity (MW/cm^2)
25X	0.8	6.12
50X	0.55	2.87
63X	1.46	36.6

To proceed with the characterization of the imaging system, a sample suitable for SHG microscopy testing was necessary.

First we considered to use a non-linear crystal. The Beta Barium Borate (BBO) nonlinear crystals were discovered in 1984[111] and since then they have become a popular nonlinear material used for SHG. BBO has a wide transparency region, broad phase-matching range, large nonlinear coefficient and high damage threshold. A BBO crystal was used to test the system by acquiring images in the reflection and the transmission mode (Fig 3.4 a, b). The power used for imaging in the backward geometry was eight times the power used for imaging in the transmission path. And even so, the image obtained from backscattered signal had lower signal compared to the image obtained in transmission. The bright field image revealed that the surface of the crystal had some dust or dirt particles (Fig 3.4 c) that are also evident in the SHG micrographs.
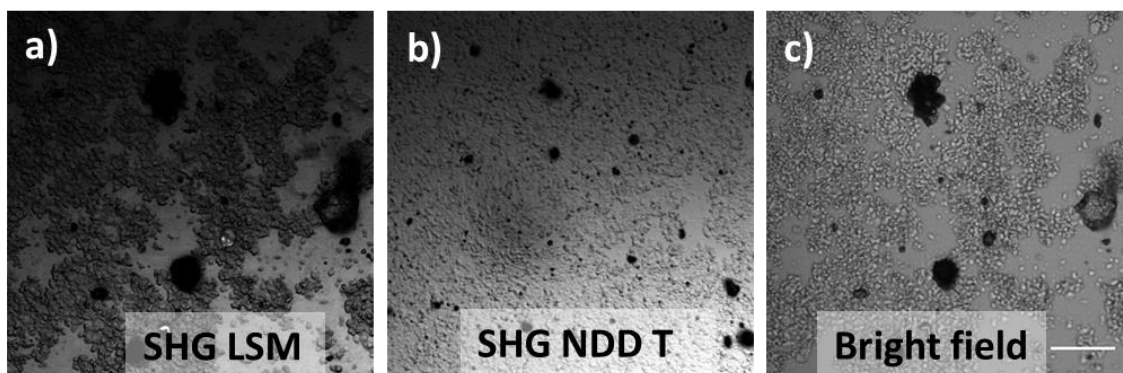

Figure 3.4 *Imaging of the beta barium borate crystal. a) Image obtained with the backscattered signal using the descanned path; the power used was 10.8 mW. b) Image obtained with the transmitted signal using the non descanned path, the power used was 1.3 mW. c) Bright field image of the crystal showing that the surface carries dust and dirt that was also seen in SHG images. The beam was focused with a NA 0.55 50X objective. Scale bar: 30 μm.*

The nonlinear crystal was placed directly on the sample holder with no need for a previous mounting in a coverslip as is usually the case for biological samples.

We then examined another type of sample, starch, which requires mounting and so the objective space architecture resembles more closely the one that has to be used for biological samples.

There are many different types of starch granules: the major starch sources are cereals and tubers. In this work we used a commercial corn starch (Maizena) commonly available in grocery stores. The granules of starch are composed of ~20% amylose and ~80% amylopectin, and they are known to generate an intense optical second harmonic signal[112]. The granules have an inner organization of alternating rings of crystalline and amorphous structures (120-400 nm thickness) that originate from the hilum[113] this ordered arrays of chiral glucose molecules are the source of SH signal[114].

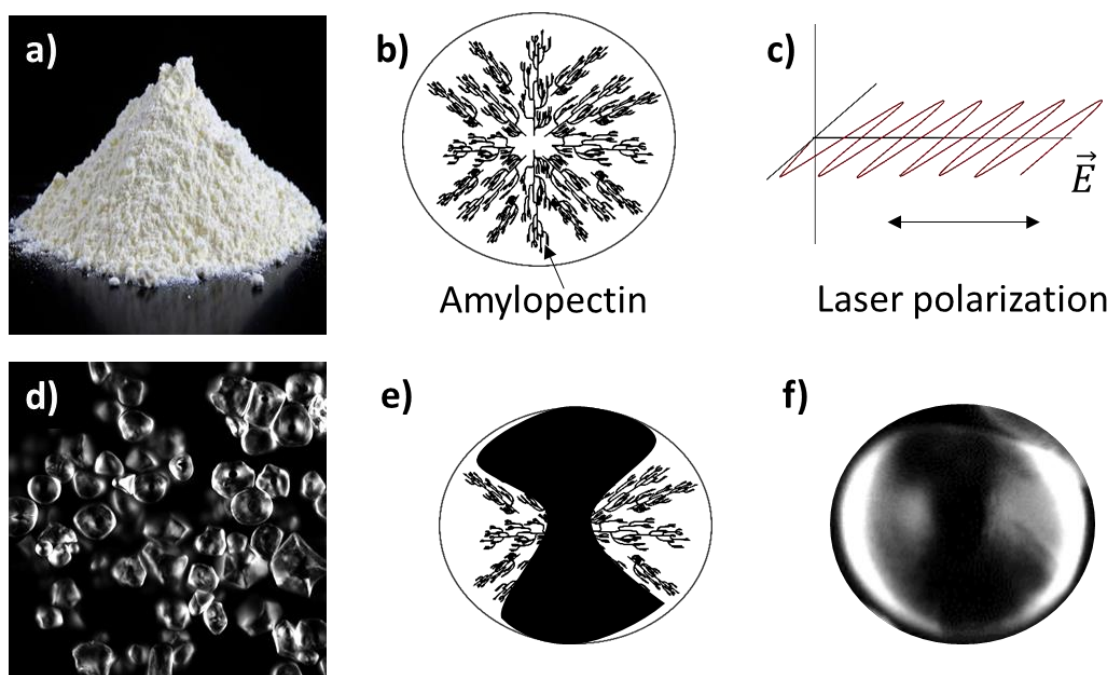*Figure 3.5 Starch granules imaged by SHG microscopy. a) Photograph of corn starch before mounting for imaging. b) Representation of the radial distribution of amylopectin in a starch granule. c) Representation of the horizontal polarization of the laser. d) SHG micrograph obtained from starch granules mounted between a glass slide and a coverslip. e) Representation of the amylopectin distribution where bright areas seen in SHG correspond to regions where the polymeric distribution aligns with the laser polarization, and dark areas correspond to regions where the polymer is oriented in a transversal direction with respect to the laser orientation. f) Magnification of a granule in (d) where the signal distribution described in (e) is observed.*

Starch granules were conventionally mounted between slide and coverslip; the highest magnification objective (63X) was used and the signal was collected in transmission (Fig 3.5 a, b). The images obtained from the granules had a characteristic pattern of signal distribution (Fig 3.5 d), with dark and bright areas. In each granule, the center, and the upper and lower parts were dark while the lateral areas were bright (Fig 3.5 e, f), this pattern corresponds to

starch imaged with a beam of linearly polarized light oriented horizontally (Carriles 2009, Zhuo 2010). The SHG intensity in each pixel depends on the net orientation of the non-linear dipoles and the polarization of the laser beam.
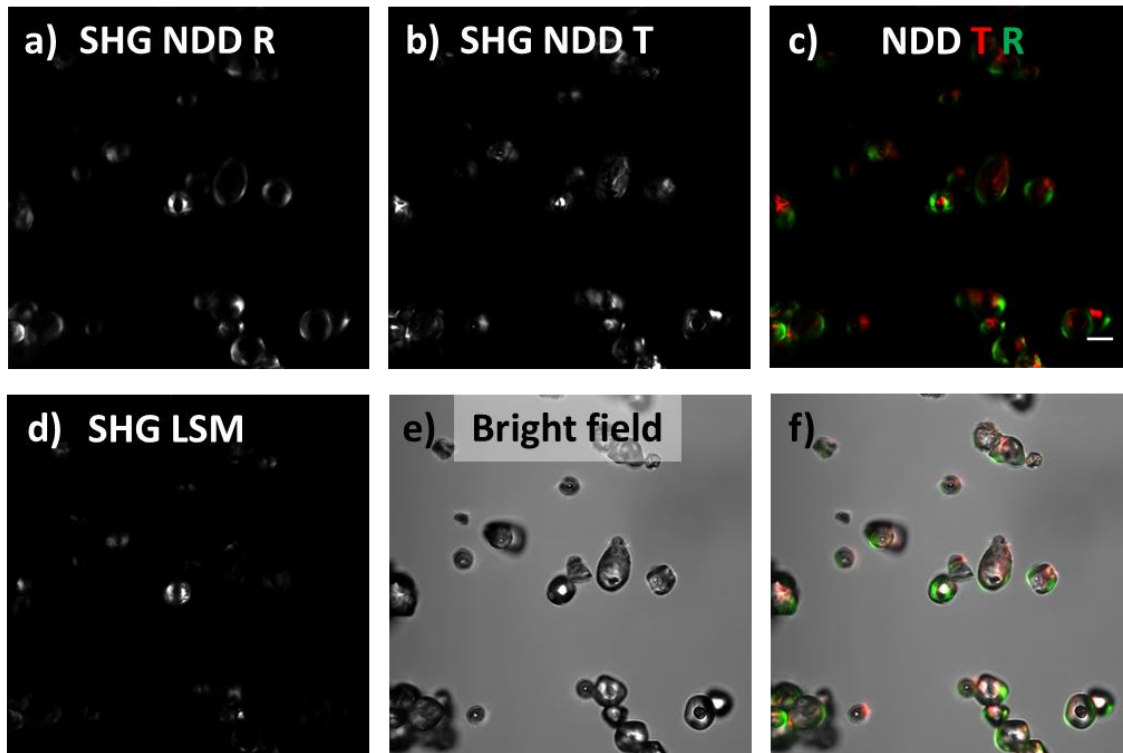

Figure 3.6 Differences in SHG images from corn starch obtained with three alternative detection paths. a) Micrograph obtained in the backward direction and in the non descanned path, the laser power used was 5.4 mW. b) The same field of view as in (a) imaged in the forward direction in a non descanned path, the laser power used was 8.4 mW. c) Merge of images obtained in forward in red and backward direction in green. d) Same fied of view as in (a) imaged in the backward direction in the descanned path, the laser power used was 9.6 mW. e) Bright field micrograph of the granules where their whole shape is observed. f) Merge of the bright field with the image in (c). The scale bar is 10 µm.

The SHG signal in forward and backward directions was also tested by imaging starch. We expected to obtain similar images in both forward and backward paths, but the images obtained suggests that focal planes imaged in both configurations do not fully coincide (Fig. 3.6 a, b, c). Micrographs obtained from backscattered SHG in descanned and non descanned paths are neither the same; but in this case the main difference appears to be the intensity levels of the features: the image obtained from the nondescanned path has more intense signal than the image obtained from the descanned path (Fig 3.6 a, d). It was useful for us to also

obtain a bright field image from the granules and merge it with the SHG images obtained. From the merge we can identify the hilum and complete borders of the granules, which shows that both images, whether they were obtained in transmission or reflection have the lobular distribution of light but that it comes from different focal planes (Fig 3.6 f).

The possibility of obtaining images of SHG in two perpendicular directions was explored from two different perspectives. By rotating the sample after imaging and re locating the same field of view, and by the use of a half wave plate placed in a space available in the excitation path, just before the objective.
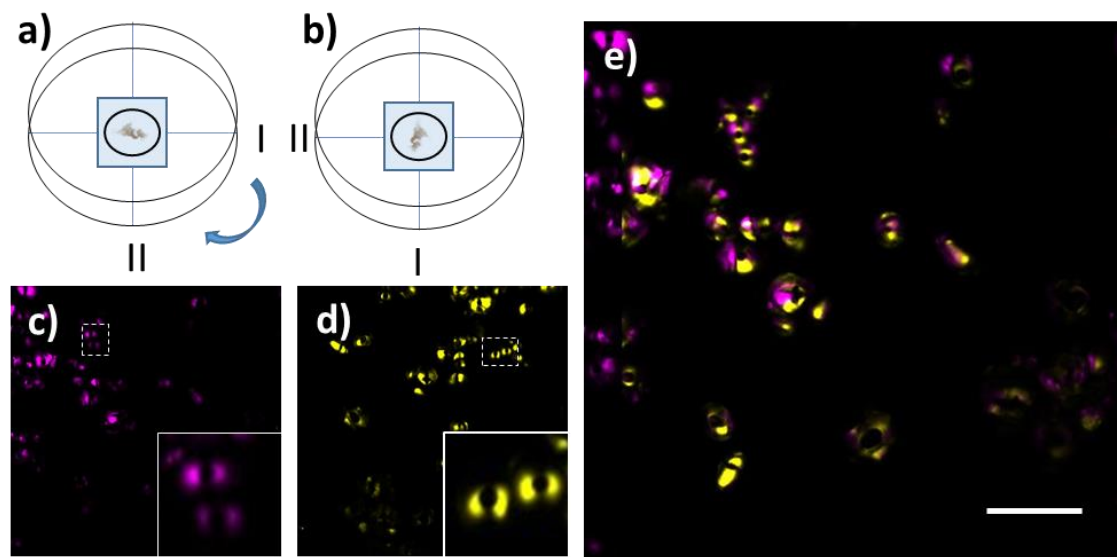

Figure 3.7 *Imaging of corn starch verifies the horizontal linear polarization of the laser. a) Glass bottom dish containing starch. b) The same glass bottom dish of (a) rotated by 90°. c) Starch grains of different sizes display a characteristic signal in position same as (a). d) Image obtained from corn starch of the same field of view of (a) rotated 90°. e) Merge of image (c) in its original direction and (d) rotated 90°. Images were obtained with the transmitted signal using the non descanned path, the power used was 28.8 mW. The scale bar is 30 μm.*

To be able to rotate the sample by 90° circular dishes were used. And as plastic is a birefringent material that could interfere with the imaging, the plastic dish was modified to have a coverslip glass bottom (Fig 3.7 a, b). A very small amount of starch was added to the well and the dish was gently shacked to disperse the granules. After placing the dish in the sample stage and trying to place it in the center, marks (lines) were made on the sides of the well to indicate the actual position. After obtaining the first image, the dish was rotated by 90° and the same field was imaged (Fig 3.7. c, d). Image processing was required to obtain

the merge of both images: first they were rotated and then also translated to have a good fitting of the positions. As this process requires to relocate the same region for imaging, marks on the coverslip are helpful to re recognize the same area.
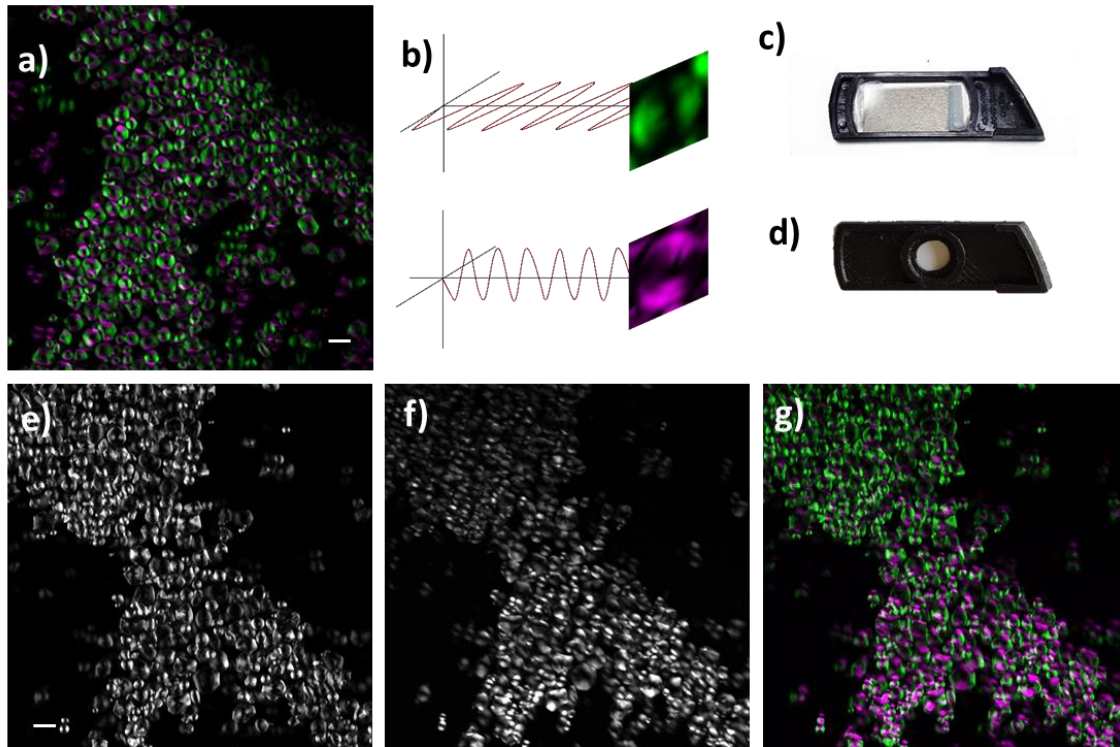

Figure 3.8 SHG signal from starch granules using two types of half wave plates. a) Merge of two images obtained with horizontally (green) and vertically (magenta) polarized light. The horizontal polarization was the original beam (no HWP used) whereas the vertical polarization was obtained by inserting a plastic HWP before the objective. b) Magnification from a single granule depicting the effect of linear polarization. c) Mount where the plastic HWP was placed and which was inserted right before the objective, in the objective revolver. d) 3D printed mount for the use of a quartz HWP. e) Micrograph obtained without the use of a wave plate. f) Micrograph obtained after inserting the quartz HWP (d) before the objective. g) Merge of (e) and (f). Images obtained in the NDD T path and their scale bar is 20 μm.

In the objective revolver there is a black holder under every objective. This piece is removable (Fig 3.8 c) and the laser beam used for excitation passes through its window. First, we used a plastic HWP attached to the piece of the microscope objective revolver (Fig 3.8 c) to image starch in a perpendicular direction, compared to the original orientation. The images obtained indicate that horizontal polarization was rotated to vertical polarization (Fig 3.8 a, b). We also printed a modified version of the removable piece designed to hold a circular HWP of a diameter of 1 cm (Fig 3.8 d). The image obtained with the HWP had the pattern predicted for vertically polarized light (Fig 3.8 e, f, g). Unexpectedly, the signal intensity

decayed when the HWP was used and also the image was unevenly illuminated (Fig 3.8 g). The diminished signal intensity may be a consequence of a reduced diameter of the excitation beam due to the aperture imposed by the printed piece used for holding the; HWP, in addition, the position of the aperture could not be precisely centered respect to objective axes and this could as well impair excitation.

As we were using a system that collected light with a condenser rather than a matching objective, we decided to test if the position of the condenser and its apertures could have an impact on image detection.

We realized that images with the highest intensity were obtained when the height of the condenser was set according to the Köhler position for the objective to be used, and that when the condenser was at its lowest position the images obtained were less intense (Fig 3.9 a, b, c). Another optic path element that has to be set for SHG imaging is the aperture diaphragm. In order to observe transparent samples through the oculars, it is common to set the condenser's aperture diaphragm (Fig 3.9 d) to less than half of its diameter, because it improves contrast, but for SHG imaging it has to be fully opened to collect the most of the SHG signal produced. To measure the effect of diaphragm aperture on signal intensity, an image of the same field of view was taken under three different conditions: the first corresponds to the control image obtained according to Köhler illumination, (Fig 3.9 e and h, blue line), in the second condition, the field diaphragm was fully opened without an impact on image intensity (Fig 3.9 f and h, yellow line), and in the third also the aperture diaphragm was fully opened which increased signal intensity (Fig 3.9 g and h, red line).

Before imaging, the height of the condenser and the aperture of the iris diaphragm were set on position for SHG microscopy.
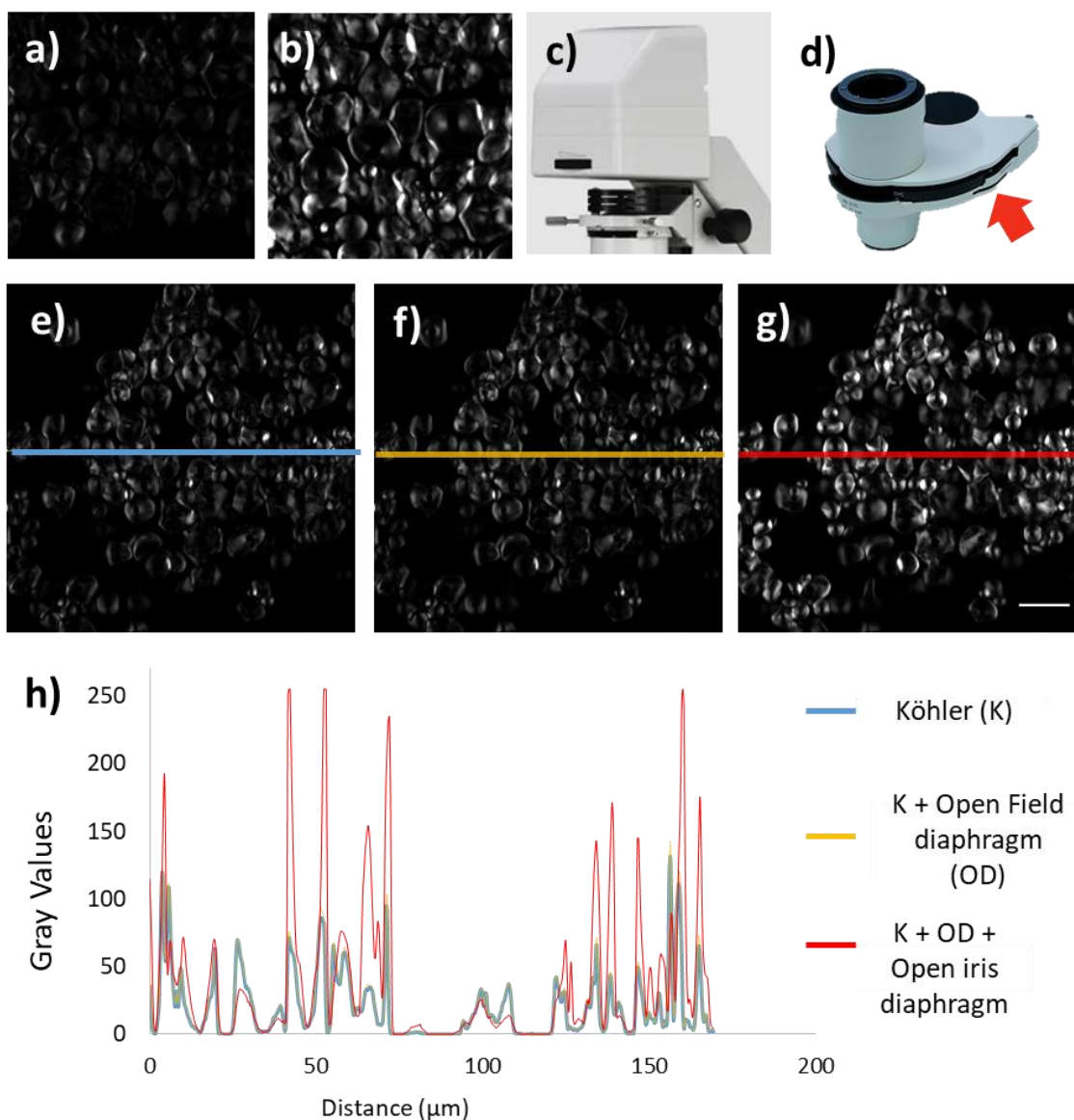
Figure 3.9 *Effect of Köhler alignment and aperture of the Iris diaphragm on SHG signal. a) Image obtained with the condenser placed at its lowest position. b) Image obtained with the condenser placed according to the Köhler illumination. c) Condenser and field diaphragm control wheel. d) The red arrow points to thecontrol wheel used to open the aperture (Iris) diaphgram. e) Image obtained with the condenser located according to Köhler alignment. f) Image obtained with the correct altitude of the condenser and the field diaphragm completely opened. g) Image obtained with the correct altitude of the condenser, the field diaphragm completely opened and the iris diaphragm completely opened. h) Intensity plot of the pixels along the line marked in (e, f and g). A higher signal is obtained when the condenser´s altitude is elected by Köhler alignment and when the Iris diaphragm is completely opened.*

The SHG intensity from starch depends on the concentration of amylopectin in the focal volume and on the excitation intensity. When imaging starch granules with increasing excitation intensity, the SHG signal also increased (Fig 3.10 a). We obtained one image per

laser excitation (0.7-2.5 mW) and selected an area to measure the gray values obtained with increasing excitation intensity (Fig 3.10 b). The gray values of each pixel in that area are averaged. For the first six average powers the gray values increase slowly but the increment for the last value is 6.5 times the previous gray value. This rapid change in intensity could be related to the quadratic relation between excitation intensity and SHG intensity. More experiments and data should be obtained to better fit that relation. We did not perform more experiments to test that relation. We were more interested in understanding the common average powers to be used in our system, since across publications of SHG imaging from starch there are many combinations of power and objectives used. To list some, Zhuo et al used a NA of 1.42 and power below 100 mW[115], Psilodimotropolous et al. used a NA of 1.4 and a power of 10 mW[116], Chen and others used powers between 60-70 mW with an objective of numerical aperture 1.2[117] and Mazumander et al. used a power of 3 mW combined with an objective of NA 1.3[118]. For SHG imaging of starch we commonly used the following combinations, 25X/0.8 NA with an excitation power of 2.5 mW, 50X/0.55 NA with a power of 10 mW and 63X/1.46 with a power of 3.4 mW. No photodamage was observed in the sample when using powers below 10 mW.
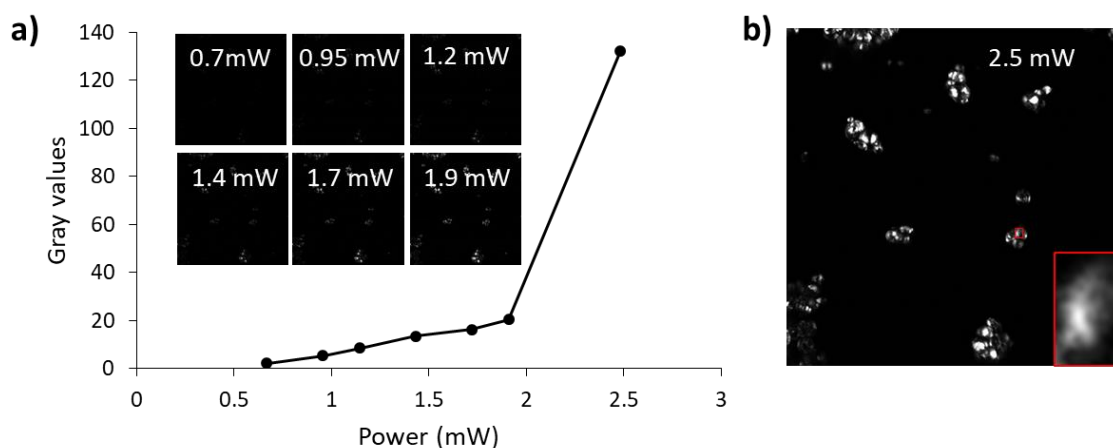

Figure 3.10 *Image intensity and average excitation power. a) Plot of measured gray values according to increasing excitation power. Insets in (a) are the images obtained with the power indicated in each image, and that correspond to the first six points in the plot. b) Micrograph that corresponds to the last point in the graph (2.5 mW and 130 gray value) in (a), the region used for measuring the gray values is highlighted in red.*

Working with biological samples
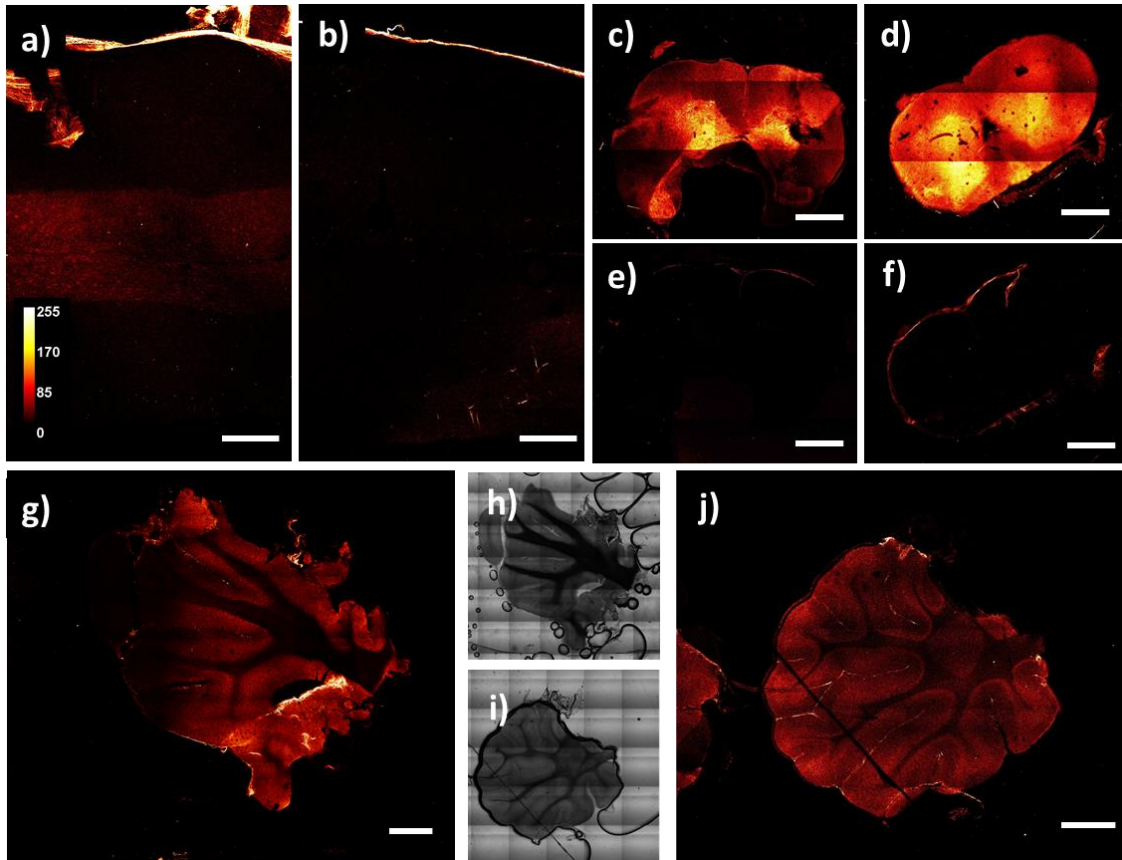
Fixed CNS

Figure 3.11 *SHG images of fixed spinal cord and cerebellum. a) Longitudinal section of the spinal cord of a Sprague Dawley (SD) rat imaged in the forward direction. b) Longitudinal section of the spinal cord of a taiep rat imaged in the forward direction. c) Transversal section of the spinal cord of a SD rat imaged in the backward direction using the descanned path. d) Transversal section of a SD rat imaged in the backward direction using the descanned path. In (c) and (d) the detection of LSM is adjusted to 430-500 nm, away from the expected SH signal (405 nm). In (e) and (f) same spinal cord sections of (c) and (d) respectively, with the detection of the LSM adjusted to 395-415 nm. g) Sagittal section of SD rat cerebellum imaged in the forward direction. h) Pseudo bright field image of same section in (g). i) Bright field image of a sagittal section of taiep rat cerebellum. j) Same section as (i) imaged by SHG in the transmission path (NDD T). Scale bar in (a) and (b) is 500 μm, in (c) to (g) is 1000 μm.*

One of the major advantages of using nonlinear microscopy for the study of biological samples is that it is label-free, giving the possibility of *in vivo* imaging[71]. Even though, imaging living cells has its own difficulties, because they are more prone to thermal damage and sample deterioration, and also endogenous signal is usually less intense than fluorescence from exogenous markers. To find out how to overcome these limitations and determine the best possible imaging conditions in our system, we imaged a variety of tissue sections. We

decided to first image fixed sections of the central nervous system of rats. It is known that collagen and myosin fibers still generate SH after fixation, but PFA fixed microtubules do not. By imaging unlabeled fixed tissue sections, we expected to learn about possible endogenous non linear signals.

The SHG images from spinal cord and cerebellum indicate that collagen from the meninges is able to generate a strong nonlinear signal after fixation (Fig 3.11). The excitation light used was 810 nm. In this experiments, only the short pass filter SP485 nm was used for imaging in the forward path, meaning that endogenous SHG signal at 405 nm and also two photon fluorescence (TPF) could be detected. The longitudinal sections of the spinal cord in both cases have intense signal that comes from collagen in membrane layers that protect the spinal cord (Fig 11 a, b). The gray matter in the spinal cord is located at its center and in the SD rat it emits signal very likely due to TPF, this signal is not detected in case of *taiep* gray matter.

In the backward descanned detection path (LSM), the detection range can be freely adjusted between any values in the visible range. As mentioned before, adequate values for the detection of SHG signal are centered at 405 nm with a width of 20 nm. Signal of images from transversal sections of spinal cord that correspond to auto fluorescence (Fig. 3.11 c, d) are more intense at the center where gray matter is located. Micrographs obtained in the LSM between 395 and 405 nm suggests that only meningeal collagen generates SH signal (Fig. 3.11 e, f).

The cerebellum was also imaged in the transmission path. In this case the combined SH and TPF signals have a similar distribution for SD and *taiep* rats, high intensity from collagen and weaker signal from gray matter (Fig. 3.11 g, j). In all sections analyzed the boundaries between gray and white matter were clearly defined for control rats and blurred for *taiep* rats. In bright field micrographs we see that the control white matter is optically denser than white matter in *taiep* rat cerebellum (Fig. 3.11 h, i).

Laser power used for imaging these fixed tissue sections was 13 mW for spinal cord and 7.8 mW for cerebellum, in both cases focused with a 10X objective with a NA of 0.25.

Cells in culture

The first living system we imaged by SHG were HeLa cells in culture. SH signal from cells is generated in microtubules but we expected the signal from a single microtubules to be too low for being detected. Detectable SHG is usually obtained from bundles of parallel microtubules, that kind of microtubular organization is naturally found in mitotic spindles and in axons. Paraformaldehyde fixation leads to the disappearance of microtubule's SH signal [76,100], therefore only living cells were imaged.

We seeded HeLa cells in glass bottom culture dishes and when confluence of cells was ~70%, the culture medium was removed and warm PBS was used for imaging. The culture medium was removed because it contains a colored pH indicator that exhibits autofluorescence and could generate unwanted signal. HeLa cells grow attached to the substrate and during their division process they detach and adopt a spherical shape. For imaging, the cell dish was placed on the sample stage and a region with spherical cells was located through the oculars, then the lid of the culture dish was removed and PBS was extracted leaving a minimal amount of the liquid, just enough to cover the cells (Fig. 3.12 a). When using a 35 mm cell culture dish, whose plastic bottom thickness was 1 mm, the total volume of a well with 1 cm diameter is ~ 80 uL, the PBS volume added for imaging was 40 uL.

We observed SH signal from two microtubule structures, mitotic spindles (Fig. 3.12 b, d) and intercellular bridges (Fig. 3.12 c). Only the portion of the spindle fibers whose orientation coincides with the laser polarization (horizontal) emitted SH signal (Fig 3.12 b). Most of cells in the culture dish were attached to the substrate and their microtubules did not generate detectable SH signal.

In the spindle, microtubules of the central part are arranged in two antiparallel arrays with their plus ends at the equator and their minus ends at the poles with an overall shape of a football, and at each pole, the mitotic spindle has an aster, like a tuft of microtubules[119]. None of the four mitotic spindles shown in figure 3.12 has the same tridimensional orientation but in all of them the signal arises from MTs parallel to the laser orientation. In order to obtain images of both poles of the mitotic apparatus we had to obtain sequential images separated by half a micron, and the images presented here are the sum projection of 8-12 planes (Fig. 3.12 b, d). The power required for imaging was 4.5 mW using a 63X objective with NA 1.46

and the highest gray values obtained from bundles of MTs in the 8-bit images were around 30 (Fig. 3.12 f).
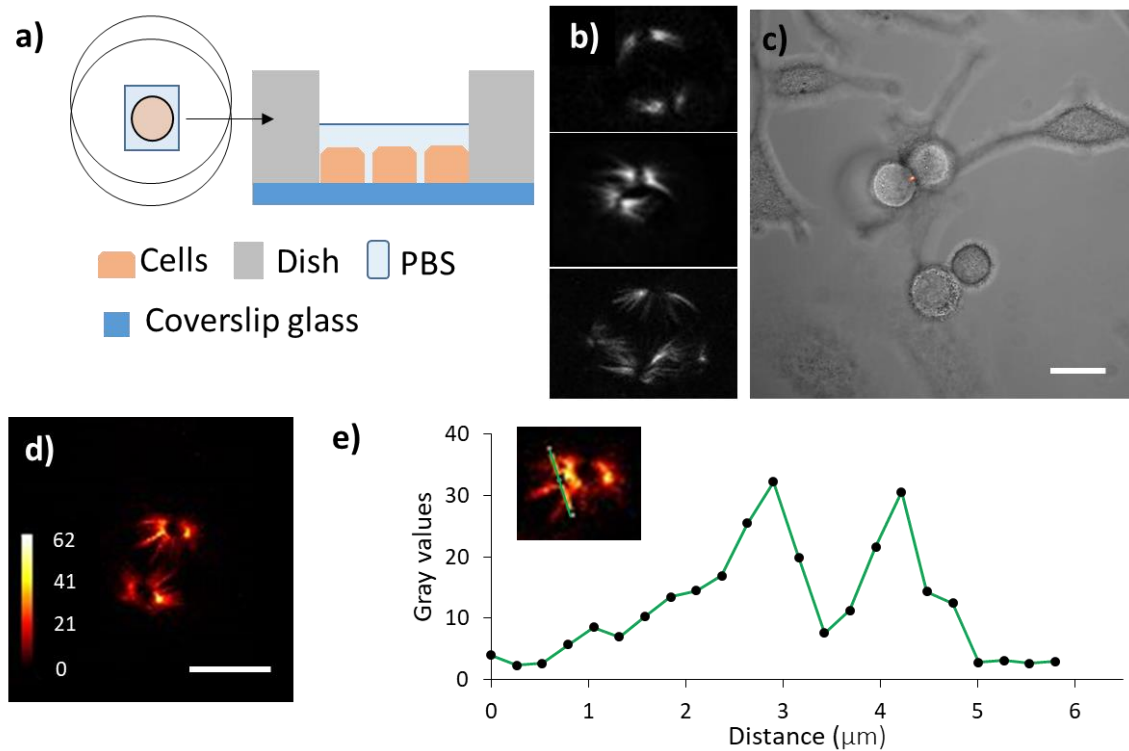

Figure 3.12 Mitotic spindle and intercellular bridge imaged by SHG. a) Sample preparation for SHG imaging, no lid and a thin layer of PBS are required for SHG imaging. b) Mitotic spindles imaged by SHG with a horizontally polarized laser. c) Merge of SHG image of an intercellular bridge and the bright field image. d) SHG micrograph of a HeLa cell in division where the MTs that are horizontally distributed are seen. e) Plot of gray values obtained from linescan through microtubules of mitotic spindle (green line inset). Scale bar in (c) 20 μm and in (e) 10 μm.

We also tested SHG microscopy in fate restricted Immortalized Multipotent Otic Progenitor (iMOP) cells, which are capable of differentiating into functional hair cells and neurons (Azadhe 2016). Undifferentiated iMOP cells grow in suspension. SHG signal from unlabeled, undifferentiated iMOPs was obtained from those portions of the mitotic spindles with bundles of MTs horizontally oriented (Fig. 3.13 a–c). After differentiation, neuron-like iMOP cells exhibit fiber like axons that generated SH (Fig. 3.13 d, f). To confirm that SH signal was generated from MTs we fixed and immunolabeled the cells for tubulin (Fig. 3.13 e). Fluorescence from labeled MTs and SHG coincide almost totally. The orientation of laser polarization is horizontal and axons that had their MTs in that orientation give rise to SHG.

The fluorescence signal does not depend on laser orientation and horizontally and vertically oriented MTs are equally excited and detected (Fig. 3.13 f).

The imaging conditions for iMOP cells were similar to those used for HeLa cells, but the objective used was a 25X NA 0.8, and the power was 15.96 mW for not differentiated cells (mitotic spindles) and 9.1 mW for differentiated cells (axons).
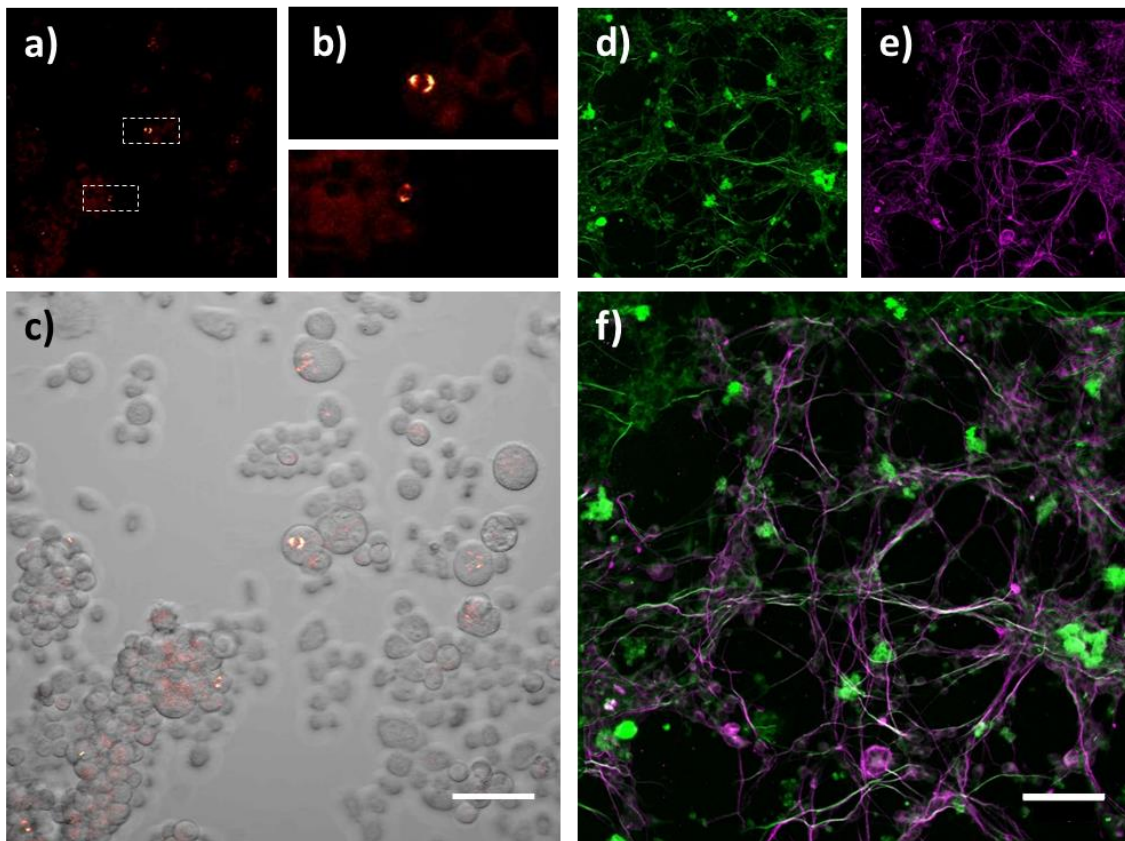

Figure 3.13 Immortalized Multipotent Otic Progenitor cells prior to and after differentiation. a) Micrograph from undifferentiated iMOP cells; only the mitotic spindles generate SH signals. b) Zoom on mitotic spindles framed in (a). c) Merge of bright field and SHG images, where the whole shape of the cells is visible. d) SHG micrograph from neuron like-cells, where axons are the major source of signal. e) Fluorescence from the same culture of cells fixed and immuno labeled for microtubules. f) Merge from SHG in green and fluorescence from microtubules in magenta. Both (e) and (f) are a sum projection from 7 planes separated by 2 μm. Scale bar in (c) is 50 μm and in (f) is 100 μm.

Acute tissue sections

Collagen and myosin

Collagens are the most abundant extracellular matrix macromolecules in vertebrates[120]. Most of collagens exist as triple helices formed by strong and flexible fibrils[121]. SHG arises from the non-centrosymmetric arrangement of chemical moieties of the polypeptide at a molecular

level, and at a supra molecular level it is irradiated from individual collagen fibrils of around 50 nm diameter[122]. Fibrillary collagen generates bright second harmonic signals, and its hyperpolarizability is just 10-fold less than crystalline quartz[84].

Acute mouse gastrocnemius tendon and a small section of the liver surface were dissected and whole mounted. A mouse tail was sliced in 150 µm longitudinal and transversal sections. A rat gastrocnemius muscle was sliced in 200 µm sections. The sections were mounted between a slide and a coverslip using PBS as mounting medium. Images from fibrillary collagen in tendon of mouse and rat exhibited high signal intensity (Fig. 3.14 a, b and c). The laser polarization mostly coincides with the orientation of collagen fibrils in fig 3.14 (a) and (b), but the signal from collagen in (b) is more intense because the excitation laser power was higher, 20.8 mW (<I> = 5.9 MW/cm^2) and 26 mW (<I> =7.5 MW/cm^2) respectively . To image the tendon in Fig 3.14 (c) the laser power was only 3.9 mW but the numerical aperture of the objective used was higher (0.8) and the calculated intensity was 2.4 MW/cm^2, still lower than the intensity used for imaging (a) and (b).

A different distribution of collagen fibers was observed in tail sections: most collagen fibrils are parallel to the tail in its longitudinal sections (Fig 3.14 d) while in transverse slices the collagen fibers are randomly oriented (Fig 3.14 e). Both images were obtained with the same average power.

Rat and mouse tail and gastrocnemius tendon are manly composed of type I collagen which is known to generate strong SHG emissions. In general, the minima and maxima of SHG intensity occur when laser is perpendicular and parallel to the collagen fiber direction, respectively[123–125],but in figure 3.14 collagen fibers orientation is almost perpendicular to the direction of polarization of the laser beam and the signal is still intense suggesting that the intensity may be associated to differences on fiber density between different regions rather than polarization dependence.

We used the 50X objective for imaging with an average power of 22.1 mW for tendon and 20.8 mW for liver capsule.
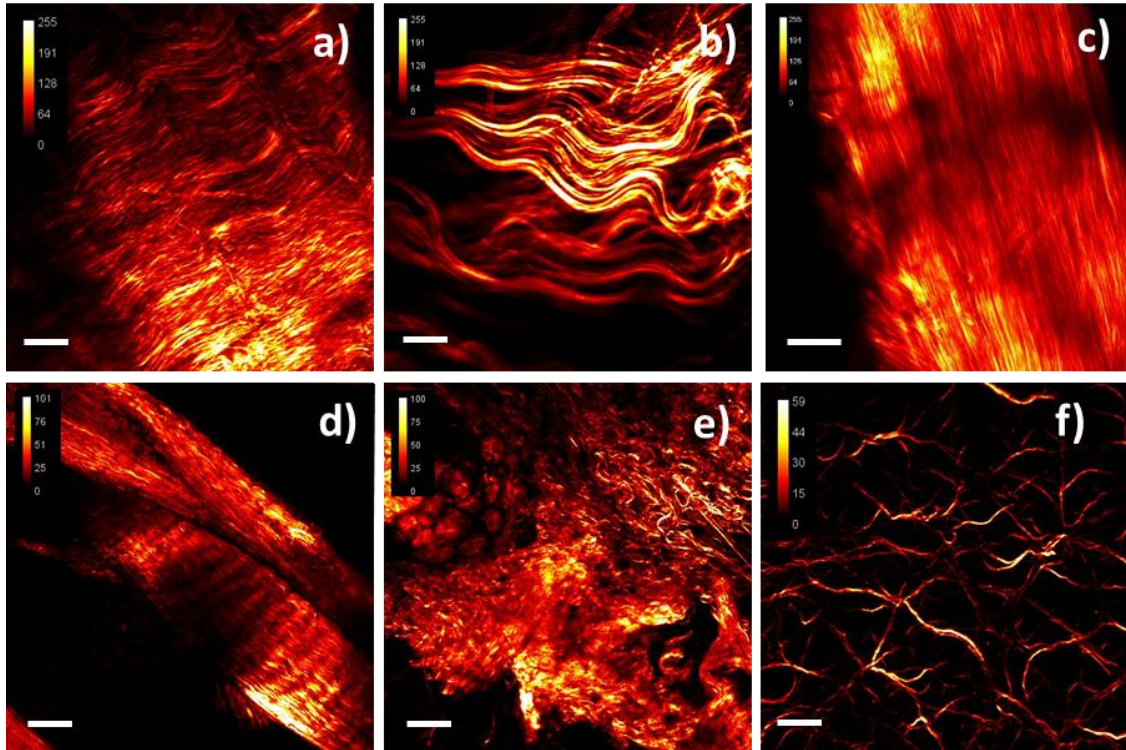
Figure 3.14 Collagen from acute tissue sections. a) Tendon of the gastrocnemius muscle of a mouse. b and c) Tendon from gastrocnemius mouse of rats. d) Longitudinal section of mouse tail. e) Transversal section of muse tail. f) Collagen in kidney surface of mouse. Scale bar (a), (b) and (d) 20 µm, (c) and (e) 50 µm and (f) 100 µm. All images obtained in the transmission path and the laser polarization was horizontal.

The sarcomere is the basic structural unit of skeletal muscle tissue and is a highly organized arrangement of contractile, regulatory, and structural proteins (Fig 3.15). The distance between z-disc defines the sarcomere and the shortening of individual sarcomeres leads to the contraction of individual skeletal muscle fibers. The Z-disc are pulled closer during muscle contraction and move apart during relaxation. During contraction thin actin filaments and thick myosin filaments generate cross-bridges, which slide the myofilaments over each other. During relaxation myosin and actin detach[126].

Myosin is a fibrous protein, whose filaments have a uniform longitude of 1.6 microns and a diameter of 30 nm[127]. Thick myofilaments are composed of myosin protein complexes, which are made up of six proteins: two myosin heavy chains and four light chain molecules. Hundreds of myosin proteins are arranged into each thick filament with tails toward the M-

line and heads extending toward the Z-discs. Myosin can convert the chemical energy of ATP into mechanical energy to generate force and movement[128].

SHG in cardiac myocytes originates from within the coiled rod region of myosin thick filaments[67,129] and has been used to track A-bands in subsarcomere structure in live cardiac myocyte[130].
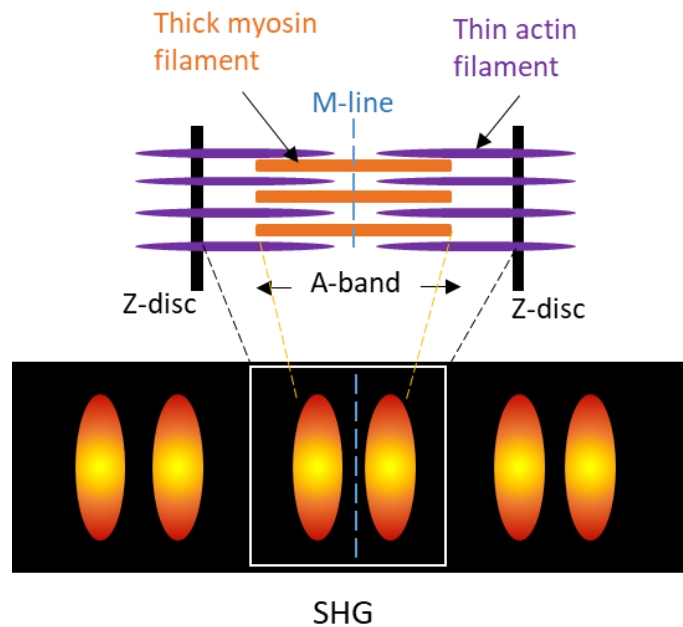

Figure 3.15 *Diagram of a sarcomere depicting the myosin filaments in the A-band as the source of SHG emitted signal*

The same gastrocnemius muscles used for collagen imaging were studied for the myosin contribution (mouse and rat). A section of mouse muscle was incubated for 2 minutes with Hoechst and then imaged, to reveal the position of nuclei (Fig 3.16 a, b, c). The TPE absorption of Hoechst overlaps with the wavelength used for nonlinear imaging (810 nm), and part of its emission is allowed by the short pass filter (485 nm) used for SHG imaging, in consequence Fig. 3.16 a, has contributions from SHG from myosin and TPF from Hoechst. We also obtained a fluorescence image from the nuclei (Fig. 3.16 b) and made the merge of bright field, nonlinear and fluorescence images (Fig 3.16 c).
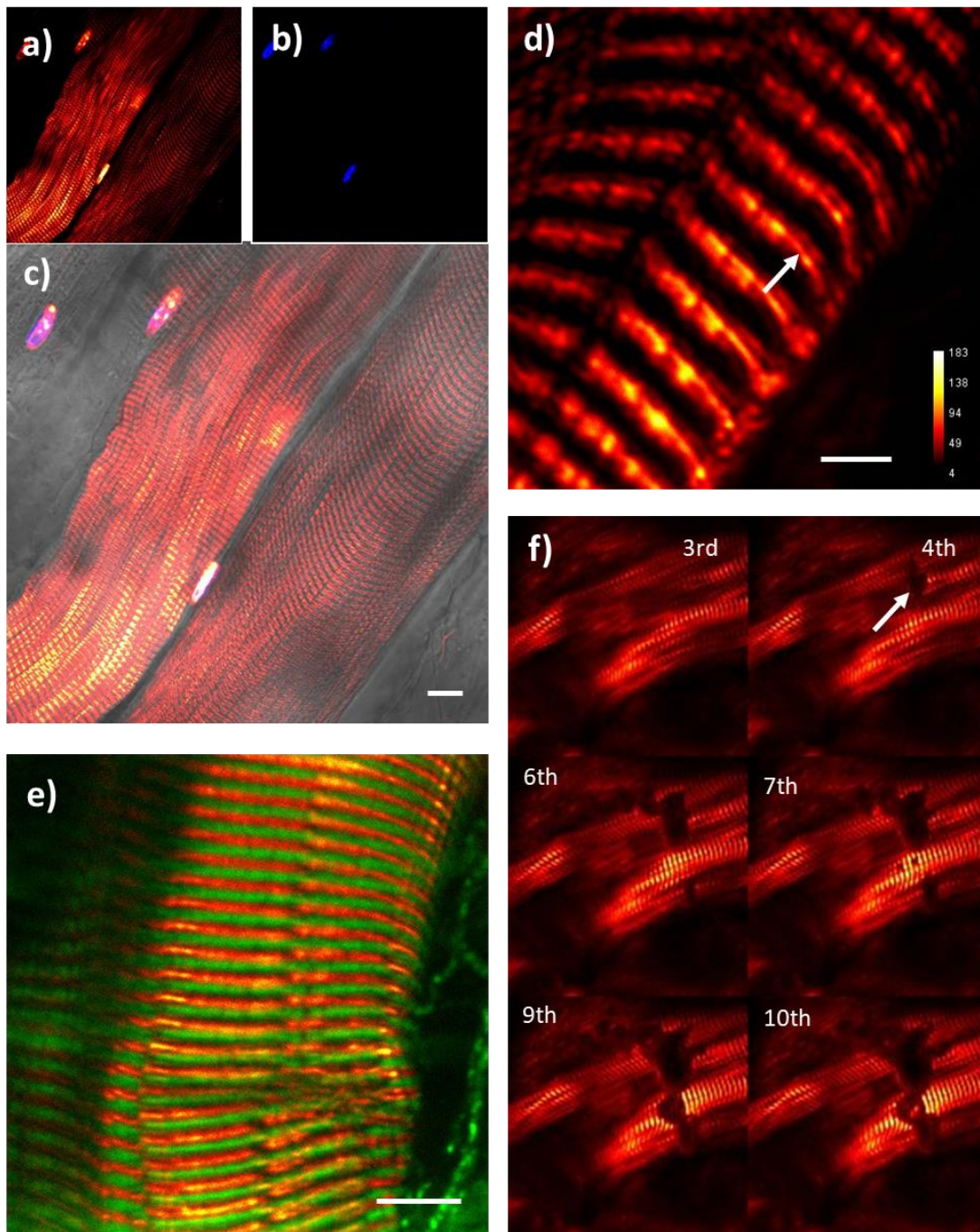
Figure 3.16 *Acute preparation of mouse gastrocnemius muscle imaged by SHG. a) SHG image from myosin and TPE fluorescence from nuclei labeled with Hoescht. b) Fluorescence image from nuclei in (a). c) Merge of the bright field, SHG and fluorescence images in (a and b). d) High magnification SHG micrograph where myosin from the A band of sarcomeres is resolved and appears like a double line (arrow). e) Merge of images obtained in forward (red hot look up table) and backward direction (green LUT). f) Damage in tissue (arrow). The tissue was consecutively imaged at different planes separated by 0.5 μm. Scale bar in (c and e) is 10 μm, in (d) 5 μm. The calibration bar in (d) indicates the gray values associated with the pseudocolor (LUT) used in that image.*

We also obtained images with higher resolution where the two lobes in the A-band of the sarcomere are resolvable (Fig 3.16 d). Although the forward detected signal (red) and the backward detected signal (green) were obtained from the same field of view, they did not exactly match (Fig 3.16 e). Simultaneous imaging in forward and backward direction was not possible, the images were obtained consecutively and without moving the sample.

The images in Figure 3.16 a-e were obtained using the 50X NA 0.55 objective and laser powers between 26 and 31 mW, which translates to intensities of 7.5 and 9 MW/cm^2; working with these intensities did not damage the samples. When using the 63X NA 1.43 objective combined with a laser power of 26 mW we observed that the muscle suffered damage (Figure 3.16 f). Although the laser power used was the same as in previous images, as the NA of the objective was higher, the calculated intensity for this experiment was five times the intensity used to acquire previous images (47.5 MW/cm^2), and additionally the same region was imaged at different depths separated by 0.5 um. Our hypothesis is that this must be photo damage of thermal origin, related to the absorption of infrared radiation.

Central nervous system

The first images of acute sections from CNS were obtained from mouse brain.

As microtubules are highly dynamic structures they also respond to changes in temperature and depolymerize. In order to avoid microtubules depolymerization it is necessary to transport and maintain the acute tissue sections in a warm solution. Others have used artificial cerebrospinal fluid to maintain the CNS acute sections. We obtained good results maintaining the tissue in warm (37°C) Hanks' balanced salt solution (HBSS), which contains glucose and sodium bicarbonate and is often used for short cell incubation outside the growth medium.
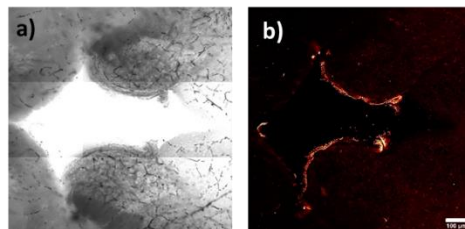

Figure 3.17 SHG from microtubules in other brain regions. a) Bright field image of the cerebral aqueduct of Sylvius. b) Same region as in (a) where the microtubules of the ependymal cells lining the cavity display high SHG. Scale bar 100 μm.

One of the advantages of the use of SHG is that infrared light penetrates deeper into tissue, which could allow the imaging of thicker tissue sections. We first tried imaging 300 um tissue sections from CNS, without good results. We were able to reduce the thickness of the mouse sections to be imaged, to 140 um. The best signal was obtained when imaging these coronal sections only over a coverslip and with the addition of 100 uL of HBSS on top. To avoid drying, the samples were washed in warm HBSS after imaging and then mounted again and imaged again. Tissues did not display damage signs for around 30 minutes after first imaging; after that time microtubules did not emit more signal.

High SHG signal intensity was obtained from the cilia of ependymal cells lining the wall of the cerebral aqueductus of Sylvius (Fig 3.17 a,b) The cilia are formed by a nine fold symmetric microtubule-based structure termed the basal body which must be the source of the intense signal. The SH signal from cilia has previously been reported by Dombeck et al[53].

Other authors had imaged axons of pyramidal cells and mossy fibers in the hippocampus by SHG microscopy[52,53]. Microtubules in axons are distributed parallel to each other and have uniform orientation, with their plus ends towards the axons tip[131] and have been stablished as the source of SHG from axons[53].
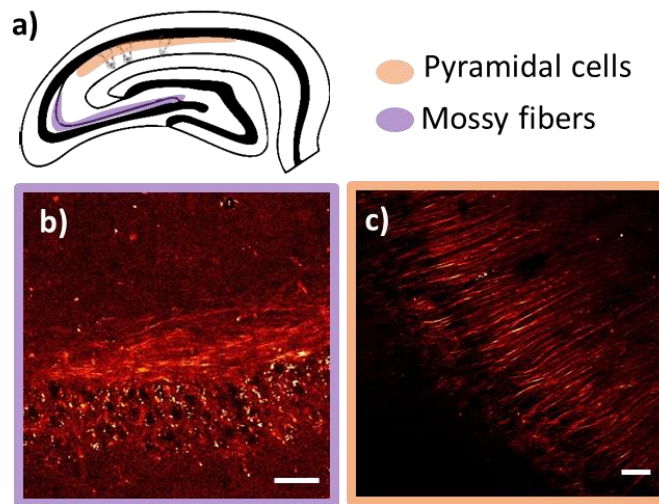

Figure 3.18 SHG from mouse hippocampus. a) Schematic representation of the location of neurons from the hippocampus from which we detected SHG signal. b) Mossy fibers in the mouse hippocampus. c) The hippocampus was rotated in order to have the pyramidal axons in the same orientation as the laser polarization. Scale bar in (b) and (d) is 50 um and in (c) is 30 um.

We also obtained images from axons in the hippocampus (Fig 3.19) of mouse brain. We first tried to obtain images with the 50X NA0.55 objective but we could not detect any signal besides the collagen. We decided to work with the 25X NA 0.8 objective because it would concentrate more intensity at the level of the sample increasing the chances of obtaining SH signal from microtubules. We used a power of 10.4 mW.

The orientation of the slice was important as the intensity of the emitted SHG will depend on the fiber orientation respect to laser polarization. We imaged axons from the mossy fibers (Fig 3.18 b) and also the axons from the pyramidal cells (Fig 3.18 a, b).

Imaging of taiep rat brain by SHG microscopy

We first imaged the corpus callosum (CC), and the cerebellar white matter, because both are mainly composed of myelinated axons and therefore more oligodendrocytes can be found there than in other regions. The *taiep* rat suffers from progressive demyelination and atrophy of the cerebellum[22,48,50]; however, the amount and distribution of oligodendrocytes in CC and cerebellar WM has not been assessed yet.

The images obtained from the CNS of control (wild type, WT) and TUBB4A mutant *taiep* rats showed different patterns of SHG emitting structures: their spatial distribution resembled elongated cellular processes, cell bodies and also some rounded structures, among the dominating presence of fiber-like structures (Fig. 3.19, c, h, e, k). In equivalent regions of control rats, the signal from the CC was always weaker, and no cell body-like distributions were seen (Fig. 3.19 b, g, d, j). In all the TUBB4A mutant rats examined, the SHG active structures in each folium were arranged inside cell bodies or processes and located in the cerebellar WM. The detected signals had a higher intensity than any signal obtained from homologous regions of control animals (Fig. 3.19,g to k). Same type of structures was found in adult *taiep* and control rats at 6 and 10 months.
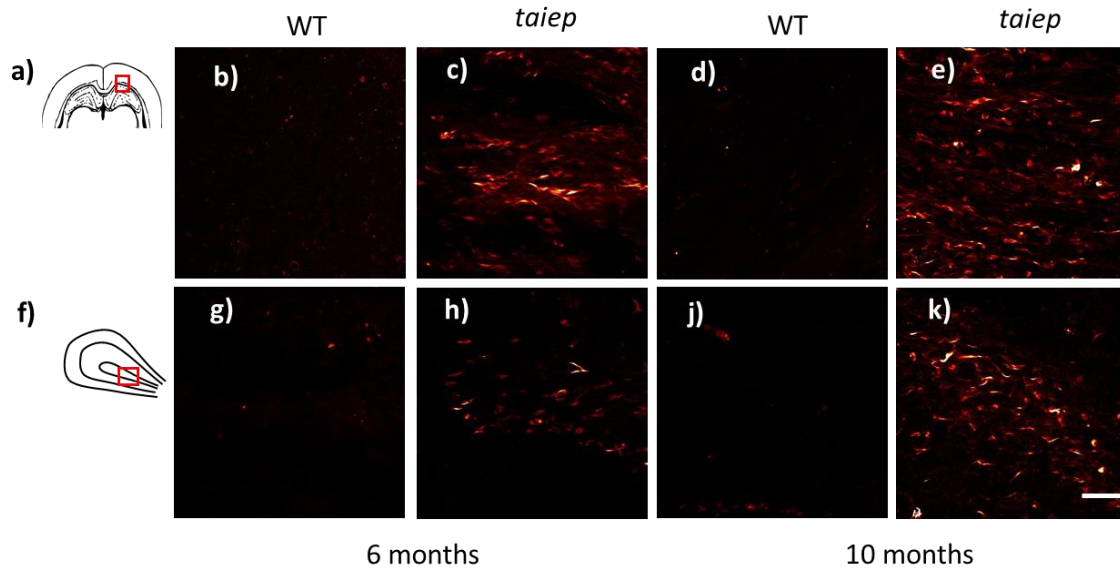
Figure 3.19 White matter of corpus callosum and cerebellum of taiep rats hosts cells that emit SH signal. a) Location of the imaged and analyzed region of the CC. b-e) Representative SHG micrographs from the CC of WT and a TUBB4A mutant rats of 6 months (taiep n=2, WT n=2) and 10 months (taiep n=4, WT n=2). f) Location of the imaged region of folium in the cerebellum. g-k) Representative SHG micrographs from the cerebellar white matter of WT and taiep rats of 6 months (taiep n=2, WT n=2) and 10 months (taiep n=4, WT n=2). Scale bar 50 μm.

To have a better comprehension of the tridimensional distribution of cells in the white matter, images composed of various tiles and planes in the z direction were acquired, stitched and projected to be presented in 2 dimensions (Figure 3.20). From those images we see that the corpus callosum of *taiep* rats has the higher intensity but at the same time has small regions with lower density, very likely due to loss of cell density in these parts (Fig 3.20 b). On the other hand, the corpus callosum of the WT rat is more homogeneous but the signal is lower. By analyzing 26 images from mutant and 16 from healthy rats, we obtained gray values from 26 ROI in the CC (260000 pixels) for each group of rats. The histogram built with the data depicts the difference in intensity of the images: gray values in WT are below 25 while in *taiep* the majority is below 50 and some pixels reach values up to 250 (Fig. 3.20 c).
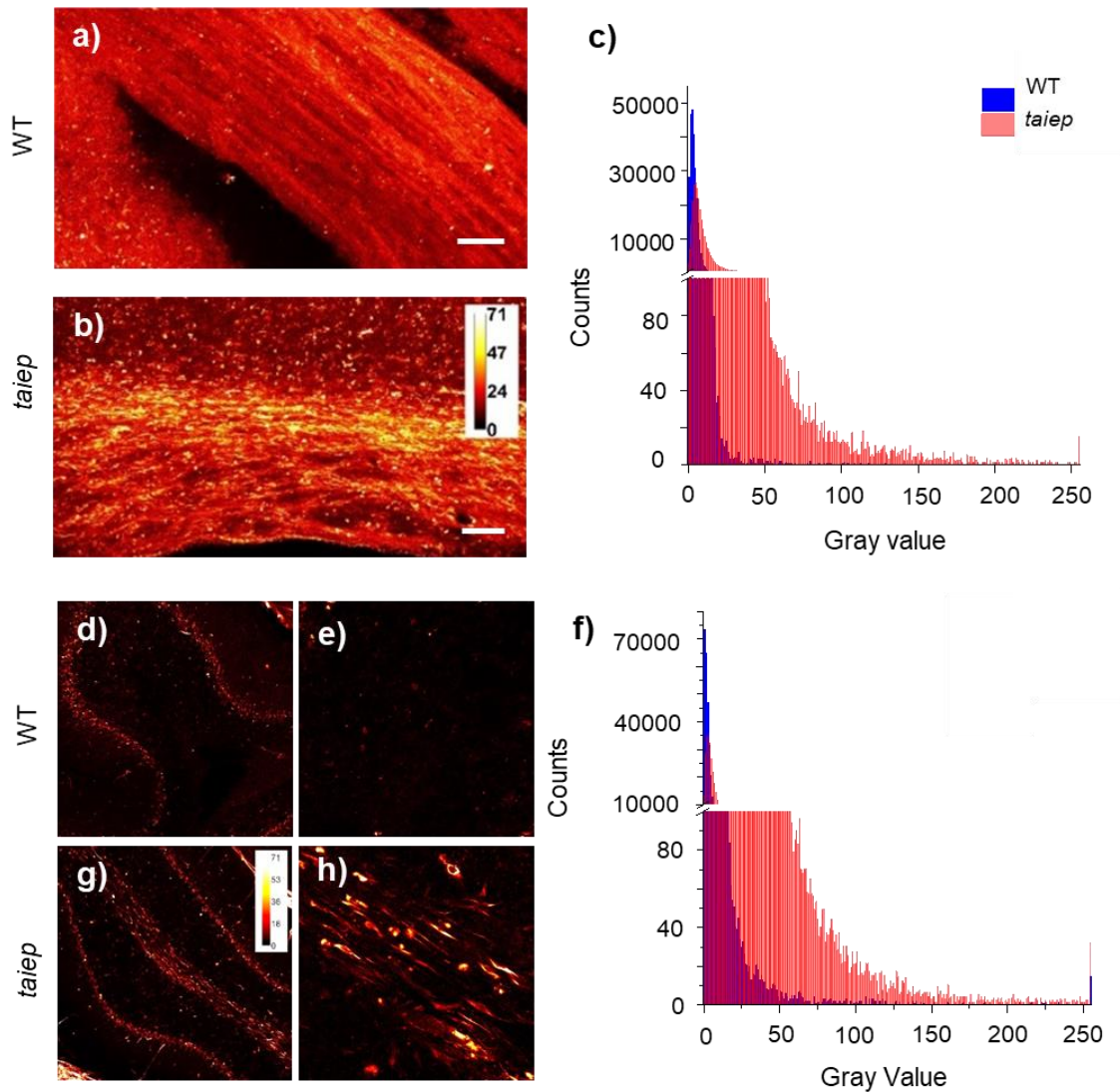
Figure 3.20 Higher SHG intensity is observed in the corpus callosum and cerebellar white matter. a, b) Representative SHG micrographs from the CC of a WT and a TUBB4A mutant rat, respectively. Z-stacks of five images, each spaced 7 μm, were generated. c) Gray level histogram obtained from regions of interest (ROIs) in the CC of the rats (26 + 16 images from 3 taiep and 2 WT rats). Representative SHG micrographs from cerebellum of WT (d,e) and mutant (f,g) rats. The images are max projections from 5 planes separated by 7 μm. h) Histogram obtained from SH signal of the cerebellar WM (2 WT and 3 taiep rats).

Images from the whole folia of rats at various depths were also acquired and their sum projections are displayed (Fig 3.20 d, f). The structures that emit SH signals are located in the white matter. A higher magnification of the WM reveals cell-shaped structures and their processes (Fig 3.20 g), whereas in the higher magnification images of white mater from WT rat no similar structures are found. By analyzing 16 images from mutant and 15 from WT rats, we obtained the gray values from 60 ROI in the cerebellar white matter, 30 ROI (300

000 pixels) for each group of rats. The histogram (Fig. 3.20 f) illustrates that most gray values of WT are below 25, while in *taiep* most of the gray values reach 50, with some pixels displaying values up to 250.

We found similar SH signal emitting structures in other tracts like the internal capsule, anterior commissure, and fibers crossing the caudate-putamen of TUBB4A rats (Fig 3.21).
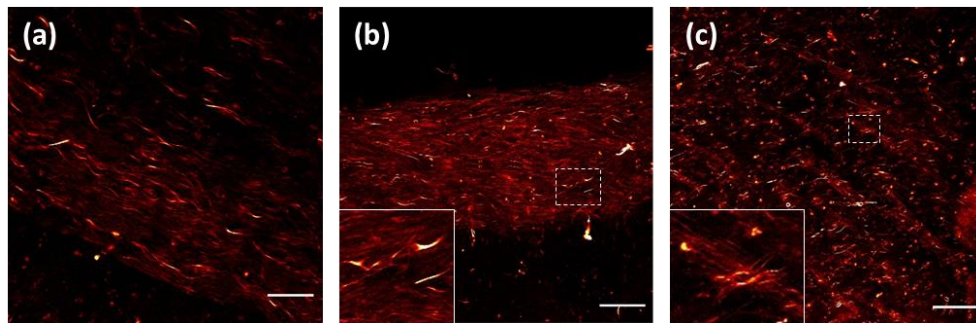
Figure 3. 21. SH signal emitting structures in other tracts of taiep rat's brain. Similar structures were observed in (a) the internal capsule, (b) the anterior commissure and (c) in the caudate-putamen of TUBB4A rats. Scale bars in (a) 50 μm and in (b, c) 100 μm.

Some images of CNS of rats were acquired in the forward path, as all previous CNS images shown, but also using an additional element, a narrow band pass filter centered al 405 nm and with a width of 20 nm (Fig 3.22). The sharp filter decreased the unspecific signal intensity improving the definition of the signal from the soma like and the elongated structures in the *taiep* images (Fig 3.22 f, h). Few thin fibers are still visible in the filtered corpus callosum image from WT rat (Fig 3.22 a, e), but in the WT cerebellum almost all signal is filtered out (Fig 33.22 c, g).

This filter was positioned between the condenser and the short pass filter, being this the best position among the few available in our set-up.

Before using the filter with the tissue from *taiep* rats we tested it with starch granules, the images obtained with and without the filter did not had significant changes in intensities (Fig 3.22 i, j).
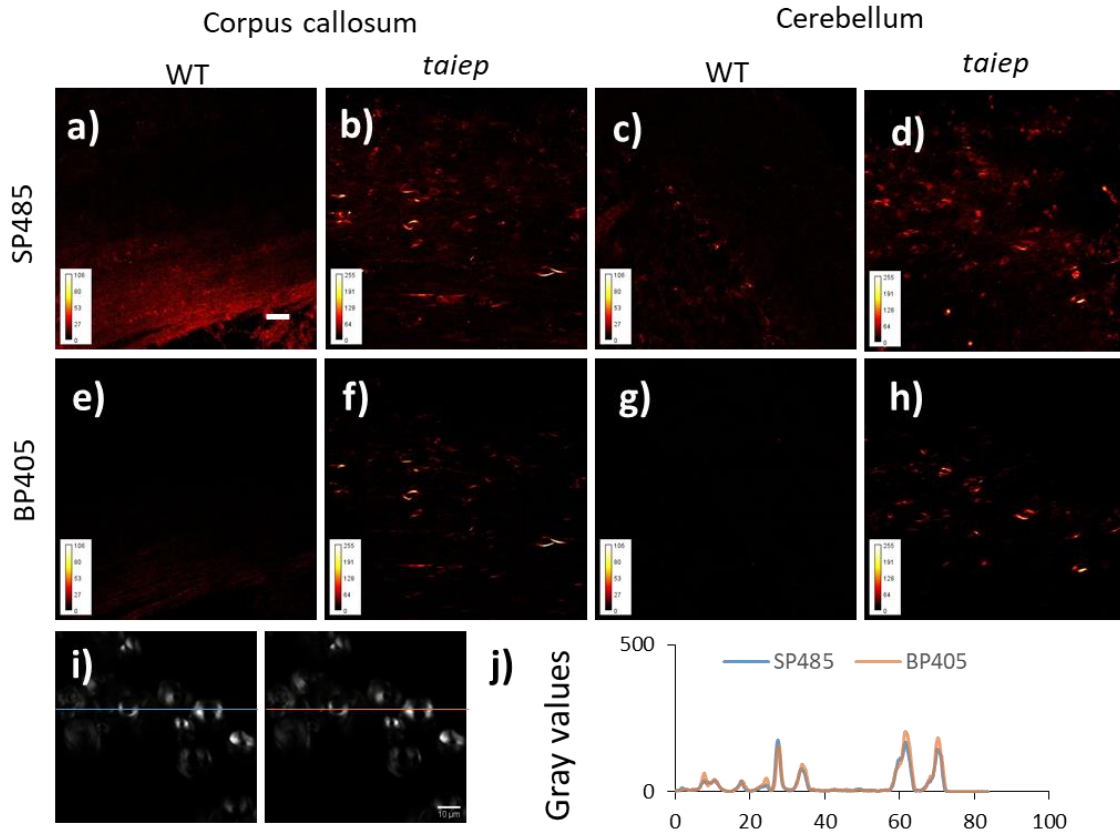
Figure 3.22 *Images acquired using SHG band pass filter maintain the differential signal. a-d) Images obtained using the short pass filter 485 nm. e-h) Images from the same regions as in (a-d) additionally filtered for precise SHG signal. i) Short pass SP485 filtered (left) and band pass 405 filtered (right) image from starch. j) Intensity plot from linescan in (i). Scale bar in (a) is valid for (a-h) and is 40 μm and scale bar for (i) is 10 μm.*

Discussion

In this chapter we introduced the nonlinear process of second harmonic generation (SHG) for its application in biomedical imaging. We described the characteristics of the optical set up used for SHG microscopy and the experiments performed in order to determine its possibilities and limitations. The lessons learned were applied for the imaging of tissular microtubules in close to living conditions with most cellular features preserved.

The first step was to determine the best conditions for the label free imaging of microtubules in cells of the central nervous system. We learned how to image

microtubules in our commercial setup by experimenting with a nonlinear crystal, starch, and fixed tissue sections to finally image microtubules from cells in culture.

A positive aspect about using a commercial set up is that most of its functions are automatized, but on the other hand, a negative aspect is the reduced adaptability of the optical system, for example for integration of polarization control. Our laser is horizontally polarized and as SHG is an intrinsically coherent process its polarization has an impact on the SHG image. In our experiments only the amylopectin chains and the microtubules that are parallel to laser polarization were efficiently excited and emitted SHG. In starch and mitotic cells it means that only a portion of the granule or the spindle apparatus will be visible by SHG. Polarization control would give us the flexibility to work with different polarization directions; the separate images that can be generated this way can be used to produce a SH image that includes the emission from emitters in various directions; even more, we could use the data obtained from different polarizations in the sample to obtain information about molecular orientation[106]. Imaging with circularly polarized light will generate images from emitters regardless of their orientations[53]. We tested two options available for changing laser polarization direction. We used either a half wave plate or a plastic polarizer before the laser reached the objective back aperture, but the mounting of the optic element was manual, reducing the possibility of a precise control. While imaging was possible, certain reduction in image intensity was observed, probably due to plastic strain or because the holder of the plate cut part of the laser beam.

The intensity obtained from SHG emitters encompasses structural information of the tissue. In order to make an appropriate analysis from the intensity we first need to understand that the image intensity depends on various factors. a) The intensity used for excitation: the higher the intensity the higher the SHG. b) On the numerical aperture of the objective: it is not the same to image with and the 50X NA 0.55 objective and a power of 26 mW or with the same power and the 63X objective; in the first situation the intensity is 7.5 MW/cm^2 but in the second situation the intensity is 36.6 MW/cm^2, almost 5 fives the intensity obtained with the lower NA objective. c) The detection path: usually the transmitted SHG is stronger that the backscattered SHG, but in some cases the backscattered signal could also be high due to the scattering nature of some samples. The non descanned paths detect more intensity because

the optical path is shorter compared to the descanned path. In the descanned path light must interact with more optical elements and finally less light is detected. d) The condenser: the height and the aperture of the iris diaphragm of the condenser must be checked before imaging because both could have a big impact in image intensity. In our microscope, when imaging in the forward direction the condenser collects the SHG and to improve the detection it needs to be tested for each objective because as numerical apertures are different the best height may not be the same for all objectives. It is common that users of the confocal microscope set the diaphragm aperture to less than half of its full diameter because it provides better contrast when it is closed, but for SHG it has to be fully opened. e) The organization of SHG emitters within the sample is also a factor that will have an effect on signal intensity[76,107]. As SHG is a coherent phenomenon the relative position between emitters will define if the signal emitted sums constructively or destructively. Also, the density of emitters in the imaging volume will have an effect on intensity of SHG. f) Sample mounting, that is the material above the sample will also impact signal intensity. We decided to avoid using coverslips on top of the samples and also to reduce to the minimum the amount of the liquid media used for tissue or cell preservation. g) The biological state of the harmonophore, we have seen that damaged microtubules from mitotic spindles and axons in culture would not emit more SHG.

No thermal damage is expected from SHG imaging but it is important to remember that other nonlinear and linear phenomena could be occurring at the same time, like two photon and one photon excitation. Three types of damage have been described when studying two photon excitation photo damage. First, photo damage as a consequence of TPE of intracellular chromophores, in this case photo oxidative processes result in the formation of reactive oxygen species which triggers a biochemical damage cascade in cells. Second, a dielectric breakdown occurs when high intensity optical fields ionize the molecules in the specimen. And third, damage due to single photon absorption, which is of thermal origin[132,133]. We experienced that imaging for extended time (z-stacks) could result in sample damage, even when the power used is below 100 mW. The cavitation (as seen in Figure 3.17 f) could be a result of an abrupt rise in temperature due to absorption of infrared radiation. We also observed that when imaging big regions for extended time (tiles) the sample could get dry and emitted unspecific signal increases rapidly (Fig 3.18 d). Therefore, for acute tissue

imaging the scanning time should be brief to avoid heating and damaging of tissue. On average, our 25X images were generated in 15 s as 512x512 pixels arrays, averaging 2 times.

As for the objectives used, we could not obtain SH from microtubules when using the 50X NA 0.55 objective, even though it was good enough for starch, collagen and myosin imaging. All SHG images from microtubules were obtained either with the 25X NA 0.8 or 63X NA 1.43 objectives. For tissue imaging the 25X was preferred because small increases in laser power using the 63X objective rapidly damaged the tissue.

Our optical set up definitely allows SHG imaging of microtubules, even though finding the equilibrium between innocuous incident laser power, ideal volume of medium and detectable SHG can be challenging.

Our second goal was to explore the potential of SHG to highlight the changes in the tubulin network caused by a TUBB4A mutation in H-ABC. We aimed to image the consequences of the mutation on fresh, unlabeled nervous tissue, and make a direct comparison between the *taiep* murine model of tubulinopathy and the WT counterpart. We found that the images obtained consistently showed remarkable differences between healthy and mutant nervous tissue.

The molecular hallmark of the *taiep* rat is the accumulation of microtubules within its oligodendrocytes, in the cell body and in its processes[46]. Recent work indicates that detectable SH signal from microtubules depends not only on the uniform polarization[53] but also on the number and stability of the microtubules in a bundle[76]. SHG microscopy is therefore sensitive to subtle changes in the organization of the microtubules network. So far there are no publications where SHG from microtubules in oligodendrocytes is studied. We hypothesized that bundles of microtubules in the myelinating cells of the TUBB4A mutant rats would give rise to detectable SHG.

SHG revealed that in the WM of the H-ABC animal model elongated structures and cell bodies emitted SH signal and that similar structures were not found in WM of control rats. These structures were detected in the corpus callosum and in the cerebellar white matter of mutant rats. Since, a) microtubules and collagen are the only SH emitters in the CNS[72], b) many tubulin mutations cause microtubule increased stability[134], c) the emitting structures

we detected in *taiep* are located mainly in the WM, and d) the processes imaged by SHG correspond to cell bodies in the WM containing a high amount of tubulin, the somata-like structures are plausibly oligodendrocytes bodies, while the fibrous structures might be oligodendrocyte processes, abnormally filled with microtubules.

When we analyzed the images of corpus callosum from WT rats we also observed that weak signal arises from thin processes in the corpus callosum, this signal persisted after filtering with the band pass filter for SHG, meaning that this was SH signal very likely from axons. When we previously imaged mouse hippocampus we could detect signal from unmyelinated axons of the pyramidal cells and from the mossy fibers; those fibers appeared more defined than the axons in the corpus callosum. A possible explanation is that tight myelin sheaths surrounding axons could interfere with excitation and/or SHG emission from the amount of microtubules present inside axons and covered by several layers of a birefringent material[52]. Specific experiments and simulations that replicate the geometry of microtubules inside myelinated axons are needed to thoroughly prove this hypothesis.

Myelination in the central and peripheral nervous system has been assessed with other multiphoton microscopy techniques like third harmonic generation (THG) or Coherent Anti-Stokes Raman Scattering (CARS)[135–140]. Compared to these techniques SHG has its own advantages for the visualization of the CNS. THG arises from interfaces instead SHG is molecule-specific, and its coherent nature make it sensitive to subtle changes in the microtubule network[76]. Regarding its implementation, many neuroscience labs have access to a two-photon excitation system, that can be easily modified into a SHG set-up[70], therefore is more accessible than THG or CARS microscopy which require completely different laser sources[140–142], besides detection adaptations. Another important advantage is that the laser power typically used for SHG is not expected to produce thermal injury due to SHG (although a certain amount of damage is unavoidable because of single and two photon absorption) and it is therefore compatible with prolonged imaging of living cells[67,68,53,143,144,102,145,76].

Endogenous emissions from Nicotinamide adenine dinucleotide phosphate (NAD(P)H), flavin adenine dinucleotide (FAD), retinol, elastin, collagen in the CNS, could also be induced with highly energetic short pulses of light[70]. In our study of the CNS we detected the

intrinsic signal from collagen for example in fresh and fixed sections from the meninges and in fresh choroid plexus (data not shown). The SHG signal from microtubules was imaged in acute sections of CC and cerebellum, together with the signature pathological signal coming from the white matter tracts in brain and cerebellum of the TUBB4A mutant rats. In the neurodegeneration processes studied so far, the detectable amount of NAD(P)H, FAD and retinol decreases after the onset and with the progression of the disease[146], which makes very unlikely that the differential signal in WM of the *taiep* rat corresponds to these molecules.

A region of the cerebellum where we detected comparable nonlinear signal in both control and mutant rats was the Purkinje cell layer. This signal has been attributed to TPE from NAD(P)H and FAD in the cytoplasm of Purkinje cells[72]. We cannot exclude a contamination of TPE signal in the nonlinear images obtained using only the short pass filter 485nm. However, images acquired after the narrow band pass filter (BP405) confirm that the differential signal found in *taiep* rats white matter is SHG.

Further studies on different regions of the CNS of the TUBB4A mutant rat and at different ages will contribute to the understanding of the relation between the number of cell bodies detected by SHG and the demyelination state.
Finally, this study of a tubulinopathy model using SHG microscopy is the first to expand the applications of the technique for studying neurodegenerative disorders besides those where disruption of axonal MTs has been implicated, like Alzheimer´s disease and glaucoma, to diseases where a mutation alters MTs organization and number in possibly more than one cell type.

Fluorescence microscopy

Fluorescence microscopy is a powerful technique that takes advantage of molecules that can absorb light of a particular range of wavelengths and the re-emit light at longer wavelengths. It combines the magnifying properties of light microscopy with the visualization of fluorescent molecules. Wide field fluorescence microscopy and confocal microscopy are both techniques used to observe fluorescent samples. On wide field fluorescence microscopy the whole field of view is illuminated. The fluorescent sample is excited causing all the specimen thickness to fluoresce. The out of focus light cannot be separated from the in focus detail, reducing image contrast. In confocal microscopy a laser light source is focused in the sample, reducing the illuminated volume. All the illuminated volume is excited and the emitted light is collected by an objective and passes through a pinhole positioned confocal to the focal spot. The consequence of this restricted light path is that only light coming from the thin focal section contributes to the image. This technique allows to take images of different focal planes which can be recombined to create a three-dimensional representation of the sample.

Among the advantages provided by confocal laser scanning microscopy, are the possibility of using it with multiple dyes in the sample, the possibility to achieve high resolution without any post processing, 3D reconstruction and acceptable compatibility with live cell imaging.

We used fluorescence microscopy to analyze CNS tissue of the animal model for H-ABC and compared it to tissues from the CNS of control rats.

Staining of samples

Cells size and transparency, make them invisible, even when observed through a microscope. In a tissue section, the task is even more difficult. Contrast should be created in the system to distinguish the cells' features. This contrast can be generated by introducing dyes into cells.

Chemistry contributed with the development of different dyes and fluorescent molecules used to label cell structures. Fluorescent dyes are fluorescent molecules that don't associate with a particular biological target, and fluorescent probes are dyes capable of detecting

specific biological targets like cells in a tissue, organelles, proteins, nucleic acids, ions and enzymes[147].

The methods for delivering fluorescent compounds to specific locations in the cells can be divided into three groups: fluorescent proteins, fluorescently labeled antibodies and chemical dyes with an affinity for particular subcellular component.

Usually more than just one structure is observed, using in the same sample more than one of the methods listed above, increasing the information that can be obtained from the sample; when this is done it is important to make sure that the optical properties of the labels do not overlap[148].

Chemical dyes

One of the most widely used dyes is fluorescein mostly because it is excited by the 488 nm argon-ion laser line. And for multiple color labeling applications coumarins were the choice for blue ~450 nm, and rhodamines for orange ~580 nm. However these dyes showed limitations: fluorescein is pH sensitive, rhodamine aggregates in aqueous solutions and coumarines are comparably less efficient than fluorescein[149].

New dyes for biomolecular detection applications are always been developed to overcome this type of limitations. In this work the secondary antibodies were conjugated to dyes of the family of the Alexa Fluor fluorophores, which are more water soluble than fluorescein and rodhamine and exhibit a pH insensitivity over a very broad range $(4 - 10)$[150].

Fluorescent proteins

The story of Fluorescent Proteins began with the isolation of green fluorescent protein from Aequorea victoria jellyfish by Shimomura (1962). Later this protein has been extensively studied and modified giving birth to a vast number of useful blue, cyan and yellow mutants. Fluorescent proteins from other species have been identified giving more variety to the color palette including orange, red and far red. Fluorescent proteins need to be expressed by the cell so they are used in living cells.

Antibodies

In 1941 Coon and collaborators first used fluorescent antibodies to localize proteins using the high specificity of immune reactions of the animals[151].

An antibody is a Y- shaped globular protein that reacts specifically with the antigen that induced its formation and is produced mainly by plasma cells. Biotechnology has allowed the production of fluorescent markers by attaching fluorophores to antibodies. The technique used to label a specific protein or antigen in cells by the use of an antibody, is called immunocitochemistry.

Inmunocitochemistry is commonly accomplished either by using fluorophore-conjugated primary antibodies raised against a specific protein called direct immunofluorescence, or by first labeling with primary antibodies followed by secondary antibody detection that is, indirect inmunofluorescence.

Antibodies are produced using an animal species as the host. The most common species for primary antibody are rat, mouse, goat and rabbit, and for secondary goat, donkey, sheep and rabbit.

In this work we also used another method for the labeling of tubulin in live cells, SiR-tubulin[152]. The SiR fluorophores are based on silicon-containing rhodamine conjugated to ligands, in case of SiR-tubulin, SiR is conjugated to a microtubule binding drug, docetaxel.

Materials and methods

Tissue preparation

From the six *taiep* and four Sprague Dawley (SD) rats initially imaged by MRI, one *taiep* and one SD were perfused and used only for immunohistochemistry (IHC) experiments, while four *taiep* and two SD 10 months old rats were used for SHG and IHC experiments. Rats were anesthetized with a mixture of ketamine–xylazine (0.125 mg/Kg and 5 mg/Kg, IP), and then sacrificed by decapitation. The brain and cerebellum were removed and the two hemispheres separated. One was used for SHG imaging, and the second hemisphere was immediately immersed in 4% formaldehyde in PBS for immunohistochemical processing. Another group of four *taiep* and four WT aged 9 months was perfused with 4% PFA in PBS for additional IHC and therefore, not used for SHG imaging.

Fixed tissue sections were immersed in 30% sucrose in PBS at 4°C for 24 hours and frozen using tissue freezing medium (ref. 14020108926, Leica, USA). Thirty-micron slices were obtained in a CM 1860 cryostat (Leica, USA).

Sections were marked immunolabeled. Primary antibodies used: anti-neurofilaments 200 (N4142, Sigma, USA), anti-APC antibody [CC-1] (ab16794, abcam, UK) for mature oligodendrocytes, polyclonal anti- Alpha/Beta-tubulin (ATN02, Cytokeleton, USA). Secondary antibodies used: Alexa Fluor 555 A21422, Alexa Fluor 488 A11070 and Alexa Fluor 488 A11015 secondary antibodies (Thermo Fisher Scientific, USA). Myelin sheaths were stained with Fluoromyelin red (F34652, Thermo Fisher Scientific, USA) as indicated in the datasheet. Nuclei were stained with DAPI (62248, Thermo Fisher Scientific, USA). Acute tissue sections were incubated at 37°C in SiR-tubulin (Spirochrome AG CY-SC002, 1:100 mL in HBSS) for one hour prior to imaging.

Microscopy

For fluorescence imaging, we used a LSM-710-NLO confocal microscope (Zeiss, Germany) equipped with either an LCI Plan-Neofluar 25X/0.8 or an alpha Plan-Apochromat 63x/1.46 Oil Korr M27 immersion objectives.

Pseudo-bright field images were generated with residual 405 nm laser light captured in transmission by an external non descanned detector (NDD) of the LSM 710 Zeiss confocal microscope, using a 25x oil-immersion objective. Bright-field images of whole organs were acquired with a Cytation 5 cell imaging multi-mode reader (Biotek, Vermont, U.S.A.) with a 4x objective.

Analysis and statistics

The open source FIJI software[109] was used to convert and reconstruct the images as well as to perform the intensity analysis. The plugin StarDist [153] was used to count the nuclei. Graphpad Prism was used for statistical analysis: $p < 0.05$ (*), $p < 0.01$ (**), $p < 0.001$ (***), $p < 0.0001$ (****). The box graphs indicate median values with 25 and 75 percentile, the symbol "+" stands for the mean and whiskers represent min and max values. Bars graphs indicate mean value with S.E.M. Normal distribution of the data was assessed by Shapiro–Wilk normality tests, t-tests were conducted as a two sided.

Results

Demyelination of the corpus callosum and the cerebellum

We used the same brains of rats analyzed by MRI and SHG to perform the histological analysis of the structures of interest, including the cerebellum in *taiep* and WT rats of the same age (10 months).

Our MRI volumetric analysis of the corpus callosum support that it is atrophic, the most probable explanation for the atrophy is the demyelination. To corroborate this hypothesis, we analyzed the fixed tissue sections (Fig 4.1). In phase-contrast micrographs, the white matter of corpus callosum of WT rats was optically denser than in *taiep* rats (Fig. 4.1 a, f). We labeled neurofilaments with antibodies and myelin sheets with a membrane dye. A dimmer fluorescent myelin staining in *taiep* rats confirmed the damage in the white matter (Fig. 4.1 b, c , g, h). Additionally, we observed that the same demyelination affected the striosomes of *taiep* rats (Fig 4.1 d, i).
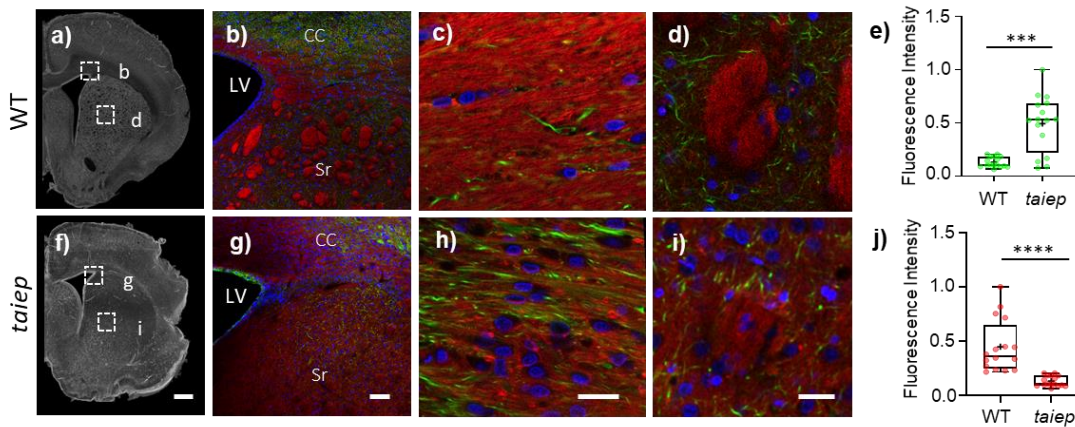

Figure 4.1 *The corpus callosum of 10 months old taiep rats is demyelinated. a, f) Representative coronal slices of corpus callosum and striatum of WT (a) and taiep rat (f) brains acquired by phase contrast microscopy. b, g) Myelin (red) and neurofilaments (green) were revealed by immunofluorescence. Amplifications of white squares for merge are shown in (c, h) the corpus callosum and in (d, i) the striatum. Nuclei were revealed by DAPI (blue). Scale bars 1000 μm (a, f), 20 μm (b,g), 5 μm (c,h), and 100 μm (d, i).LV: lateral ventricle, CC: corpus callosum, Sr: striatum. The membrane-associated signal is more intense and organized in control rats than in the mutants and the signal from neurofilaments is less intense in control rats. e) and j) Normalized fluorescence of neurofilaments and myelin (4 WT and 4 taiep rats, *** p <0.001 and **** p <0.0001, two tailed Mann-Whitney test). Fluorescence was normalized to the highest value, which for neurofilaments was measured in the TUBB4A and for myelin in the WT rat.*

The fluorescence intensity from neurofilaments in white matter tracts was always lower in healthy rats compared to the demyelinated model (Fig. 4.1 h). When comparing the images, the neurofilaments bundles in myelinated axons appeared somehow thinner and less intense

than bundles in *taiep* rats (Fig. 3 c, h). These differences were congruent with the observations obtained with the SHG technique, as a higher signal intensity was found in the white matter of *taiep* rats. The box charts were obtained from 4 WT and 4 TUBB4A mutant, 10 months old rats; 2 images from each rat and 2 ROIs in each image of the CC were analyzed (Fig. 4.1 e, j).

The hypomyelination and the atrophy of the cerebellum are pathognomonic signs of H-ABC. Together with the profound motor impairment they cause, they are also present in the animal model. The cerebellar white matter is a region where we found cells that generated SH signals. To investigate if there was a correspondence between spatial distribution of SHG and neural fibers in cerebellar layers, we assessed the fixed tissue sections by immunofluorescence.

In bright field micrographs, the white matter of WT rats has a higher optical density than the granular layer (Fig. 4.2 a). On the other hand, the white matter of *taiep* rats looks less dense. The fluorescent myelin staining is abundant and compact in WT rats while it is sparse in *taiep* rats (Fig. 4.2 b, g). Furthermore, neurofilaments immunofluorescence reveals the demyelinated axons. We compared the neurofilament fluorescence intensity of the cerebellar layers (Fig 4.2 c-e, h-j). In control rats the molecular layer displayed the highest fluorescence intensity (Fig. 4 p). Instead, in the case of *taiep* rats, the fluorescence intensity from fibers in the WM was significantly stronger than fluorescence in the granular and molecular layers (Fig. 4 q). Comparing between WT and *taiep* cerebellar layers, neurofilaments fluorescence intensities from the molecular and granular layers and the cerebellar WM of *taiep* rats were stronger than those of the same regions of control rats (Fig. 4.2 r, s and t).

Signal intensity in SHG micrographs obtained from homologous regions of the cerebellum of the same rats, reproduced the pattern observed in fluorescence images, i.e. dramatic difference in intensity in *taiep* white matter, being the signal from the mutant stronger than that from the WT (Fig. 4 a, d). These histology findings are also consistent with the hyperintensities observed in cerebellar MRIs of *taiep* rats and confirm the damage in the myelin of the cerebellar white matter.
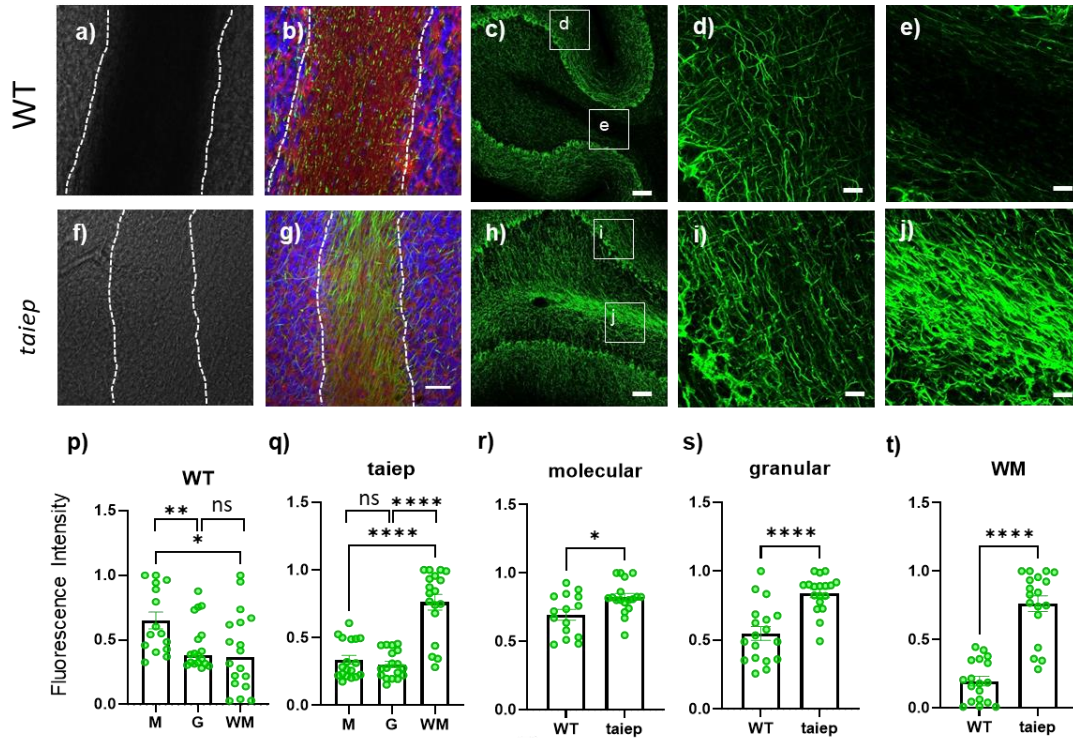
Figure 4.2 *Histological analysis of cerebellum. a,f) Bright field micrographs of coronal slices of cerebellum of WT and taiep rat brains (10 months). White dotted lines delimitate the white matter region in cerebellar folia. b, g) Myelin (red) and Neurofilament (green) were revealed by immunofluorescence. Nuclei were revealed by DAPI (blue). Scale bar in (g) 30 μm. Confocal images of stained neurofilaments from the cerebellum of WT (c-e) and mutant rats (h-k). (d and i) are zoomed regions in the molecular layer and (e and j) are zoomed regions in the cerebellar white matter, where the difference in signal distribution and intensity is better appreciated. p) In the control rats fluorescence from the molecular layer was significantly higher than fluorescence from WM and granular layer (n=3 WT rats ** $p <0.01$, * $p < 0.05$, two tailed Mann-Whitney test). q) In the mutant rat the WM fluorescence was higher than the fluorescence from granular and molecular layers (n = 3 TUBB4A rats, **** $p <0.0001$, two tailed Mann-Whitney test).Fluorescence intensity in the molecular (r) and granular (s) layers and WM (t) of mutant rats was significantly higher than the fluorescence from control rats (n=3 taiep and 3 WT rats, molecular layer * $p<0.05$, WM and granular layer **** $p<0.0001$, two tailed Mann-Whitney test).*

Mature oligodendrocytes in white matter

Song et al. imaged oligodendrocytes of *taiep* rats by transmission electron microscopy finding an unusually high amount of microtubules in the soma and in their processes (Song 1999). We immunolabeled the tissues for tubulins and for a mature oligodendrocyte marker in the search for the abnormal oligodendrocytes. In this analysis we used the tissue from 9

months old rats. The tubulin staining was ubiquitous due to the nature of the antibody used, a polyclonal immunoglobulin against alpha/beta tubulin, but in *taiep* rats we recognized cell bodies strongly stained for tubulin in the corpus callosum and in the cerebellar WM (Fig. 4.3 d, f, h and j arrows). The shape of the structures that were strongly stained for tubulin in *taiep* rat WM sections, closely resembled the cell bodies and rounded structures observed by SHG in the same regions of corpus callosum and cerebella of *taiep* rats. Some of the tubulin positive cell bodies were also positive for the oligodendrocyte marker (Fig. 4.3 h and j).

We counted more tubulin positive cells in the mutant animal (Fig 4.3 l) and also a higher number of cells in the CC and cerebellar WM of *taiep* rats (Fig 4.3 k). The difference in the amount of tubulin positive cells was more pronounced in the cerebellum, where we also found a higher number of mature oligodendrocytes. In the corpus callosum the difference in density of mature oligodendrocytes was not significant between WT and *taiep* rats.
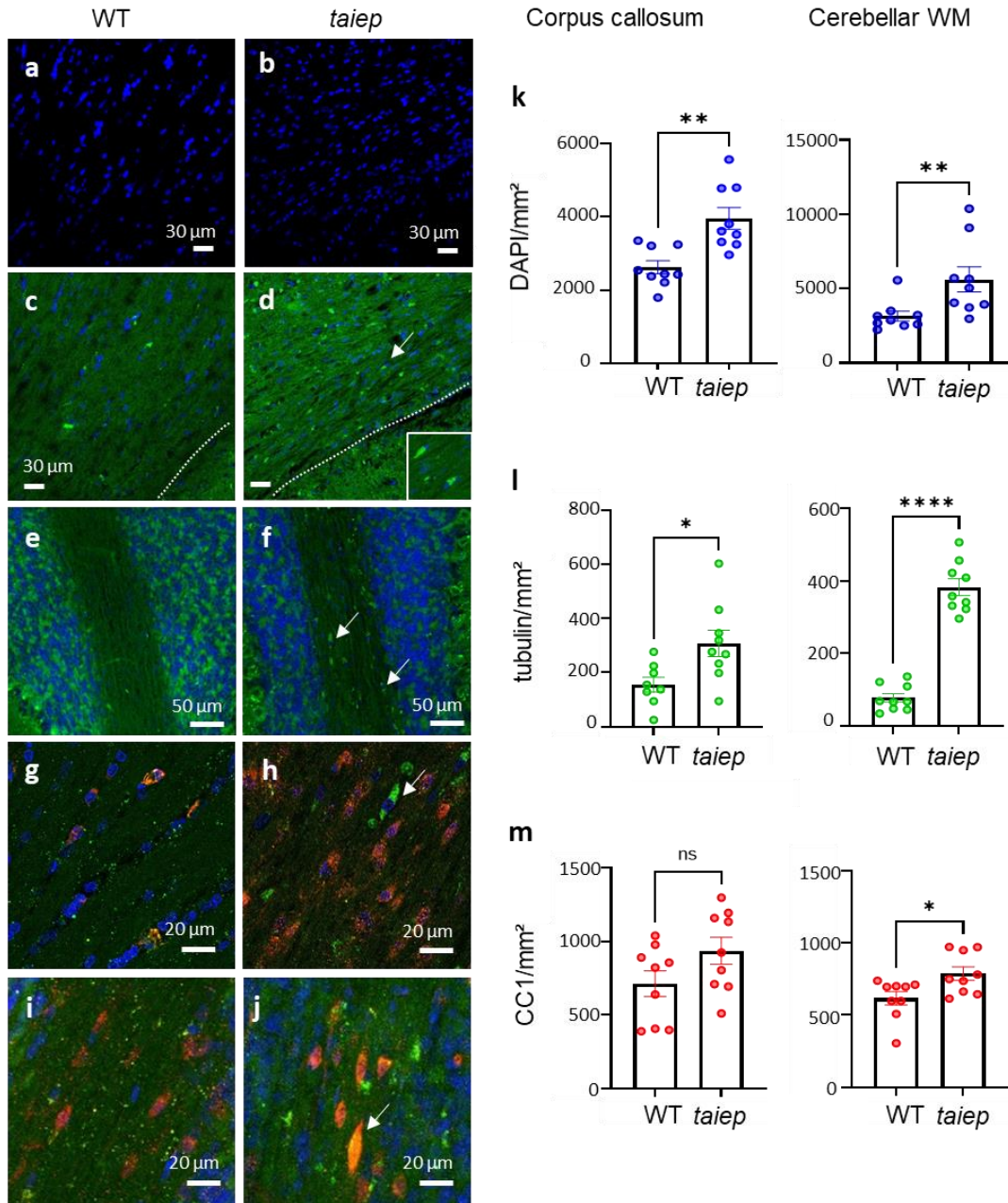
Figure 4.3 *Differences in cellular numbers between taiep and WT a-b) More nuclei are observed in the corpus callosum of taiep rats than in WT, respectively. c-d) Tubulin staining in corpus callosum of WT (c) and taiep rats (d); inset in d shows a magnification of the region pointed by the arrow. e-f) Cerebellar WM and granular layer in WT (e) and taiep rats (f), arrows in f point at cell bodies heavily stained for tubulin. g-j) Sections labeled with the mature oligodendrocyte marker CC1 in red, and tubulin in green; corpus callosum of WT (g) and taiep rats (h), cerebellar WM of WT (i) and taiep rats (j). Arrow in (h) points to a cell positive for tubulin and arrow in j points to a cell positive for tubulin and CC1. K) Quantification of DAPI (+) cells/mm² (** p < 0.01, Welch´s test for CC and ** p < 0.01, Mann Whitney test for cerebellum). l) Tubulin positive cells/mm² (* p < 0.5, CC and **** p < 0.0001 for cerebellum, Welch´s test). m) CC1 positive cells/mm² (ns difference, Welch´s test for CC and * p < 0.5, Mann Whitney test for cerebellum). n=3 WT and 3 taiep rats.*

To verify our findings with an alternative method, we performed live tissue staining using SiRtubulin and we confirmed that the difference detected by SHG between WT and *taiep* WM is due to tubulin-positive cells. These cells have a morphology that closely resembles the structures that emit SHG in *taiep* white matter (Fig 4.4 a, b, e, f).
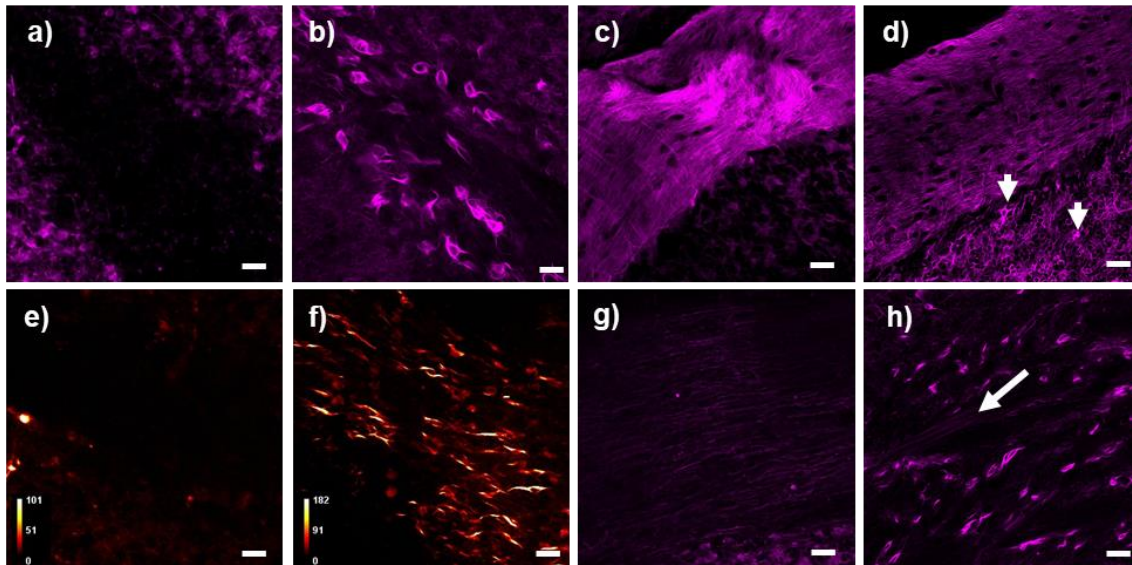

Figure 4.4 Differences between taiep and WT white matter come from microtubules. a, b) Acute tissue sections labeled with SiR-Tubulin. In cerebellar White matter of WT rats no cell bodies were observed (a, 2 WT rats aged 2 months). In contrast, cell bodies with processes labeled for tubulin were detected in taiep rats WM (b, 2 taiep rats aged 8 months). e, f) SHG images from White matter of WT and taiep rats respectively (2 WT and 2 taiep rats aged 6 months). c, d) Microtubules in the molecular and granular layers of WT and taiep rats, respectively. Some cells displaying high intensity were found in the granular layer in taiep rats. g) Microtubules from axons in the white matter of WT rats were observed when laser power was increased. h) Some axons were also observed in taiep white matter using less than half the laser power used for excitation of axons in WT rats. Scale bar in (a, b, e, f) is 20 μm, and in (c, d, g, h) is 30 μm.

Microtubules in the other layers of the cerebellum were organized very similarly. In the molecular layer, long arrangement of microtubules were imaged (Fig 4.4 c, d) in the control and TUBB4A mutant rats. In the granular layer, few cells with high intensity were found (Fig 4.4 d, arrows). The intensity of the fluorescence from cells in *taiep* white matter was high and therefore required low excitation intensity. This intensity was not enough to reveal the fluorescence from microtubular axons in WT rats (Fig 4.4 a); some axons were imaged only after increasing the intensity (Fig 4.4 g). A bundle of axons was also detected with low laser power in the cerebellar white matter of *taiep* rats (Fig 4.4 h, arrow).

Discussion

In this work, we conjugated magnetic resonance imaging, second harmonic generation microscopy and immunohistochemistry in the analysis of the CNS of the taiep rat, which is the animal model for the H-ABC human leukodystrophy.

The noninvasive MRI study gave us information about white matter abnormalities with a resolution of 100 x 100 µm^2, then we used confocal fluorescence microscopy to corroborate these findings by imaging cellular structures at the microscopic level. The main findings of our longitudinal MRI study suggest demyelination in various structures and atrophy of the corpus callosum and the cerebellum of the *taiep* rat. Microscopic observation of white matter uncovers the demyelination in the *taiep* rat. Optical density in corpus callosum and cerebellar white matter of control rats is higher, pointing to the loss of myelin in *taiep* rats. We fluorescently labeled the CNS tissue for myelin and neurofilaments. We observed that fluorescent membrane staining of myelin was more intense and organized in control rats than in the mutants, and consistently the signal from neurofilaments was less intense in control rats. This is well depicted in the corpus callosum and the cerebellar folia where fluorescence intensity from neurofilaments in WM fibers of *taiep* rats was higher than that from the same regions in WT. Our hypothesis is that in WT animals tightly packed myelin sheets might interfere with either the excitation/emission of the labeled axonal cytoskeleton or with the proper diffusion of antibodies underneath the insulator; therefore, only a fraction of the total fluorescence could be detected. It is possible that proper myelination could also interfere with excitation and/or SHG emission from the amount of microtubules present inside axons and covered by several layers of a birefringent material[52]. Experiments and simulations that replicate the geometry of microtubules inside myelinated axons are needed to thoroughly prove this hypothesis.

H-ABC patients suffer from motor problems similarly to the *taiep* rat. One of those is the cerebellar ataxia, which is common to various leukodystrophies. It is still unknown how tubulin mutations induce the atrophy of the cerebellum; however, the ataxic signs of H-ABC due to myelin loss in this organ could be explained with the damage on afferent and efferent pathways of the cerebellum. Motor dysfunction reflects damage in a nervous network that

involves also basal ganglia and cortical areas[59,154,155]. We also found clear evidence, in MRI and by fluorescence microscopy, of striatal damage in the *taiep* rat, which could explain the other motor signs in *taiep* rats that are not explained by cerebellar dysfunction.

In other experiments, we labeled the CNS with an alpha-beta tubulin marker. This tissue showed the presence of cell bodies that were heavily stained for tubulin in the white matter of *taiep* rats, while in the wild type rat, the same staining procedure did not reveal cell bodies. This stronger tubulin fluorescence in cell bodies could be explained by a high amount of tubulin, which agrees with our hypothesis that the cell bodies could be those of defective oligodendrocytes of TUBB4A mutant rats. Oligodendrocytes bodies highly immunoreactive for tubulin have already been reported in *taiep* rats in the CC and cerebellar WM[156], in the anterior medullary velum of the cerebellum[157] and in oligodendrocytes in culture[158]. In previous studies of the mutant rat, electron microscopy has revealed that the body and the processes of the oligodendrocytes have an increased amount of MTs [46,49,78].

Finally, we used a marker suitable for live tissue staining of microtubules looking for the source of the differential signal between *taiep* and control rats. We found that the white matter of *taiep* rats contained cells that were densely marked for tubulin. The shape and distribution of these cells is very similar to what is seen by SHG microscopy, of course the polarization of our laser allows us to obtain signal only from bundles of microtubules oriented horizontally, differently to what occurs in the fluorescence images of microtubules where the whole cytoskeletal structure is highlighted. Tubulin in the molecular layer of the cerebellum was distributed similarly in the animal model of H-ABC and in the healthy rats. In the granular layer some scattered cells loaded with microtubules were observed only in *taiep* rats. This is congruent with what we already described about the fluorescent labeled neurofilaments, in that the granular layer of the cerebellum displays mayor changes in the demyelinated samples compared to the molecular layer.

Conclusions

The development of new techniques like magnetic resonance imaging and exome sequencing contributed to the better understanding of leukodystrophies and completely changed their diagnosis approach. The discoveries made, also changed the way we understand this myelinating disorders and now we know that some of them could be originated in mutations of structural proteins. Tubulinopathies are a subset of leukodistrophies related to mutations in genes for tubulins. The motivation of this work was to contribute in the understanding of the pathophysiology of one of this recently described diseases named hypomyelination with atrophy of the basal ganglia and the cerebellum, which is caused by mutations in tubulin beta 4a.

We provide a longitudinal analysis of the changes in the central nervous system in the *taiep* rat. This animal model naturally shares genetic and clinical characteristics with the human disease. We longitudinally analyzed MRI´s from *taiep* rats from two perspectives; qualitatively, providing anatomic description and recognizing the same radiological pattern described for H-ABC, and quantitatively by analyzing the changes in the volume of the cerebellum and other central structures and correlating them with immunohistochemical changes. We described in detail the white matter abnormalities seen in MRIs in the brain and cerebellum of *taiep* rats from 1 to 10 months. This work collaborated to present the *taiep* rat as the animal model for H-ABC in a context where the unavailability of pathological materials still makes difficult the comprehension of the disease. The accessibility of a trustworthy animal model is fundamental for the understanding of the pathophysiology of the disease itself, also making possible to answer questions that could not be addressed in human patients due to ethical reasons.

We also provide a new alternative for imaging the central nervous system of the animal model for tubulinopathies. The core of this work is the novel use of second harmonic generation microscopy, performed in a commercial microscope, to distinguish between healthy and pathological white matter in the animal model for H-ABC tubulinopathy, in a label free manner. The technique is able to highlight differences that were not described before, doing it in close-to-living conditions, with most cellular features preserved. Our hypothesis that

densely packed microtubules in the abnormal/defective oligodendrocytes emit detectable SH signal was tested by comparing SHG images from the white matter to the results obtained from tissue sections immunolabeled and analyzed by fluorescence microscopy. So far we have imaged by SHG the corpus callosum and the cerebellum of *taiep* rats of different ages finding the same characteristic oligodendrocytes that emit intense SH signal. We also analyzed by fluorescence microscopy the cell density in these regions finding that some mature oligodendrocytes in the white matter *taiep* rats are also strongly stained for tubulin. Finally, fluorescence of tubulins in fresh tissue corroborates that in the TUBB4A mutant rats white matter, some cells have a very intense fluorescence intensity, indicating a higher amount on microtubules. The abnormal cells share morphology and distribution with the cells imaged by SHG microscopy in *taiep* rats. Thus, we confirm that SHG is able to image microtubules from oligodendrocytes in *taiep* rats CNS. Therefore, we propose two uses of SHG microscopy in relation to this myelin disorder: in the long term, it might be integrated in diagnostic approaches, for the screening of biopsies or direct intracranial analysis, but the greatest impact could be associated to try deciphering the molecular basis of H-ABC.

Future perspectives for this research include imaging the CNS of *taiep* rats at birth, also imaging other white matter structures and also performing quantitative studies. New born rats are still unmyelinated, imaging their CNS during the myelinating process may give us information related to the evolution of the microtubule defect. By analyzing CNS of rats of different developmental stages by SHG we may acquire data to correlate SHG signal with the demyelination state. A better understanding of the myelination process, could explain why many patients with hypomyelination experience a slow clinical decline after a long phase of stability[10]. Our SHG study was centered in the analysis of two regions, the corpus callosum and the cerebellum, but we think that other structures should also be analyzed. For instance the striatum should be analyzed as this is one of the structures where we have found more differences related to white matter either by MRI or fluorescence. Another exciting possibility is to obtain quantitative information about the defective microtubules. By polarization SHG we could determine the pitch angle of the dimers of tubulin respect to the microtubule axis in *taiep* and control rats. This type of measurements have been performed in purified microtubules, axonemes and cultured neurons, but not yet in oligodendrocytes. Knowing the angle of tubulin dimers associated to TUBB4A mutation in *taiep* rats is

important as conformational changes in tubulin subunits in the microtubule are the basis for the regulation of polymerization and depolymerization of microtubules.

References

1. Kursula, P. Structural properties of proteins specific to the myelin sheath. *Amino Acids* **34**, 175–185 (2008).

2. Morell, P. & Quarles, R. H. The Myelin Sheath. *Basic Neurochem. Mol. Cell. Med. Asp. 6th Ed.* (1999).

3. Bradl, M. & Lassmann, H. Oligodendrocytes: biology and pathology. *Acta Neuropathol. (Berl.)* **119**, 37–53 (2010).

4. Swire, M. *et al.* Oligodendrocyte HCN2 Channels Regulate Myelin Sheath Length. *J. Neurosci.* **41**, 7954–7964 (2021).

5. Demaerel, P. *et al.* MR findings in leukodystrophy. *Neuroradiology* **33**, 368–371 (1991).

6. van der Knaap, M. S., Valk, J., de Neeling, N. & Nauta, J. J. Pattern recognition in magnetic resonance imaging of white matter disorders in children and young adults. *Neuroradiology* **33**, 478–493 (1991).

7. Knaap, M. S. van der *et al.* New Syndrome Characterized by Hypomyelination with Atrophy of the Basal Ganglia and Cerebellum. *Am. J. Neuroradiol.* **23**, 1466–1474 (2002).

8. Leegwater, P. A. *et al.* Subunits of the translation initiation factor eIF2B are mutant in leukoencephalopathy with vanishing white matter. *Nat. Genet.* **29**, 383–388 (2001).

9. Ng, S. B. *et al.* Targeted capture and massively parallel sequencing of 12 human exomes. *Nature* **461**, 272–276 (2009).

10. Wolf, N. I., ffrench-Constant, C. & van der Knaap, M. S. Hypomyelinating leukodystrophies — unravelling myelin biology. *Nat. Rev. Neurol.* **17**, 88–103 (2021).

11. Ginhoux, F. *et al.* Fate Mapping Analysis Reveals That Adult Microglia Derive from Primitive Macrophages. *Science* **330**, 841–845 (2010).

12. López-Hernández, T. *et al.* Mutant GlialCAM Causes Megalencephalic Leukoencephalopathy with Subcortical Cysts, Benign Familial Macrocephaly, and Macrocephaly with Retardation and Autism. *Am. J. Hum. Genet.* **88**, 422–432 (2011).

13. Wolf, N. I. *et al.* Mutations in RARS cause hypomyelination. *Ann. Neurol.* **76**, 134–139 (2014).

14. Alata, M. *et al.* Longitudinal Evaluation of Cerebellar Signs of H-ABC Tubulinopathy in a Patient and in the taiep Model. *Front. Neurol.* **0**, (2021).

15. Simons, C. *et al.* A de novo mutation in the β-tubulin gene TUBB4A results in the leukoencephalopathy hypomyelination with atrophy of the basal ganglia and cerebellum. *Am. J. Hum. Genet.* **92**, 767–773 (2013).

16. Hamilton, E. M. *et al.* Hypomyelination with atrophy of the basal ganglia and cerebellum: further delineation of the phenotype and genotype-phenotype correlation. *Brain J. Neurol.* **137**, 1921–1930 (2014).

17. Erro, R. *et al.* H-ABC syndrome and DYT4: Variable expressivity or pleiotropy of TUBB4 mutations? *Mov. Disord. Off. J. Mov. Disord. Soc.* **30**, 828–833 (2015).

18. Ferreira, C., Poretti, A., Cohen, J., Hamosh, A. & Naidu, S. Novel TUBB4A mutations and expansion of the neuroimaging phenotype of hypomyelination with atrophy of the basal ganglia and cerebellum (H-ABC). *Am. J. Med. Genet. A.* **164**, 1802–1807 (2014).

19. Miyatake, S. *et al.* Expanding the phenotypic spectrum of TUBB4A-associated hypomyelinating leukoencephalopathies. *Neurology* **82**, 2230–2237 (2014).

20. Curiel, J. *et al.* TUBB4A mutations result in specific neuronal and oligodendrocytic defects that closely match clinically distinct phenotypes. *Hum. Mol. Genet.* **26**, 4506–4518 (2017).

21. Gavazzi, F. *et al.* Acquisition of Developmental Milestones in Hypomyelination With Atrophy of the Basal Ganglia and Cerebellum and Other TUBB4A-Related Leukoencephalopathy. *J. Child Neurol.* 883073821000977 (2021) doi:10.1177/0883073821000977.

22. Lopez-Juarez, A. *et al.* Auditory impairment in H-ABC tubulinopathy. *J. Comp. Neurol.* (2020) doi:10.1002/cne.24990.

23. What is H-ABC. *Foundation to Fight H-ABC* https://www.h-abc.org/habc.

24. Gonçalves, F. G. *et al.* Tubulinopathies. *Top. Magn. Reson. Imaging TMRI* **27**, 395–408 (2018).

25. Binarová, P. & Tuszynski, J. Tubulin: Structure, Functions and Roles in Disease. *Cells* **8**, 1294 (2019).

26. Bahi-Buisson, N. *et al.* The wide spectrum of tubulinopathies: what are the key features for the diagnosis? *Brain J. Neurol.* **137**, 1676–1700 (2014).

27. Sferra, A., Nicita, F. & Bertini, E. Microtubule Dysfunction: A Common Feature of Neurodegenerative Diseases. *Int. J. Mol. Sci.* **21**, 1nn–1nn (2020).

28. Fletcher, D. A. & Mullins, R. D. Cell mechanics and the cytoskeleton. *Nature* **463**, 485–492 (2010).

29. Vemu, A., Atherton, J., Spector, J. O., Moores, C. A. & Roll-Mecak, A. Tubulin isoform composition tunes microtubule dynamics. *Mol. Biol. Cell* **28**, 3564–3572 (2017).

30. Alberts, B. *et al. Molecular Biology of the Cell*. (Garland Science, 2002).

31. Breuss, M. W., Leca, I., Gstrein, T., Hansen, A. H. & Keays, D. A. Tubulins and brain development - The origins of functional specification. *Mol. Cell. Neurosci.* **84**, 58–67 (2017).

32. Weigel, M., Wang, L. & Fu, M.-M. Microtubule organization and dynamics in oligodendrocytes, astrocytes, and microglia. *Dev. Neurobiol.* **81**, 310–320 (2021).

33. Janke, C. The tubulin code: molecular components, readout mechanisms, and functions. *J. Cell Biol.* **206**, 461–472 (2014).

34. Amargant, F., Barragan, M., Vassena, R. & Vernos, I. Insights of the tubulin code in gametes and embryos: from basic research to potential clinical applications in humans. *Biol. Reprod.* **100**, 575–589 (2019).

35. Burgoyne, R. D., Cambray-Deakin, M. A., Lewis, S. A., Sarkar, S. & Cowan, N. J. Differential distribution of beta-tubulin isotypes in cerebellum. *EMBO J.* **7**, 2311–2319 (1988).

36. Strassel, C. *et al.* An essential role for α4A-tubulin in platelet biogenesis. *Life Sci. Alliance* **2**, (2019).

37. Hausrat, T. J., Radwitz, J., Lombino, F. L., Breiden, P. & Kneussel, M. Alpha- and beta-tubulin isotypes are differentially expressed during brain development. *Dev. Neurobiol.* **81**, 333–350 (2021).

38. Mutch, C. A. *et al.* Disorders of Microtubule Function in Neurons: Imaging Correlates. *Am. J. Neuroradiol.* **37**, 528–535 (2016).

39. Hersheson, J. *et al.* Mutations in the autoregulatory domain of β-tubulin 4a cause hereditary dystonia. *Ann. Neurol.* **73**, 546–553 (2013).

40. Romaniello, R. *et al.* Tubulin genes and malformations of cortical development. *Eur. J. Med. Genet.* **61**, 744–754 (2018).

41. Zhang, Y. *et al.* An RNA-Sequencing Transcriptome and Splicing Database of Glia, Neurons, and Vascular Cells of the Cerebral Cortex. *J. Neurosci.* **34**, 11929–11947 (2014).

42. Amos, L. A. & Löwe, J. The subtle allostery of microtubule dynamics. *Nat. Struct. Mol. Biol.* **21**, 505–506 (2014).

43. Robinson, N. B. *et al.* The current state of animal models in research: A review. *Int. J. Surg.* **72**, 9–13 (2019).

44. Twigger, S. N. *et al.* What everybody should know about the Rat Genome and its online resources. *Nat. Genet.* **40**, 523–527 (2008).

45. Holmgren, B., Urbá-Holmgren, R., Riboni, L. & Vega-SaenzdeMiera, E. C. Sprague Dawley rat mutant with tremor, ataxia, tonic immobility episodes, epilepsy and paralysis. *Lab. Anim. Sci.* **39**, 226–228 (1989).

46. Duncan, I. D., Lunn, K. F., Holmgren, B., Urba-Holmgren, R. & Brignolo-Holmes, L. The taiep rat: a myelin mutant with an associated oligodendrocyte microtubular defect. *J. Neurocytol.* **21**, 870–884 (1992).

47. Lunn, K. F., Clayton, M. K. & Duncan, I. D. The temporal progression of the myelination defect in the taiep rat. *J. Neurocytol.* **26**, 267–281 (1997).

48. Garduno-Robles, A. *et al.* MRI Features in a Rat Model of H-ABC Tubulinopathy. *Front. Neurosci.* **14**, 555 (2020).

49. Lunn, K. F., Baas, P. W. & Duncan, I. D. Microtubule organization and stability in the oligodendrocyte. *J. Neurosci. Off. J. Soc. Neurosci.* **17**, 4921–4932 (1997).

50. Duncan, I. D. *et al.* A mutation in the Tubb4a gene leads to microtubule accumulation with hypomyelination and demyelination. *Ann. Neurol.* **81**, 690–702 (2017).

51. Campagnola, P. J. & Loew, L. M. Second-harmonic imaging microscopy for visualizing biomolecular arrays in cells, tissues and organisms. *Nat. Biotechnol.* **21**, 1356–1360 (2003).

52. Kwan, A. C., Dombeck, D. A. & Webb, W. W. Polarized microtubule arrays in apical dendrites and axons. *Proc. Natl. Acad. Sci. U. S. A.* **105**, 11370–11375 (2008).

53. Dombeck, D. A. *et al.* Uniform polarity microtubule assemblies imaged in native brain tissue by second-harmonic generation microscopy. *Proc. Natl. Acad. Sci. U. S. A.* **100**, 7081–7086 (2003).

54. McRobbie, D. W., Moore, E. A., Graves, D. M. J. & Prince, M. R. *MRI from Picture to Proton*. (Cambridge University Press, 2003).

55. Cortés, Ma. D. C., Gavito, B., Ita, M. L., Valencia, J. & Eguibar, J. R. Characterization of the spontaneous and gripping-induced immobility episodes on taiep rats. *Synapse* **58**, 95–101 (2005).

56. Denic, A. *et al.* MRI in Rodent Models of Brain Disorders. *Neurother. J. Am. Soc. Exp. Neurother.* **8**, 3–18 (2011).

57. Yushkevich, P. A. *et al.* User-guided 3D active contour segmentation of anatomical structures: Significantly improved efficiency and reliability. *NeuroImage* **31**, 1116–1128 (2006).

58. Rat Brain Atlas. http://labs.gaidi.ca/rat-brain-atlas/?ml=7&ap=-3&dv=10.

59. Neychev, V. K., Gross, R. E., Lehéricy, S., Hess, E. J. & Jinnah, H. A. The functional neuroanatomy of dystonia. *Neurobiol. Dis.* **42**, 185–201 (2011).

60. Couve, E., Cabello, J. F., Krsulovic, J. & Roncagliolo, M. Binding of microtubules to transitional elements in oligodendrocytes of the myelin mutant taiep rat. *J. Neurosci. Res.* **47**, 573–581 (1997).

61. Silva-Gómez, A. B., Bravo-Duran, D. A., Eguibar, J. R. & Cortes, C. Juvenile Taiep rats have shorter dendritic trees in the dorsal field of the hippocampus without spatial learning disabilities. *Synapse* **72**, e22024 (2018).

62. Fuenzalida, M., Aliaga, E., Olivares, V., Roncagliolo, M. & Bonansco, C. Developmental increase of asynchronic glutamate release from hippocampal synapses in mutant taiep rat. *Synapse* **63**, 502–509 (2009).

63. Volpe, J. J., Kinney, H. C., Jensen, F. E. & Rosenberg, P. A. The developing oligodendrocyte: key cellular target in brain injury in the premature infant. *Int. J. Dev. Neurosci.* **29**, 423–440 (2011).

64. Jose, E. R., del Carmen, C. M., Araceli, U. & Alicia, L.-C. The Myelin Mutant Rat Taiep as a Model of Neuroimmunological Disease. *Adv. Neuroimmune Biol.* **5**, 9–17 (2014).

65. Concha, L., Beaulieu, C., Collins, D. L. & Gross, D. W. White-matter diffusion abnormalities in temporal-lobe epilepsy with and without mesial temporal sclerosis. *J. Neurol. Neurosurg. Psychiatry* **80**, 312–319 (2009).

66. Laule, C. *et al.* Water content and myelin waterfraction in multiple sclerosis. *J. Neurol.* **251**, 284–293 (2004).

67. Campagnola, P. J. *et al.* Three-dimensional high-resolution second-harmonic generation imaging of endogenous structural proteins in biological tissues. *Biophys. J.* **82**, 493–508 (2002).

68. Mohler, W., Millard, A. C. & Campagnola, P. J. Second harmonic generation imaging of endogenous structural proteins. *Methods San Diego Calif* **29**, 97–109 (2003).

69. Denk, W., Strickler, J. H. & Webb, W. W. Two-Photon Laser Scanning Fluorescence Microscopy. *Science* (1990) doi:10.1126/science.2321027.

70. Zipfel, W. R., Williams, R. M. & Webb, W. W. Nonlinear magic: multiphoton microscopy in the biosciences. *Nat. Biotechnol.* **21**, 1369–1377 (2003).

71. Lim, H. Harmonic Generation Microscopy 2.0: New Tricks Empowering Intravital Imaging for Neuroscience. *Front. Mol. Biosci.* **0**, (2019).

72. Jiang, L. *et al.* Label-free imaging of brain and brain tumor specimens with combined two-photon excited fluorescence and second harmonic generation microscopy. *Laser Phys. Lett.* **14**, 105401 (2017).

73. Haines, D. E., Harkey, H. L. & Al-Mefty, O. The "Subdural" SpaceA New Look at an Outdated Concept. *Neurosurgery* **32**, 111–120 (1993).

74. Urabe, N. *et al.* Basement membrane type IV collagen molecules in the choroid plexus, pia mater and capillaries in the mouse brain. *Arch. Histol. Cytol.* **65**, 133–143 (2002).

75. Baas, P. W. & Lin, S. Hooks and Comets: The Story of Microtubule Polarity Orientation in the Neuron. *Dev. Neurobiol.* **71**, 403–418 (2011).

76. Van Steenbergen, V. *et al.* Molecular understanding of label-free second harmonic imaging of microtubules. *Nat. Commun.* **10**, 1–14 (2019).

77. Sharoukhov, D., Bucinca-Cupallari, F. & Lim, H. Microtubule Imaging Reveals Cytoskeletal Deficit Predisposing the Retinal Ganglion Cell Axons to Atrophy in DBA/2J. *Invest. Ophthalmol. Vis. Sci.* **59**, 5292–5300 (2018).

78. Song, J., O'connor, L. T., Yu, W., Baas, P. W. & Duncan, I. D. Microtubule alterations in cultured taiep rat oligodendrocytes lead to deficits in myelin membrane formation. *J. Neurocytol.* **28**, 671–684 (1999).

79. Fu, M. *et al.* The Golgi Outpost Protein TPPP Nucleates Microtubules and is Critical for Myelination. *Cell* **179**, 132-146.e14 (2019).

80. Franken, P. A., Hill, A. E., Peters, C. W. & Weinreich, G. Generation of Optical Harmonics. *Phys. Rev. Lett.* **7**, 118–119 (1961).

81. Bloembergen, N., Chang, R. K., Jha, S. S. & Lee, C. H. Optical Second-Harmonic Generation in Reflection from Media with Inversion Symmetry. *Phys. Rev.* **174**, 813–822 (1968).

82. Eisenthal, K. B. Liquid Interfaces Probed by Second-Harmonic and Sum-Frequency Spectroscopy. *Chem. Rev.* **96**, 1343–1360 (1996).

83. Hellwarth, R. & Christensen, P. Nonlinear optical microscopic examination of structure in polycrystalline ZnSe. *Opt. Commun.* **12**, 318–322 (1974).

84. Freund, I., Deutsch, M. & Sprecher, A. Connective tissue polarity. Optical second-harmonic microscopy, crossed-beam summation, and small-angle scattering in rat-tail tendon. *Biophys. J.* **50**, 693–712 (1986).

85. Bouevitch, O., Lewis, A., Pinevsky, I., Wuskell, J. P. & Loew, L. M. Probing membrane potential with nonlinear optics. *Biophys. J.* **65**, 672–679 (1993).

86. Mercatelli, R. *et al.* Three-dimensional mapping of the orientation of collagen corneal lamellae in healthy and keratoconic human corneas using SHG microscopy. *J. Biophotonics* **10**, 75–83 (2017).

87. Da Costa, V. *et al.* Nondestructive Imaging of Live Human Keloid and Facial Tissue Using Multiphoton Microscopy. *Arch. Facial Plast. Surg.* **10**, 38–43 (2008).

88. Chen, G. *et al.* Nonlinear spectral imaging of human hypertrophic scar based on two-photon excited fluorescence and second-harmonic generation. *Br. J. Dermatol.* **161**, 48–55 (2009).

89. Zhuo, S. *et al.* Label-Free Imaging of Basement Membranes Differentiates Normal, Precancerous, and Cancerous Colonic Tissues by Second-Harmonic Generation Microscopy. *PLOS ONE* **7**, e38655 (2012).

90. Adur, J. *et al.* Second harmonic generation microscopy as a powerful diagnostic imaging modality for human ovarian cancer. *J. Biophotonics* **7**, 37–48 (2014).

91. Burke, K. *et al.* Using second harmonic generation to predict patient outcome in solid tumors. *BMC Cancer* **15**, 929 (2015).

92. Yuting, L. *et al.* Microscale characterization of prostate biopsies tissues using optical coherence elastography and second harmonic generation imaging. *Lab. Invest.* **98**, 380–390 (2018).

93. Hristu, R. *et al.* Quantitative second harmonic generation microscopy for the structural characterization of capsular collagen in thyroid neoplasms. *Biomed. Opt. Express* **9**, 3923–3936 (2018).

94. Varga, B. *et al.* Internal structure and remodeling in dystrophin-deficient cardiomyocytes using second harmonic generation. *Nanomedicine Nanotechnol. Biol. Med.* **30**, 102295 (2020).

95. Feeney, E. J. *et al.* The value of muscle biopsies in Pompe disease: identifying lipofuscin inclusions in juvenile- and adult-onset patients. *Acta Neuropathol. Commun.* **2**, 2 (2014).

96. Bocklitz, T. *et al.* Non-linear multimodal imaging for disease diagnostics and treatment monitoring. in (eds. Sampson, D. D., Matthews, D. L., Popp, J., Rubinsztein-Dunlop, H. & Wilson, B. C.) 103400F (2017). doi:10.1117/12.2275361.

97. Rivenson, Y. *et al.* Virtual histological staining of unlabelled tissue-autofluorescence images via deep learning. *Nat. Biomed. Eng.* **3**, 466–477 (2019).

98. Mazumder, N. *et al.* Label-Free Non-linear Multimodal Optical Microscopy—Basics, Development, and Applications. *Front. Phys.* **7**, 170 (2019).

99. Boyd, R. W. Chapter 2 - Wave-Equation Description of Nonlinear Optical Interactions. in *Nonlinear Optics (Third Edition)* (ed. Boyd, R. W.) 69–133 (Academic Press, 2008). doi:10.1016/B978-0-12-369470-6.00002-2.

100. Pavone, F. S., Campagnola, P. J. & Campagnola, P. J. *Second Harmonic Generation Imaging*. (CRC Press, 2016). doi:10.1201/b15039.

101. Odin, C., Heichette, C., Chretien, D. & Grand, Y. L. Second harmonic microscopy of axonemes. *Opt. Express* **17**, 9235–9240 (2009).

102. Psilodimitrakopoulos, S. *et al.* Estimation of the effective orientation of the SHG source in primary cortical neurons. *Opt. Express* **17**, 14418–14425 (2009).

103. Psilodimitrakopoulos, S. *et al.* Quantitative imaging of microtubule alteration as an early marker of axonal degeneration after ischemia in neurons. *Biophys. J.* **104**, 968–975 (2013).

104. Kaneshiro, J. *et al.* Second harmonic generation polarization microscopy as a tool for protein structure analysis. *Biophys. Physicobiology* **16**, 147–157 (2019).

105. Sanderson, M. J., Smith, I., Parker, I. & Bootman, M. D. Fluorescence Microscopy. *Cold Spring Harb. Protoc.* **2014**, pdb.top071795 (2014).

106. Moreaux, L., Sandre, O., Charpak, S., Blanchard-Desce, M. & Mertz, J. Coherent Scattering in Multi-Harmonic Light Microscopy. *Biophys. J.* **80**, 1568–1574 (2001).

107. LaComb, R., Nadiarnykh, O., Townsend, S. S. & Campagnola, P. J. Phase Matching considerations in Second Harmonic Generation from tissues: Effects on emission directionality, conversion efficiency and observed morphology. *Opt. Commun.* **281**, 1823–1832 (2008).

108. Pelletier, M. J. & Pelletier, C. C. RAMAN SPECTROSCOPY | Instrumentation. in *Encyclopedia of Analytical Science (Second Edition)* (eds. Worsfold, P., Townshend, A. & Poole, C.) 94–104 (Elsevier, 2005). doi:10.1016/B0-12-369397-7/00529-X.

109. Schindelin, J. *et al.* Fiji: an open-source platform for biological-image analysis. *Nat. Methods* **9**, 676–682 (2012).

110. Chameleon Ultra - Tunable Ti:Sapphire Oscillators | Coherent. https://www.coherent.com/lasers/oscillators/chameleon-ultra.

111. Chen, C., Wu, B., You, G., Jiang, A. & Huang, Y. High-Efficiency and Wide-Band Single-Harmonic-Generation Properties of the New Crystal β-BaB2O4. in *International Quantum Electronics Conference (1984), paper MCC5* MCC5 (Optical Society of America, 1984).

112. Govindaraju, I. *et al.* Microscopic and spectroscopic characterization of rice and corn starch. *Microsc. Res. Tech.* **83**, 490–498 (2020).

113. Naguleswaran, S., Vasanthan, T., Hoover, R. & Bressler, D. Amylolysis of amylopectin and amylose isolated from wheat, triticale, corn and barley starches. *Food Hydrocoll.* **35**, 686–693 (2014).

114. Zhuo, G.-Y. *et al.* Three-dimensional structural imaging of starch granules by second-harmonic generation circular dichroism. *J. Microsc.* **253**, 183–190 (2014).

115. Zhuo, Z.-Y. *et al.* Second harmonic generation imaging – A new method for unraveling molecular information of starch. *J. Struct. Biol.* **171**, 88–94 (2010).

116. Psilodimitrakopoulos, S., Amat-Roldan, I., Loza-Alvarez, P. & Artigas, D. Estimating the helical pitch angle of amylopectin in starch using polarization second harmonic generation microscopy. *J. Opt.* **12**, 084007 (2010).

117. Chen, M.-Y. *et al.* Multiphoton imaging to identify grana, stroma thylakoid, and starch inside an intact leaf. *BMC Plant Biol.* **14**, 175 (2014).

118. Mazumder, N., Xiang, L. Y., Qiu, J. & Kao, F.-J. Investigating starch gelatinization through Stokes vector resolved second harmonic generation microscopy. *Sci. Rep.* **7**, 1–9 (2017).

119. Lodish, H. *et al.* Microtubule Dynamics and Motor Proteins during Mitosis. *Mol. Cell Biol. 4th Ed.* (2000).

120. Lullo, G. A. D., Sweeney, S. M., Körkkö, J., Ala-Kokko, L. & Antonio, J. D. S. Mapping the Ligand-binding Sites and Disease-associated Mutations on the Most Abundant Protein in the Human, Type I Collagen *. *J. Biol. Chem.* **277**, 4223–4231 (2002).

121. Hubert, T., Grimal, S., Carroll, P. & Fichard-Carroll, A. Collagens in the developing and diseased nervous system. *Cell. Mol. Life Sci. CMLS* **66**, 1223–1238 (2009).

122. Fuentes-Corona, C. G. *et al.* Second harmonic generation signal from type I collagen fibers grown in vitro. *Biomed. Opt. Express* **10**, 6449–6461 (2019).

123. Yasui, T., Tohno, Y. & Araki, T. Determination of collagen fiber orientation in human tissue by use of polarization measurement of molecular second-harmonic-generation light. *Appl. Opt.* **43**, 2861–2867 (2004).

124. Chou, C.-K. *et al.* Polarization ellipticity compensation in polarization second-harmonic generation microscopy without specimen rotation. *J. Biomed. Opt.* **13**, 014005 (2008).

125. Sharoukhov, D. & Lim, H. On probing conformation of microtubules by second-harmonic generation. *J. Mod. Opt.* **63**, 71–75 (2016).

126. Mansfield, P. J. & Neumann, D. A. Chapter 3 - Structure and Function of Skeletal Muscle. in *Essentials of Kinesiology for the Physical Therapist Assistant (Third Edition)* (eds. Mansfield, P. J. & Neumann, D. A.) 34–49 (Mosby, 2019). doi:10.1016/B978-0-323-54498-6.00003-5.

127. AL-Khayat, H. A. Three-dimensional structure of the human myosin thick filament: clinical implications. *Glob. Cardiol. Sci. Pract.* **2013**, 280–302 (2013).

128. Cooper, G. M. Actin, Myosin, and Cell Movement. *Cell Mol. Approach 2nd Ed.* (2000).

129. Plotnikov, S. V., Millard, A. C., Campagnola, P. J. & Mohler, W. A. Characterization of the Myosin-Based Source for Second-Harmonic Generation from Muscle Sarcomeres. *Biophys. J.* **90**, 693–703 (2006).

130. Awasthi, S. *et al.* Multimodal SHG-2PF Imaging of Microdomain Ca2+-Contraction Coupling in Live Cardiac Myocytes. *Circ. Res.* **118**, e19–e28 (2016).

131. Conde, C. & Cáceres, A. Microtubule assembly, organization and dynamics in axons and dendrites. *Nat. Rev. Neurosci.* **10**, 319–332 (2009).

132. Masters, B. R. *et al.* Mitigating thermal mechanical damage potential during two-photon dermal imaging. *J. Biomed. Opt.* **9**, 1265–1270 (2004).

133. Barney, C. W. *et al.* Cavitation in soft matter. *Proc. Natl. Acad. Sci.* **117**, 9157–9165 (2020).

134. Tischfield, M. A. & Engle, E. C. Distinct α and β–tubulin isotypes are required for the positioning, differentiation, and survival of neurons: new support for the "multi-tubulin" hypothesis. *Biosci. Rep.* **30**, 319–330 (2010).

135. Lim, H. *et al.* Label-free imaging of Schwann cell myelination by third harmonic generation microscopy. *Proc. Natl. Acad. Sci.* **111**, 18025–18030 (2014).

136. Redlich, M., Redlich, M., Lim, H. & Lim, H. Label-Free Intravital Imaging of Cortical Myelin in Mouse Brain by Third-Harmonic Generation Microscopy. in *Biophotonics Congress: Optics in the Life Sciences Congress 2019 (BODA,BRAIN,NTM,OMA,OMP) (2019), paper JT4A.9* JT4A.9 (Optical Society of America, 2019). doi:10.1364/BODA.2019.JT4A.9.

137. Wang, H., Fu, Y., Zickmund, P., Shi, R. & Cheng, J.-X. Coherent anti-stokes Raman scattering imaging of axonal myelin in live spinal tissues. *Biophys. J.* **89**, 581–591 (2005).

138. Fu, Y. *et al.* Paranodal myelin retraction in relapsing experimental autoimmune encephalomyelitis visualized by coherent anti-Stokes Raman scattering microscopy. *J. Biomed. Opt.* **16**, 106006 (2011).

139. Bélanger, E. *et al.* In vivo evaluation of demyelination and remyelination in a nerve crush injury model. *Biomed. Opt. Express* **2**, 2698–2708 (2011).

140. Hajjar, H. *et al.* Label-free non-linear microscopy to measure myelin outcome in a rodent model of Charcot-Marie-Tooth diseases. *J. Biophotonics* **11**, e201800186 (2018).

141. Witte, S. *et al.* Label-free live brain imaging and targeted patching with third-harmonic generation microscopy. *Proc. Natl. Acad. Sci.* **108**, 5970–5975 (2011).

142. Hill, R. A. & Grutzendler, J. Uncovering the biology of myelin with optical imaging of the live brain. *Glia* **67**, 2008–2019 (2019).

143. Stoothoff, W. H., Bacskai, B. J. & Hyman, B. T. Monitoring Tau-Tubulin Interactions Utilizing Second Harmonic Generation in Living Neurons. *J. Biomed. Opt.* **13**, 064039 (2008).

144. Kwan, A. C., Duff, K., Gouras, G. K. & Webb, W. W. Optical visualization of Alzheimer's pathology via multiphoton-excited intrinsic fluorescence and second harmonic generation. *Opt. Express* **17**, 3679–3689 (2009).

145. Bancelin, S. *et al.* Probing microtubules polarity in mitotic spindles in situ using Interferometric Second Harmonic Generation Microscopy. *Sci. Rep.* **7**, 1–8 (2017).

146. Lautrup, S., Sinclair, D. A., Mattson, M. P. & Fang, E. F. NAD+ in Brain Aging and Neurodegenerative Disorders. *Cell Metab.* **30**, 630–655 (2019).

147. Pawley. *Handbook of Biological Confocal Microscopy*. (Springer Science & Business Media, 2010).

148. Wiley: Current Protocols Select: Methods and Applications in Microscopy and Imaging - Simon Watkins, Claudette St. Croix. http://www.wiley.com/WileyCDA/WileyTitle/productCd-1118044312.html.

149. Fluorescein, Oregon Green and Rhodamine Green Dyes—Section 1.5 - CL. //www.thermofisher.com/cl/es/home/references/molecular-probes-the-handbook/fluorophores-and-their-amine-reactive-derivatives/fluorescein-oregon-green-and-rhodamine-green-dyes.html.

150. Panchuk-Voloshina, N. *et al.* Alexa dyes, a series of new fluorescent dyes that yield exceptionally bright, photostable conjugates. *J. Histochem. Cytochem. Off. J. Histochem. Soc.* **47**, 1179–1188 (1999).

151. Coons, A. H., Creech, H. J. & Jones, R. N. Immunological Properties of an Antibody Containing a Fluorescent Group. *Proc. Soc. Exp. Biol. Med.* **47**, 200–202 (1941).

152. Lukinavičius, G. *et al.* Fluorogenic probes for live-cell imaging of the cytoskeleton. *Nat. Methods* **11**, 731–733 (2014).

153. Schmidt, U., Weigert, M., Broaddus, C. & Myers, G. Cell Detection with Star-convex Polygons. (2018) doi:10.1007/978-3-030-00934-2_30.

154. Prudente, C. N., Hess, E. J. & Jinnah, H. A. Dystonia as a Network Disorder: What is the Role of the Cerebellum? *Neuroscience* **260**, 23–35 (2014).

155. Shakkottai, V. G. *et al.* Current Opinions and Areas of Consensus on the Role of the Cerebellum in Dystonia. *Cerebellum Lond. Engl.* **16**, 577–594 (2017).

156. Krsulovic, J., Couve, E. & Roncagliolo, M. Dysmyelination, demyelination and reactive astrogliosis in the optic nerve of the taiep rat. *Biol. Res.* **32**, 253–262 (1999).

157. Song, J., Goetz, B. D., Kirvell, S. L., Butt, A. M. & Duncan, I. D. Selective myelin defects in the anterior medullary velum of the taiep mutant rat. *Glia* **33**, 1–11 (2001).

158. Song, J., Carson, J. H., Barbarese, E., Li, F.-Y. & Duncan, I. D. RNA transport in oligodendrocytes from the taiep mutant rat. *Mol. Cell. Neurosci.* **24**, 926–938 (2003).

List of publications

Alata, M., González-Vega, A., Piazza, V., Kleinert-Altamirano, A., Cortes, C., Ahumada-Juárez, J.C., Eguibar, J.R., López-Juárez, A., Hernandez, V.H., 2021. Longitudinal Evaluation of Cerebellar Signs of H-ABC Tubulinopathy in a Patient and in the *taiep* Model. Front. Neurol. 12, 1113. https://doi.org/10.3389/fneur.2021.702039

Lopez-Juarez, A., Gonzalez-Vega, A., Kleinert-Altamirano, A., Piazza, V., Garduno-Robles, A., **Alata, M**., Villaseñor-Mora, C., Eguibar, J.R., Cortes, C., Padierna, L.C., Hernandez, V.H., 2021. Auditory impairment in H-ABC tubulinopathy. J Comp Neurol 529, 957–968. https://doi.org/10.1002/cne.24990

Garduno-Robles, A., **Alata, M**., Piazza, V., Cortes, C., Eguibar, J.R., Pantano, S., Hernandez, V.H., 2020. MRI Features in a Rat Model of H-ABC Tubulinopathy. Front Neurosci 14, 555. https://doi.org/10.3389/fnins.2020.00555

Alata, M., Cervantes, J.C.M., Roldán, A.S.J., Rodriguez, M., Vega, A.G., Piazza, V., 2019. 3,3'-thiodipropanol as a versatile refractive index-matching mounting medium for fluorescence microscopy. Biomed Opt Express 10, 1136–1150. https://doi.org/10.1364/BOE.10.001136

Alata M, Martínez Cervantes J.C, Rodriguez M., Armas-Perez J.C. and Piazza V., 2017. "Optimización de un medio de montaje para microscopia de alta resolución," Avance de la Ciencia en México, 4875-4883.

Alata M., Piazza V., Eguibar J.R., Cortes C., Hernandez V.H., H-ABC tubulinopathy revealed by label-free nonlinear optics, Submitted (October 2021).

CONFERENCE PRESENTATIONS

• Poster presentation in XVI Encuentro Participación de la Mujer en la Ciencia, León, México, 2017.

• Poster presentation in XX Reunión de Neuroimagen, Guanajuato, México, 2018.

• Poster presentation in XXI Reunión de Neuroimagen, Guanajuato, México, 2019.

• Oral presentation in Photonics West 2020 BIOS, San Francisco, California, 2020.

• Alata M., Cervantes, J.C.M., Piazza, V., 2020. 3,3'-thiodipropanol as a refractive index matching mounting medium for fluorescence microscopy, in: Three-Dimensional and Multidimensional Microscopy: Image Acquisition and Processing XXVII. Presented at the Three-Dimensional and Multidimensional Microscopy: Image Acquisition and Processing XXVII, International Society for Optics and Photonics, p. 1124514. https://doi.org/10.1117/12.2551802

Awards

3rd Place, Poster competition for Graduate students, second edition, 2021

1st Place, Poster competition for Graduate students, first edition, 2019

Centro de Investigaciones en Optica A.C.